

VILNIUS UNIVERSITY  
CENTER FOR PHYSICAL SCIENCES AND TECHNOLOGY

Rūta Raišelienė

**Investigation of Phase Transformations  
in the Synthesis of Magnesium  
Whitlockite Powders and Granules by  
the Dissolution-Precipitation Method**

**DOCTORAL DISSERTATION**

Natural Sciences,  
Chemistry (N 003)

VILNIUS 2025

The dissertation was prepared between 2019 and 2025 while studying at Vilnius University.

**Academic Supervisor – Assoc. Prof. Dr. Inga Grigoravičiūtė** (Vilnius University, Natural Sciences, Chemistry – N 003).

This doctoral dissertation will be defended in a public meeting of the Dissertation Defence Panel:

**Chairman – Assoc. Prof. Dr. Justina Gaidukevič** (Vilnius University, Natural Sciences, Chemistry – N 003).

**Members:**

**Dr. Germanas Peleckis** (University of Wollongong, Australian Institute for Innovative Materials, Natural sciences, Chemistry – N 003),

**Prof. Habil. Dr. Rimantas Ramanauskas** (Center for Physical Sciences and Technology, Natural sciences, Chemistry – N 003),

**Assoc. Prof. Dr. Živilė Stankevičiūtė** (Vilnius University, Natural Sciences, Chemistry – N 003),

**Prof. Dr. Vida Vičkačkaitė** (Vilnius University, Natural Sciences, Chemistry – N 003).

The dissertation shall be defended at a public meeting of the Dissertation Defence Panel at 2 pm on the 26th of September 2025 in the Inorganic Chemistry auditorium (141) of the Institute of Chemistry, Faculty of Chemistry and Geoscience, Vilnius University.

Address: Naugarduko str. 24, LT-03225 Vilnius, Lithuania

Tel. +370 5 2193105; e-mail: [info@chgf.vu.lt](mailto:info@chgf.vu.lt)

The text of this dissertation can be accessed at the library of Vilnius University as well as on the website of Vilnius University:

[www.vu.lt/lt/naujienos/ivykuu-kalendorius](http://www.vu.lt/lt/naujienos/ivykuu-kalendorius)

VILNIAUS UNIVERSITETAS  
FIZINIŲ IR TECHNOLOGIJOS MOKSLŲ CENTRAS

Rūta Raišelienė

Fazinių virsmų tyrimas  
tirpinimo-nusodinimo metodu  
sintetinant magnio vitlokito miltelius ir  
granules

**DAKTARO DISERTACIJA**

Gamtos mokslai,  
Chemija (N 003)

VILNIUS 2025

Disertacija rengta 2019–2025 metais Vilniaus universitete.

**Mokslinė vadovė – doc. dr. Inga Grigoravičiūtė** (Vilniaus universitetas, gamtos mokslai, chemija – N 003).

Gynimo taryba:

**Pirmininkė – doc. dr. Justina Gaidukevič** (Vilniaus universitetas, gamtos mokslai, chemija – N 003).

**Nariai:**

**dr. Germanas Peleckis** (Vollongongo universitetas, Australijos inovatyviųjų medžiagų institutas, gamtos mokslai, chemija – N 003),

**prof. habil. dr. Rimantas Ramanauskas** (Fizinių ir technologijos mokslų centras, gamtos mokslai, chemija – N 003),

**doc. dr. Živilė Stankevičiūtė** (Vilniaus universitetas, gamtos mokslai, chemija – N 003)

**prof. dr. Vida Vičkačkaitė** (Vilniaus universitetas, gamtos mokslai, chemija – N 003)

Disertacija ginama viešame Gynimo tarybos posėdyje 2025 m. rugsėjo mėn. 26 d. 14 val. Vilniaus universiteto Chemijos instituto Chemijos ir Geomokslų fakulteto Neorganinės chemijos auditorijoje, 141. Adresas: Naugarduko g. 24, LT-03225, Vilnius, Lietuva, tel. +370 5 2193105; el. paštas [info@chgf.vu.lt](mailto:info@chgf.vu.lt).

Disertaciją galima peržiūrėti Vilniaus universiteto bibliotekoje ir VU interneto svetainėje adresu: [www.vu.lt/lt/naujienos/ivykiu-kalendorius](http://www.vu.lt/lt/naujienos/ivykiu-kalendorius)

## TABLE OF CONTENTS

LIST OF ABBREVIATIONS .....	7
INTRODUCTION.....	8
1. LITERATURE OVERVIEW .....	12
1.1. Bones.....	12
1.2. The demand for hard tissue substitutes .....	15
1.3. Biomaterials .....	16
1.3.1. CaP-based biomaterials .....	17
1.3.2. Variety of CaP-based bioceramics forms .....	19
1.3.3. Variety of CaP-based bioceramics .....	22
1.3.3.1. Magnesium whitlockite .....	24
1.4. Synthesis of Calcium Phosphates.....	26
1.4.1. Dissolution-precipitation synthesis .....	27
1.4.2. Synthesis Methods and potential application fields of Mg-WH .....	29
2. EXPERIMENTAL PART .....	39
2.1. Reagents .....	39
2.2. Synthesis methodology .....	39
2.2.1. Large-scale synthesis of Mg-WH powders: influence of reaction time.....	39
2.2.2. Large-scale synthesis of Mg-WH granules: the effect of reaction pH on phase composition .....	40
2.2.3. Synthesis of Mg-WH granules with different morphology through variations in precursor compositions .....	41
2.4. Characterization .....	43
3. RESULTS AND DISCUSSION .....	46
3.1. Large-scale synthesis and characterization of Mg-WH powders: influence of reaction time.....	46
3.2. Large-Scale synthesis and characterization of Mg-WH granules: the effect of reaction pH on phase composition.....	54

3.3. Synthesis of Mg-WH granules with different morphology through variations in precursor compositions .....	64
<b>4. CONCLUSIONS.....</b>	<b>73</b>
SUMMARY IN LITHUANIAN .....	75
SANTRUMPŪ SARAŠAS .....	75
ĮVADAS.....	76
DISERTACIJOS SANDARA .....	80
<b>1. LITERATŪROS APŽVALGA .....</b>	<b>80</b>
<b>2. EKSPERIMENTO METODIKA .....</b>	<b>80</b>
<b>3. REZULTATAI IR JŪ APTARIMAS .....</b>	<b>81</b>
3.1. Didelio kieko Mg-WH miltelių sintezė ir apibūdinimas .....	81
3.2. Didelio kieko Mg-WH granulių sintezė ir apibūdinimas .....	87
3.3. Skirtingos morfologinės sudėties magnio vitlokito granulių sintezė iš skirtingos sudėties pradinių granulių.....	96
<b>4. IŠVADOS .....</b>	<b>104</b>
REFERENCES.....	105
ACKNOWLEDGMENTS.....	131
LIST OF PUBLICATIONS AND ATTENDING CONFERENCES ...	132
CURRICULUM VITAE .....	134

## LIST OF ABBREVIATIONS

$\alpha$ -TCP	$\alpha$ -tricalcium phosphate ( $\alpha$ -Ca <sub>3</sub> (PO <sub>4</sub> ) <sub>2</sub> )
BCP	Biphasic calcium phosphate
$\beta$ -TCP	$\beta$ -tricalcium phosphate ( $\beta$ -Ca <sub>3</sub> (PO <sub>4</sub> ) <sub>2</sub> )
BET	Brunauer–Emmet–Teller
BJH	Barrett–Joyner–Halenda
CaP	Calcium phosphate
CASU	Calcium sulphate (CaSO <sub>4</sub> )
CDHA	Calcium-deficient hydroxyapatite (Ca <sub>9</sub> (HPO <sub>4</sub> )(PO <sub>4</sub> ) <sub>5</sub> OH)
CHA	Carbonated hydroxyapatite (Ca <sub>10-a</sub> (PO <sub>4</sub> ) <sub>6-b</sub> (CO <sub>3</sub> ) <sub>c</sub> (OH) <sub>2-d</sub> )
COLL	Collagen
CPC	Calcium phosphate cement
CS	Chitosan
CSH	Calcium sulphate hemihydrate (CaSO <sub>4</sub> ·0.5H <sub>2</sub> O)
DCPA	Calcium hydrogen phosphate anhydrous (CaHPO <sub>4</sub> )
DCPD	Calcium hydrogen phosphate dihydrate (CaHPO <sub>4</sub> ·2H <sub>2</sub> O)
DTG	Differential thermogravimetry
EDX	Energy-dispersive X-ray
FGF-18	Fibroblast growth factor
FT-IR	Fourier transform infrared spectroscopy
GEL	Gelatine
GYP	Calcium sulphate dihydrate (CaSO <sub>4</sub> ·2H <sub>2</sub> O)
HAP	Hydroxyapatite (Ca <sub>10</sub> (PO <sub>4</sub> ) <sub>6</sub> (OH) <sub>2</sub> )
ICDD	International Centre for Diffraction Data
Mg(Ac) <sub>2</sub>	Magnesium acetate tetrahydrate (Mg(CH <sub>3</sub> COO) <sub>2</sub> ·4H <sub>2</sub> O)
Mg-WH	Magnesium whitlockite (Ca <sub>18</sub> Mg <sub>2</sub> (HPO <sub>4</sub> ) <sub>2</sub> (PO <sub>4</sub> ) <sub>12</sub> )
MP	Dimagnesium phosphate (MgHPO <sub>4</sub> ·xH <sub>2</sub> O)
NP	Nanoparticle
OCP	Octacalcium phosphate (Ca <sub>8</sub> (HPO <sub>4</sub> ) <sub>2</sub> (PO <sub>4</sub> ) <sub>4</sub> ·5H <sub>2</sub> O)
PLGA	Poly(lactic-co-glycolic) acid
RIR	Normalized corundum reference intensity ratio
S <sub>BET</sub>	Specific surface area
S <sub>ext</sub>	External surface area
SEM	Scanning electron microscopy
TCP	Tricalcium phosphate (Ca <sub>3</sub> (PO <sub>4</sub> ) <sub>2</sub> )
TG	Thermogravimetric analysis
V <sub>p</sub>	Total pore volume
V <sub><math>\mu</math></sub>	Micropore volume
XRD	X-ray diffraction

## INTRODUCTION

Traumatic injuries have been shown to have a significant impact on human quality of life worldwide and pose major challenges for health care and biomedical research [1–5]. The aging population in some regions and the growing demographic in others have contributed to an increased prevalence of bone disorders, thereby highlighting a rising demand for bone implants [6]. A range of synthetic calcium phosphate (CaP) substitutes has been developed to promote the formation of new bone tissue within bone defects [7–11]. These synthetic substitutes have found extensive applications in the medical and dental fields, playing crucial roles in dental implants, alveolar bone augmentation, orthopedics, and drug delivery systems [12–15]. The notable merits of CaPs, which have garnered considerable attention, include their exceptional biocompatibility, controlled biodegradability, osteoconductive properties, and potential for osseointegration [16,17]. Currently, artificial bone substitutes are prepared in the form of powders, granules, dense or porous scaffolds, and bioactive coatings on metal prostheses[18–20].

The composition of the inorganic portion of bone tissue, particularly the presence of carbonated apatite as the primary inorganic phase, is widely accepted [21]. However, there is a lack of consensus regarding the role, importance, and existence of magnesium whitlockite ( $Mg\text{-WH}$ ,  $\text{Ca}_{18}\text{Mg}_2(\text{HPO}_4)_2(\text{PO}_4)_{12}$ ) in bone tissue, a subject that is the focus of ongoing research [22,23]. Some research suggests that Mg-WH is one of the main inorganic components of bone tissue, highlighting its high abundance, which accounts for approximately 25 to 35 wt% of hard tissues [24]. Conversely, other researchers propose that Mg-WH is primarily associated with calcifications that occur as a result of pathological processes or mineralization under certain conditions, such as those observed in calcific tendinitis or the development of calcified atherosclerotic plaques [23]. The presence of Mg-WH in bone tissue remains a subject of debate, but its synthetic analogue is noteworthy among CaP substitutes due to the presence of magnesium ( $Mg^{2+}$ ) ions in its structure, which are essential for various physiological functions in the human body [25–27]. Moreover,  $Mg^{2+}$  ions released from bone substitute materials under physiological conditions have been reported to promote osteogenic differentiation and accelerate bone formation around implants [28]. Previous studies have highlighted the necessity of developing large-scale synthesis methods for Mg-WH to support its potential applications in bone regeneration and biomaterials research [29,30].

Synthetic CaP-based materials designed for hard tissue regeneration are often utilised in granular form, offering both dental and orthopedic surgeons

increased flexibility in addressing irregular bone defects or voids of varying shapes [31,32]. Despite the promising potential of Mg-WH granules in bone tissue engineering, research on this form remains scarce. The majority of studies have focused on powdered Mg-WH, with possibly only one study specifically exploring the granular form [33]. A recent study by Lee et al. described the synthesis of Mg-WH granules from Mg-WH nanoparticles, which were obtained using the tri-solvent system. The resulting granules exhibited remarkable bone regeneration capabilities in rat calvarial defects, effectively preserving bone thickness without inducing inflammation [33]. Although synthetic Mg-WH has shown promise as a biomaterial, detailed investigation of the properties and functions of Mg-WH has been limited due to the difficulty in synthesising the pure phase, which has greatly hindered extensive research in this area [22,34]. This complexity of Mg-WH synthesis is primarily attributed to the distinctive formation characteristics of the material, which necessitate precision within a narrow pH and temperature range. Moreover, Mg-WH, which is a thermally unstable phase, is difficult to synthesize using conventional high-temperature methods [16,35]. Upon annealing above ca. 600 °C, this material decomposes by releasing water and transforming into a mixture of Mg-substituted  $\beta$ -Ca<sub>3</sub>(PO<sub>4</sub>)<sub>2</sub> and Ca<sub>2</sub>P<sub>2</sub>O<sub>7</sub>. In addition, conventional high-temperature processes often increase the crystallinity of final products, which may reduce their tissue compatibility [36]. In contrast, low-crystallinity porous CaP granules promote bone tissue healing, as porosity is essential for bioactivity and osteoconductivity [37].

To overcome these challenges, dissolution-precipitation reactions have emerged as a method for producing porous ceramics with low crystallinity and larger specific surface area ( $S_{BET}$ ) [37]. A key advantage of dissolution-precipitation reactions is their ability to maintain the shape of the precursor material, closely similar to that of the final product [38]. Moreover, it enables the production of granules, which serve as final products directly deployable for bone augmentation procedures [31,39,40]. This synthesis approach is both simple and economical as it eliminates the need for expensive, specialized equipment, such as hydrothermal reactors or high-temperature furnaces. Additionally, it reduces operational costs by removing the necessity for continuous monitoring of critical parameters like temperature and pH, which are essential for Mg-WH synthesis.

***The aim of this doctoral thesis*** is to investigate the phase transformations that govern the synthesis of Mg-WH powders and granules *via* a dissolution-precipitation method, and to optimize scalable synthesis conditions capable of yielding high-purity Mg-WH powders and granules in substantial quantities.

***The tasks of the research are the following:***

- to investigate the time-dependent formation behavior of the Mg-WH phase using gypsum powders as an environmentally benign precursor, and to conduct a characterization of Mg-WH powder with respect to phase composition and purity, crystallographic parameters, functional groups, thermal stability, surface morphology, elemental composition, and surface properties;
- to determine the optimal pH conditions for the precipitation of Mg-WH granules with gypsum-based granules as the precursor, to evaluate the influence of pH on the resulting phase composition, and to characterize the Mg-WH granules regarding phase purity, crystallographic parameters, functional groups, granule size and morphology, surface and antibacterial properties;
- to develop and modify precursor granules with varying chemical compositions by adjusting the ratios of diammonium hydrogen phosphate, magnesium hydrogen phosphate, and calcium sulfate; to investigate their transformation into biphasic or single-phase Mg-WH granules, and to characterize the resulting granules in terms of phase composition and purity, crystallographic parameters, functional groups, granule morphology, and surface properties.

## NOVELTY OF THE THESIS

This research presents an innovative method for synthesizing Mg-WH through a dissolution-precipitation technique, which offers significant advantages over conventional approaches. Unlike traditional synthesis routes that require costly equipment such as hydrothermal reactors and demand continuous monitoring of critical parameters like pH and temperature, the proposed method simplifies the process without compromising material quality. This study is the first to employ gypsum as a precursor to synthesize Mg-WH granules. It is a naturally abundant, and environmentally friendly material, thereby enhancing the sustainability and accessibility of the synthesis process. As a result, the method is not only more cost-effective but also readily scalable, making it suitable for large-scale production. Importantly, this work also proposes, for the first time, a strategy for the large-scale synthesis of Mg-WH in both powder and granule forms, demonstrating the method's practical applicability for industrial production. Furthermore, by systematically varying the composition of the precursors and adjusting the reaction conditions, this study achieves precise control over the resulting phase composition, particle morphology, and structural characteristics of Mg-WH, which are critical for

its potential applications in fields such as bone regeneration and biomaterials engineering. This outcome is indicative of the versatility of the proposed synthesis method, which can be adapted in order to produce either single-phase or biphasic calcium phosphates (BCPs).

## KEY DEFENSE STATEMENTS

1. This work demonstrates a simple, cost-effective, and environmentally sustainable method for the large-scale synthesis of high-purity Mg-WH powder and granules using gypsum as a precursor, with controlled phase formation and comprehensive structural, morphological, and compositional characterisation confirming the successful development of a scalable synthesis route.
2. The phase transformation of the Mg-WH powder can be demonstrated by systematically varying the reaction time. Mg-WH crystals exhibit well-defined rhombohedral morphology, homogeneous elemental distribution (Ca, Mg, P), and consistent lattice parameters that are aligned with reported values in the literature.
3. The phase composition of product granules may be effectively regulated by the pH of the reaction solution. The synthesis method has been demonstrated to be capable of producing both single-phase Mg-WH, DCPD, and BCPs (Mg-WH with CDHA) granules.
4. This work establishes a controllable synthesis strategy for producing Mg-WH granules with tailored morphologies and phase compositions via a tunable dissolution-precipitation approach. The successful fabrication of both single-phase Mg-WH and biphasic (Mg-WH with CDHA or DCPA) granules was enabled by strategic variation of precursor formulations and reaction times.

# 1. LITERATURE OVERVIEW

## 1.1. Bones

Bones and other calcified tissues are naturally anisotropic compounds, where biominerals (the bones' inorganic phase) are embedded within a protein matrix (organic phase of the bones), together with other organic materials and water, as illustrated in Figure 1 [41]. The bone mineral, comprising 60–70% overall composition of the bones, is a non-stoichiometric carbonated hydroxyapatite (CHA;  $\text{Ca}_{10-a}(\text{PO}_4)_{6-b}(\text{CO}_3)_c(\text{OH})_{2-d}$ ) with low crystallinity and nanometer-sized particles. Its  $\text{Ca}^{2+}$  and  $\text{PO}_4^{3-}$  ions are essential for providing bone hardness, rigidity, and structural strength [42,43]. Bone minerals also possess a considerable amount of anionic (e.g.,  $\text{HPO}_4^{2-}$ ,  $\text{CO}_3^{2-}$ ,  $\text{Cl}^-$ ) and cationic (e.g.,  $\text{Na}^+$ ,  $\text{Mg}^{2+}$ ) constituents, leading in a structurally disordered and compositionally non-stoichiometric nature [43]. CHA in bone exhibits a plate-like crystal morphology, with sizes ranging from 20 to 80 nm in length, 15 to 30 nm in width, and 2 to 10 nm in thickness [44]. The Ca/P ratio in synthetic hydroxyapatite (HAP;  $\text{Ca}_{10}(\text{PO}_4)_{6}(\text{OH})_2$ ) is 1.67, while the Ca/P ratio in bone minerals ranges from 1.37 to 1.87 [45–47].

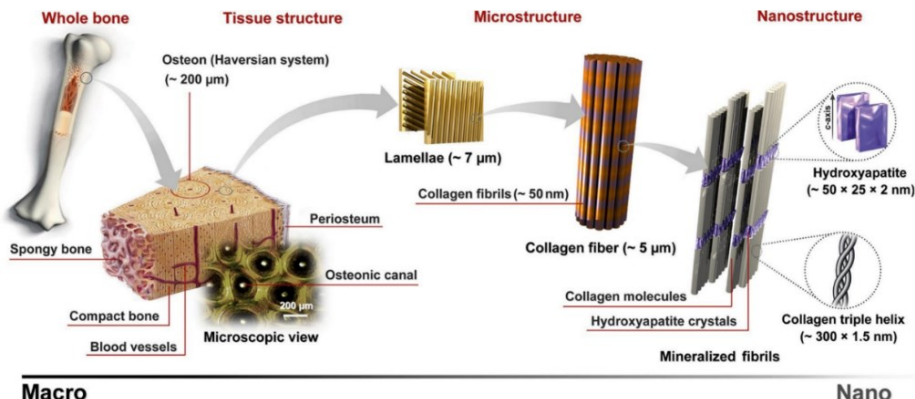


**Figure 1.** The hierarchical structure of typical bone at different length scales (from microstructure to nanostructure) [41].

Collagen (COLL) makes up approximately 85–90% of the protein content in bone, while the remaining 10% consists of noncollagenous proteins, proteoglycans, and phospholipids, forming the organic matrix of bone [48,49]. It provides elasticity and toughness while serving as the primary framework for mineral formation [41,50,51]. Recent studies have revealed that COLL regulates the growth of CHA and influences the size, shape, orientation, and 3D distribution of apatite crystals [44].

A comprehensive understanding of the bone 3D structure of the material is crucial for elucidating how bone forms and functions [52]. Human bone is classified as woven or lamellar [53]. Woven bone, with a randomly organized extracellular matrix, forms during initial growth and fracture healing and contains more osteocytes than lamellar bone [54,55]. Lamellar bone comprises organized COLL fibers and apatite crystals and exists as cortical (compact) or trabecular (spongy) bone [56–58]. Cortical bone, which makes up ~80% of the skeleton, has 5–10% porosity, while trabecular bone is 50–90% porous [53,59,60]. Cortical bone consists of osteons, collections of concentric lamellae that surround a Haversian canal with blood vessels and nerves [53,61]. Recent studies have shown that the structure of osteons, including osteocytes embedded in canaliculi, lamellae, and Haversian canals, regulates cortical bone turnover and regeneration [62,63]. More porous, elastic, and metabolically active trabecular bone, found in long bone ends and flat bones, does not form osteons, but the lamellae are arranged in parallel sheets, creating trabeculae, which intersect bony plates. [53,64,65].

Bones combine hard inorganic and resilient organic components, possessing remarkable mechanical properties comparable to aluminum or mild steel, but with lower weight [66]. Key physicochemical properties of bone include interconnecting porosity, biodegradability, bioactivity, osteoconductivity, and osteoinductivity [67]. The size and interconnectivity of bone porosity significantly influence vascularization, nutrient and cell diffusion, and tissue ingrowth.

The human skeleton undergoes continuous remodeling, where microscopic and molecular processes degrade old bone and replace it with new functional tissue, renewing the entire skeleton approximately every ten years [68,69]. Bone remodeling occurs through the matched performance of bone cells: osteoclasts resorb bone, osteoblasts create bone, and osteocytes participate in the bone remodeling process as mechanosensors and orchestrators [70]. Remodeling allows bones to adapt to mechanical stresses, repair injuries, and maintain mineral homeostasis [66]. Bone ensures mechanical support for joints, tendons, and ligaments, protects organs, and facilitates movement [71,72]. Despite appearing static, bone is remarkably dynamic at a microscopic scale [73]. Imbalances in remodeling can lead to diseases — excessive resorption causes osteoporosis, while excessive formation leads to osteopetrosis [70]. Bone can repair minor damage, such as microcracks approximately 100  $\mu\text{m}$  or slightly longer along the longitudinal axis [74]. However, extensive damage caused by trauma, bone resection due to infection or tumors, nonunions, genetic disorders, or aging exceeds the natural self-healing capacity of bone.

Bone remodeling serves two purposes: repair of microfractures (targeted remodeling) and maintenance of mineral homeostasis by providing access to  $\text{Ca}^{2+}$  and  $\text{PO}_4^{3-}$  reserves (random remodeling) [75]. This occurs within the basic multicellular unit, as Frost defined, consisting of osteoclasts, osteoblasts, and osteocytes within the bone remodeling cavity [73,76]. Osteoblasts, responsible for bone formation, originate from mesenchymal stem cells (MSCs). In contrast, osteoclasts are large, multinucleated cells – up to 100  $\mu\text{m}$  in diameter – that derive from hematopoietic stem cells and are tasked with bone resorption [77]. Osteocytes, the most abundant bone cells, differentiate from osteoblasts and act as primary mechanosensors, regulating remodeling [78].

The bone remodeling cycle typically spans 7 to 9 months but can extend up to 5 years, though newly formed bone gains a substantial load-bearing capacity much earlier [79]. This tightly regulated process consists of activation, resorption, reversal, formation, and termination as illustrated in Figure 2 [80–82].

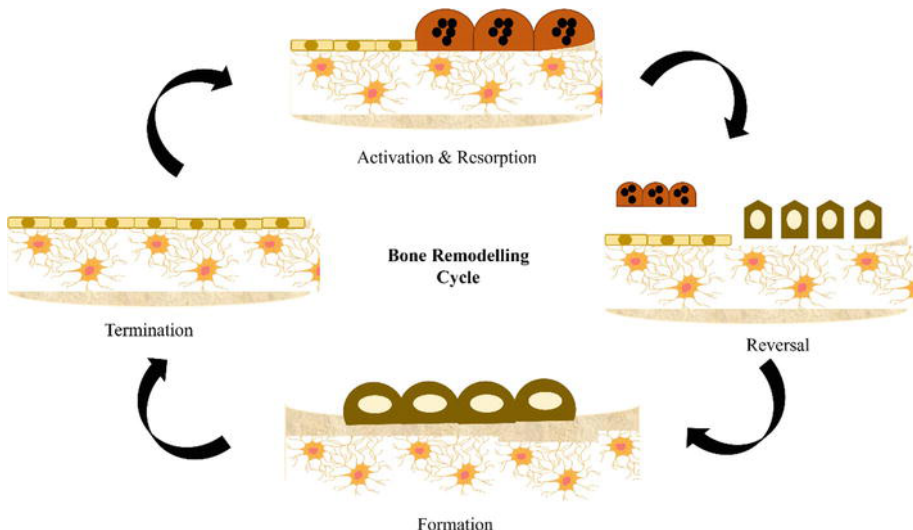


**Figure 2.** Schematic diagram of the bone remodeling cycle [83].

The remodeling cycle also applies to calcium phosphate ( $\text{CaP}$ )-based biomaterials, which must balance osteoclast and osteoblast activity for successful bone integration [84]. High  $\text{Ca}^{2+}$  concentrations, for instance, trigger the migration and differentiation of bone marrow stromal cells (BMSCs), pre-osteoblasts, and osteoblasts to resorption sites, promoting new bone formation [3]. Similarly,  $\text{Mg}^{2+}$  activates MSC differentiation and improves osteogenic cell adhesion, aiding bone healing [85]. Implants made

of Mg and Mg alloys have demonstrated positive effects on bone development in animal models, including rats, guinea pigs, and rabbits [86]. Wang *et al.* revealed that Mg<sup>2+</sup> concentration is crucial for bone formation, with 6–10 mM promoting osteoblast adhesion and proliferation, 10 mM further enhancing these effects, and 18 mM significantly inhibiting osteoblast proliferation and differentiation [87].

## 1.2. The demand for hard tissue substitutes

Biomaterials have been used throughout history to replace or repair lost body parts. As early as 2000 BC, the Egyptians used ivory to replace missing teeth and wood to create prosthetic legs, toes, and other bone substitutes [88]. As the global population ages, the demand for hard tissue reconstruction has increased significantly [89]. Although young people commonly experience fractures due to sports injuries or road accidents, older populations face bone fractures due to conditions such as osteoporosis and bone mass loss [90]. In cases where natural bone healing is not sufficient, external interventions are required [91]. Implants with osteogenic, osteoconductive, or osteoinductive properties are essential in bone grafting procedures, including the use of autografts, allografts, and synthetic substitutes.

The demand for bone implants continues to grow, with more than 400,000 bone graft surgeries performed annually in Europe and more than 600,000 in the United States [47]. According to industry reports, global sales of orthopedic products increased from \$15 billion to more than \$61.1 billion between 2002 and 2023 [47,92]. Hard tissue substitutes serve as porous scaffolds, temporary or permanent, to reduce the size of bone defects and provide structural support during the healing process [93]. Temporary substitutes are often preferred as they offer mechanical support while promoting natural tissue regeneration. These implants can be enriched with specific cells and signaling molecules to enhance tissue growth and control material degradation and absorption.

Autografts, derived from a patient's bone, are considered the gold standard due to their natural osteoconductive, osteogenic, and osteoinductive properties [74]. However, its widespread use is limited by donor site morbidity and restricted availability [89]. Allografts and xenografts, sourced from human or animal donors, provide a wider range of options but come with drawbacks such as reduced osteogenic potential, the risk of immune rejection, and disease transmission [1]. Ethical concerns and species-to-species disease transmission further limit the adoption of xenografts [93]. Given these limitations and the increasing demand for orthopedic implants, the development of advanced

synthetic materials has become imperative. Metals (such as titanium and its alloys), ceramics, polymers (both biodegradable and nonbiodegradable), and composite materials have all been explored as potential synthetic bone substitutes [90]. Furthermore, advances in bioactive coatings and surface modifications have improved the osteointegration of these materials, making them increasingly viable alternatives in clinical applications.

### 1.3. Biomaterials

A biomaterial is any natural or synthetic material designed to interact with biological systems for medical purposes, such as repairing, replacing, or improving tissue and organ function. These materials can be metals, ceramics, polymers, or composites and are used in applications such as implants, prosthetics, drug delivery systems, and tissue scaffolds [94]. The main groups of synthetic biomaterials are illustrated in Figure 3.

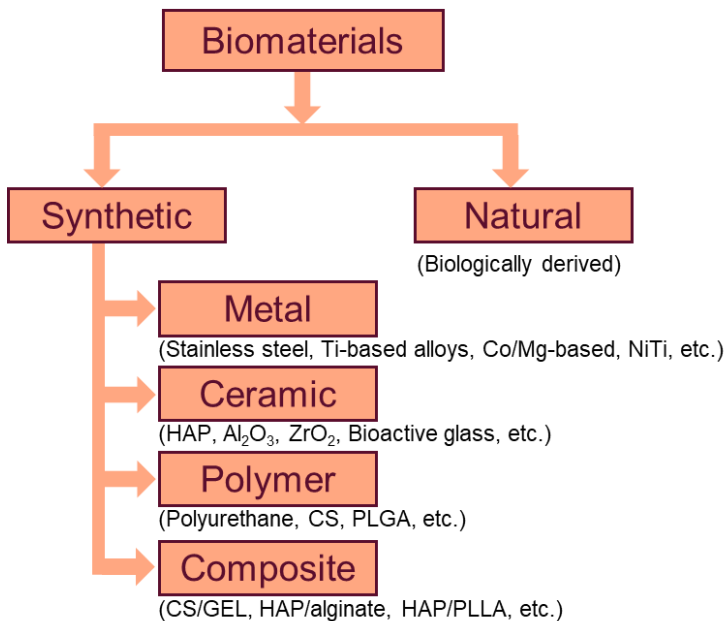


**Figure 3.** Classification of biomaterials ((CS) – chitosan. (PLGA) - poly(lactic-co-glycolic acid), (GEL) – gelatine, (PLLA) - poly-L-lactic acid).

Biomaterials are designed to be implanted in living organisms, where they interact with the body to treat injuries, replace tissues and organs, or enhance and restore biological functions [95]. They can be processed in various forms, such as molded or machined parts, coatings, fibers, films, foams, and fabrics for biomedical applications and devices [96]. Common examples include

heart valves, hip joint replacements, dental implants, skin grafts, vascular grafts, contact lenses, wound dressings, and drug delivery systems [96]. These materials must be biocompatible to avoid immune reactions, non-toxic to prevent harm to other organs, and biodegradable or bioresorbable to slowly break down and be absorbed by the body after their function [97].

### 1.3.1. CaP-based biomaterials

CaP-based biomaterials, which belong to the ceramic group, are the primary synthetic materials used in orthopedic and trauma surgery [98,99]. These compounds have a chemical composition similar to that of the inorganic phase of bone, making them excellent bone substitutes. They are characterized by biocompatibility, biodegradability, bioactivity, osteoinductivity, and osteoconductivity [1,100]. Other substances, such as calcium carbonate ( $\text{CaCO}_3$ ), calcium sulfate dihydrate (GYP,  $\text{CaSO}_4 \cdot 2\text{H}_2\text{O}$ ), and silica-based bioactive glasses, also show bioactivity, biodegradability, and osteoconductivity. However, their chemical composition does not closely resemble that of bone tissue [67].

**Biocompatibility of CaPs-based biomaterials.** CaP-based biomaterials have gained considerable scientific interest due to their biocompatibility, making them suitable for various medical applications, including bone grafts, implants, and drug delivery systems, ensuring minimal adverse effects while supporting natural healing processes [101,102]. These biomaterials interact safely with biological tissues without causing toxic, inflammatory, or immune rejection responses [103].

**Biodegradability of CaPs-containing biomaterials.** Effective bone regeneration at defect sites requires osteogenic cells, growth factors, and appropriate scaffold materials with biodegradability being a critical factor to ensure abundant new bone formation [104]. The biodegradability of CaP biomaterials enhances their biocompatibility by releasing  $\text{Ca}^{2+}$  and  $\text{PO}_4^{3-}$  ions, which activate osteogenic cells and support bone remodeling [105]. For successful bone tissue engineering, implanted graft materials must exhibit controlled degradability [106]. Obtaining a biodegradation rate that is consistent with bone resorption is essential, with factors such as granule size and sintering temperature playing key roles [1,107,108]. In vivo, the biodegradation of CaP-based biomaterials occurs through two primary pathways: passive dissolution by extracellular fluids and active cell-mediated resorption [106,109]. Generally, the rate of passive degradation depends on factors such as surface area, Ca/P ratio, crystallinity or solubility, and local pH, leading to ion dissolution and loss of mechanical integrity of implants

[1,110]. Following chemical dissolution or mechanical breakdown, the particles released from disintegrating biomaterials are absorbed by macrophages, osteoclasts, and multinucleated giant cells [110]. The speed and efficiency of cellular resorption activity depend on the size of the obtained particles: macrophages and osteoclasts (size of particles <10  $\mu\text{m}$ ), as well as giant cells (size of particles between 10 and 100  $\mu\text{m}$ ), engulf CaP biomaterials *via* phagocytosis and intracellular digestion [106]. Extracellular degradation occurs for particles larger than 100  $\mu\text{m}$ , which are processed by macrophages, giant cells of the foreign body, or through pH-lowering mechanisms established by osteoclasts [109].

**Bioactivity of CaPs-based biomaterials.** Bioactivity refers to the ability of a material to bond directly with surrounding bone tissue, influenced by chemical and physical properties (surface roughness, porosity) [67,111]. CaPs are widely recognized as bioactive compounds, which enhance bone bonding through an apatite layer at the bone-biomaterial interface [112,113]. Heughebaert *et al.* were the first to report that apatite nanocrystals can form on implanted ceramics [67]. Prof. Hench, through his studies on the bioactivity mechanisms of various biomaterials, concluded that all bioactive materials form a bone-like apatite layer on their surfaces in living organisms [114].

**Osteoinductivity.** After a fracture, bone healing is driven by osteoinduction, where immature cells become preosteoblasts to form new bone at nonosseous sites lacking osteogenic factors [1]. Urist *et al.* first demonstrated that bone formation could be induced by implanting a decalcified bone matrix or bone morphogenetic protein into the muscles of various animals [115,116]. The physicochemical composition and structure of the biomaterial critically influence its osteoinductive properties [107,108,117]. CaPs-based biomaterials such as HAP or HAP substituted with silicon ions are osteoinductive. The osteoinductive effect of CaP-based materials is most pronounced on ceramic surfaces with a macroporous structure, where the pores are interconnected rather than forming a flat surface. Porous synthetic HAP,  $\beta$ -tricalcium phosphate ( $\beta$ -TCP;  $\beta\text{-Ca}_3(\text{PO}_4)_2$ ), and porous BCP are important candidates for bone reconstruction, with osteoinductive potential classified as BCPs >  $\beta$ -TCP > HAP [67,118]. CaP-based biomaterials induce osteoinductivity by releasing  $\text{Ca}^{2+}$  and  $\text{PO}_4^{3-}$  ions into the local environment, which stimulates stem cells to migrate to the defect site, influencing their cell cycle progression and mitotic activity [119].

**Osteoconductivity.** Osteoconduction, unlike osteoinduction, is the process by which bone tissue grows along the surface or within the internal pores of an implant influenced by the material properties and the conditions of the defect site [1,120]. Osteoconductive materials support the development

of new bone on their surface or within their structure, contributing to the success of bone implants [121]. Surface modifications such as coating, gradient coating, grafting, roughening, patterning, and multilayer films improve osteoconductivity by improving cell adhesion, proliferation and migration [122]. The osteoconductivity of biomaterials can be assessed through bone coverage measurements obtained from scanning electron microscopy (SEM) images, biopsy analysis, microcomputed tomography, non-calcified histology, and histomorphometry. Increased tissue and bone cell formation on implant surfaces indicates improved osteoconductivity [1].

### 1.3.2. Variety of CaP-based bioceramics forms

CaP-based biomaterials are widely synthesized in a variety of forms, including coatings, cement, scaffolds, and granules [123]. They are commonly used to repair bone defects, treat fractures, perform total joint replacements, increase bone, and support various procedures such as orthopedic surgeries, craniomaxillofacial reconstruction, spinal surgery, otolaryngology, ophthalmology, and the use of percutaneous devices [103]. Additionally, these biomaterials are applied in dental fillings and periodontal treatments. Extensive research has been carried out to improve the properties of CaP-based materials, such as improving their bioactivity through coatings, increasing biodegradability and mechanical properties in biocomposites and hybrids, and using them for encapsulating therapeutic agents [16].

**Coatings.** CaP coatings transform non-osteconductive, load bearing implants into strong osteoconductive biomaterials [116]. These coatings are commonly applied to metallic implants to prevent corrosion and improve bioactivity [16]. Coatings can be monolayer or multilayer; In multilayer systems, the top layer ensures rapid reactivity and short immobilization time, while the bottom layer improves implant stability [103]. The thickness of the coating is crucial; excess thickness is prone to damage, while thin coatings dissolve too quickly [124]. Sol-gel and electrodeposition techniques create homogeneous, well-adherent, biocompatible CaP coatings, even on complex implant shapes [125]. Magnesium alloys have gained attention in orthopedics for their excellent mechanical and bioabsorbable properties [126]. However, their rapid degradation in aqueous and physiological environments limits their use [127]. CaP coatings in magnesium alloys help improve bioactivity, and biocompatibility, and control degradation rates [128]. Electrodeposition is particularly effective in producing CaP coatings that mimic bone structure while allowing controlled morphologies and compositions [126]. The sol-gel

method is widely used to apply thin HAP coatings on titanium alloys, improving fixation and osteointegration [129,130].

CaPs, particularly HAP and tricalcium phosphate (TCP,  $\text{Ca}_3(\text{PO}_4)_2$ ), are used as bone substitutive materials with antibacterial influence [131]. For instance, Roy *et al.* investigated the supply of silver ions, which possess antimicrobial characteristics, from TCP-coated Ti. The study demonstrated that Ag ions significantly reduced the growth of *Pseudomonas aeruginosa* and *Pseudomonas aureus* bacterial colonies by 99.99% on the silver ions-containing CaP surface in contrast to the CaP coating without Ag, without showing any cytotoxicity [132].

**Cement.** Calcium phosphate cements (CPCs) have gained scientific interest for their versatility in bone repair, augmentation, and regeneration, primarily due to their ease of handling and injectability [103]. These cements are used to fill bone defects and stabilize fractures, particularly in cases where precise molding and minimally invasive techniques are required. CPCs are formulated by mixing CaP-containing powders with water or aqueous solutions, forming a paste that hardens through a dissolution-precipitation mechanism *in vivo* [131,133]. This low temperature setting allows them to conform to defect cavities without damaging the surrounding tissues [131]. The reaction products of CPCs depend on factors such as pH, Ca/P ratio, and solubility of the initial CaPs. Most commercially available CPCs are set in apatite resembling bone mineral and offer excellent biocompatibility, osseointegration, and osteoconductivity [134]. The powder-to-liquid ratio significantly affects the injectability, setting time, and porosity of CPCs, with lower ratios leading to faster injection and longer setting times, but often compromising mechanical properties [135,136]. Despite their advantages, CPCs face challenges in clinical applications, including insufficient mechanical strength, poor injectability, and premature disintegration in blood or biological fluids due to weak cohesion [137].

**Scaffolds.** CaP scaffolds serve as a temporary bone substitute that promotes new bone formation while gradually biodegrading [138]. The first biodegradable porous  $\beta$ -TCP scaffolds were introduced in 1971, marking a key milestone in this field [123]. Effective scaffolds must mimic the extracellular matrix, supporting cell attachment, proliferation, and differentiation, while maintaining biodegradability, porosity, and an appropriate mechanical strength and degradation rate [139]. The degradation rate of the scaffold should be in sync with the rate of bone regeneration, as excessively rapid scaffold resorption can alter healing or fusion [140]. An optimal design features 30–70% porosity and pore diameters of 300–800  $\mu\text{m}$ , with mechanical properties that match spongy bone (0.5–15 MPa) [141].

Common materials used for scaffold fabrication include natural and synthetic polymers such as COLL, GEL, polycaprolactone, and PLGA [16]. Composite scaffolds that combine biodegradable polymers with CaPs are designed to improve mechanical properties [131]. For example, the incorporation of CaP particles as whiskers or spherulites within GEL or mixing CaP with COLL can significantly enhance implant strength [123]. CaP scaffolds also enable drug delivery, helping to control antibiotic release for infection prevention [138,142]. Kim *et al.* employed a dip drying technique to coat a porous HAP scaffold with a HAP and polycaprolactone composite that incorporates antibiotic tetracycline hydrochloride, while Zhang *et al.* developed a CaP composite scaffold with morphogenetic protein 2 (BMP-2) and vascular endothelial growth factor loaded on PLGA microspheres [123,131].

**Granules.** CaP-based granules are widely utilized in dental applications as bone fillers and are commercially available, mainly composed of HAP,  $\beta$ -TCP, or their BCP mixtures [40]. The effectiveness of a bone substitute depends not only on its composition but also on its structural properties [32]. Macroporous granules offer a greater advantage over dense granules for rapid bone ingrowth [143]. The macropores within the granules facilitate both bone formation and angiogenesis, while micropores enhance osteoconductivity and support new bone regeneration [144]. For example, microporous BCP granules, composed of HAP/ $\beta$ -TCP, have been successfully applied in maxillofacial surgery, implant fixation, drug delivery, anatomical remodeling, dental procedures, and overall bone repair [145]. Typically, macroporous granules are produced using gas-forming and sacrificial template methods. However, these techniques result in granules of varying sizes with unpredictable macropore distribution. The macropores often remain unconnected or closed, and their sizes frequently fall outside the optimal range for effective bone regeneration [143].

Bioceramics, such as HAP in granular form, are conventionally synthesized *via* sintering, a process that yields highly crystalline compounds but reduces their  $S_{\text{BET}}$  tissue biocompatibility [37]. Additionally, some bioceramics decompose at high temperatures required for sintering. To address these challenges, Ishikawa applied a dissolution-precipitation reaction to produce CHA granules, avoiding the problems associated with high-temperature processing while achieving excellent bone replacement outcomes. CHA is an artificial bone substitute currently used in clinical applications within the dental and maxillofacial fields, available in granular form as Cytrans® (GC, Tokyo, Japan) [32,146].

Synthetic CaP-based granules, particularly those in spherical shapes of various sizes, offer orthopedic and periodontal surgeons an effective solution to fill irregularly shaped bone defects [31].

To optimize resorption and support bone regeneration, granules should exhibit higher solubility *in vivo*. However, certain phases of CaP, such as Calcium hydrogen phosphate dihydrate (DCPD,  $\text{CaHPO}_4 \cdot 2\text{H}_2\text{O}$ , brushite) or calcium hydrogen phosphate anhydrous (DCPA,  $\text{CaHPO}_4$ , monetite), can transform into less soluble forms *in vivo*, potentially slowing their dissolution [147]. Hydrated magnesium phosphates (MPs), including struvite, K-struvite, newberyite, and amorphous MPs, have gained interest due to the role of  $\text{Mg}^{2+}$  in inhibiting HAP formation and phase transitions, resulting in a more controlled degradation process. Fuchs *et al.* implanted magnesium phosphate granules into drilling hole defects in the distal femoral condyle of white rabbits from New Zealand and observed excellent biocompatibility, rapid and continuous degradation, and effective bone regeneration [40]. Additionally, Lee *et al.* placed porous Mg-WH granules in rat calvarial defects and demonstrated that these granules significantly promoted new bone formation while maintaining excellent biocompatibility [33].

### 1.3.3. Variety of CaP-based bioceramics

Different chemical composition compounds such as HAP, TCP, DCPD and octacalcium phosphate (OCP;  $\text{Ca}_8(\text{HPO}_4)_2(\text{PO}_4)_4 \cdot 5\text{H}_2\text{O}$ ) belong to the class of CaP-based biomaterials with applications in various fields, due to the diversities in solubility, stability, and mechanical strength [105]. The selection of the appropriate CaP biomaterial from this diverse group is crucial for the effective preparation of bone regeneration materials [3]. The solubility of CaP generally depends on the stoichiometry (Ca/P ratio) and follows this order at a physiological pH of 7.4 and 25 °C: DCPD > OCP > Mg-WH >  $\beta$ -TCP > HAP [148–150]. Among these, HAP, TCP, and biphasic calcium phosphates (BCPs), which are combinations of two CaPs in varying weight ratios, are the most commonly used due to their similarity to bone tissue and their ability to promote bone formation [149].

**Hydroxyapatite.** Synthetic HAP is chemically and structurally similar to the inorganic component of bones and teeth [151,152]. The era of HAP in regenerative medicine began in the 1950s with the introduction of bioceramics as passive scaffolds for bone defect repair [153]. It is described as non-toxic, minimally inflammatory, bioactive, osteoconductive, and biocompatible, but lacks mechanical strength [149,154]. HAP is widely used in various biomedical applications, including scaffolds, powders, and coatings tailored

for specific medical purposes [155]. It is used as a bone substitute for complete or partial bone augmentation, filling bones and dental defects, and coating in orthopedic and dental implants [156]. Biodegradable and porous on the surface HAP is effectively applied in chemotherapy and antibiotic supply systems [157]. When HAP is integrated into polymer materials such as COLL, CS, and GEL, it enhances mechanical properties [158,159]. Saleem *et al.* fabricated a silk fibroin/HAP scaffold, which demonstrated more durable mechanical properties suitable for tissue engineering [159]. Element doping, heat treatment, material cladding, and other routes enhance the biological properties of HAP materials [160]. Among these, element doping stands out for its positive impact on osseous remodeling, which has been achieved using ions such as zinc (Zn), strontium (Sr), copper (Cu), Mg, manganese (Mn), and silicon (Si) [160]. HAP can be derived from both natural and synthetic sources. Natural sources include mammalian bones (e.g., bovine), marine materials (e.g., fish bones and scales), shells (e.g., seashells and eggshells), plants, algae, and minerals such as limestone [161]. Common synthesis techniques include solid state synthesis, hydrothermal processes, co-precipitation, sol-gel methods, and mechanochemical synthesis [162].

**Tricalcium phosphate (TCP).** TCP is a widely studied biomaterial in biomedicine because of its structural and chemical similarity to the mineral component of bone. Its excellent biocompatibility and bioresorbability make it an ideal candidate for applications in bone regeneration and orthopedic implants [163,164]. TCP exists primarily in two polymorphic forms:  $\alpha$ -TCP and  $\beta$ -TCP, each with distinct properties and medical uses [165].  $\beta$ -TCP material is used as an osseous graft substitute, whereas  $\alpha$ -tricalcium phosphate ( $\alpha$ -TCP) serves as a key component in the production of CaP bone cements [165–168].  $\beta$ -TCP cannot be obtained through aqueous precipitation and requires heating amorphous calcium phosphate (ACP) between 800 and 1000 °C or combining compounds such as  $\text{CaHPO}_4$  and  $\text{CaCO}_3$  (at 1000 °C for an hour) [169]. As a high-temperature phase,  $\alpha$ -TCP poses challenges in implantology due to the need for rapid cooling to preserve its structural integrity [170].

**The biphasic calcium phosphates.** BCPs were first mentioned in the late 1980s as promising materials for bone grafts, offering customizable resorption rates to support bone remodeling processes [171]. These materials typically consist of HAP and  $\beta$ -TCP in varying ratios. HAP is often chosen as the primary phase due to its chemical similarity to bone and superior mechanical properties, while  $\beta$ -TCP provides enhanced biodegradability, allowing gradual *in vivo* resorption [172]. The combination of these phases creates a balance between bioactivity and mechanical strength, making BCPs a favorable choice for hard

tissue engineering applications [173]. Their synergy supports the formation of new bone by releasing calcium and phosphate ions into the surrounding biological environment, which promotes cell attachment, proliferation, and differentiation [171,174]. BCPs are typically synthesized by sintering calcium-deficient hydroxyapatite (CDHA;  $\text{Ca}_9(\text{HPO}_4)_2(\text{PO}_4)_5\text{OH}$ ) or by mechanical mixing HAP and TCP powders [175]. These materials are available in various forms, including granules, powders, blocks, cements, and custom-made implants, depending on clinical requirements [176]. Moreover, various composites have been developed to improve both biological and mechanical properties, further broadening the clinical applications of BCPs [177].

#### 1.3.3.1. Magnesium whitlockite

Mg-WH is a CaP in which Mg partially substitutes Ca. This biomineral was mentioned as the second dominant phase in human bone, however, recent studies have found that this assertion is still unjustified, as it is claimed that Mg-WH can appear only during pathological processes [23,178]. Although the presence of Mg-WH in bone tissue remains a subject of debate, its synthetic analogue is distinguished among CaP substitutes due to the incorporation of magnesium ions in its structure. Mg ions play a crucial role in various biological functions, including the regulation of the nervous, muscular, and skeletal systems [179]. It is the fourth most abundant mineral in mammals, after sodium, potassium, and calcium [180,181]. Its allocation in the human body is as follows: 65% is found in the inorganic phase of bone, 34% is detected in the intracellular space, and 1% is in the extracellular space [182]. Deficiency of magnesium ions causes reduced bone mass, weaker bone growth, and osteoporosis [26]. Due to its important properties, many studies have been conducted on the doping of magnesium ions in HAP and TCP, which is complicated by the disparity in the radii of  $\text{Mg}^{2+}$  and  $\text{Ca}^{2+}$  ions [179,183].

Recent studies have shown that synthetic Mg-WH is superior in osteoinductivity and bone regeneration compared to HAP [184,185]. It demonstrates enhanced compressive strength and a higher resorption rate than HAP, attributed to its lower Ca/P ratio [33,186]. Mg-WH shows greater stability in the acid microenvironment created by osteoclast activity, underscoring its potential to promote bone growth and regeneration [187]. In a recent study, Lee *et al.* synthesized Mg-WH granules at 700 °C, demonstrating excellent bone regeneration capabilities without inducing any inflammatory response, effectively restoring original bone thickness in rat calvaria defects [33]. In particular, scaffolds composed of CS with

incorporated Mg-WH have demonstrated significantly enhanced bone formation compared to HAP in models of rat calvarial defects [188]. Yang *et al.* reported in 2020, that Mg-WH plays an inimitable role in improving both osteogenic and neural activities. Synthetic Mg-WH has a high surface area-to-volume ratio, enhancing cell attachment and overall biocompatibility [27,186]. Mg-WH replicates early stage bone regeneration by increasing extracellular  $\text{PO}_4^{3-}$  and  $\text{Mg}^{2+}$  concentrations and preventing osteoclastic differentiation [189]. During osseous regeneration, Mg-WH transforms into mechanically stronger HAP-neo bone tissue [190]. In very recent experiments conducted by Maximiano *et al.* Mg-WH demonstrated significant anti-inflammatory properties by reducing key inflammatory markers such as nitric oxide, tumor necrosis factor-alpha, and interleukin 6, and demonstrated promise in cancer treatment by impeding the proliferation of MDA-MB-231 breast cancer cells [191].

Mg-WH comprises a rhombohedral crystal structure ( $\text{R}3c$ ), characterized by lattice parameters  $a = b = 10.350(5)$  Å,  $c = 37.085(12)$  Å,  $\alpha = \beta = 90^\circ$ ,  $\gamma = 120^\circ$  [178,192]. The crystal structure of Mg-WH is presented in Figure 4.

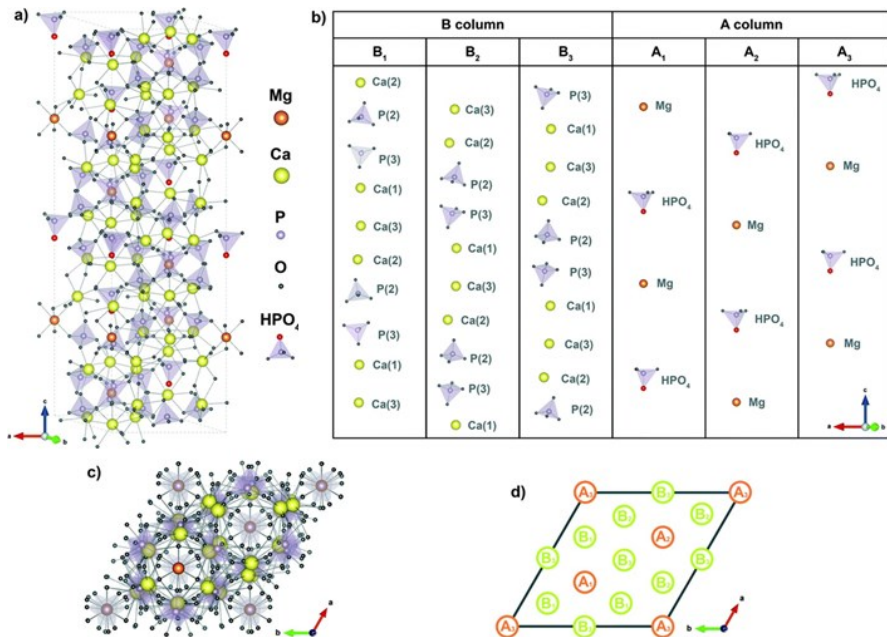


**Figure 4.** Unit cell of Mg-WH (a and c); the arrangement of atoms in structural columns (b); the arrangement of columns in unit cell (d) [193].

Two periodically arranged columns along the c-axis are identified in its structure [24]. The  $\text{Mg}^{2+}$  and  $\text{HPO}_4^{2-}$  units alternating with empty spaces fill

column A, while a recurring combination of Ca(1)–P(3)O<sub>4</sub>–P(2)O<sub>4</sub>–Ca(2)–Ca(3) packs the dense column B [193]. These columns are divided into three distinct subtypes with identical atomic positions but varying heights relative to each other along the z-axis (Fig. 4b). Each A column is encircled by six B columns of two distinct subtypes, and two A columns of different subtypes surround each B column on opposing sides and four B columns, again of two diverse subtypes (Fig. 4d). 3 A columns and 9 B columns are present in the Mg-WH unit cell. The Ca(1) and Ca(2) ions are related to five PO<sub>4</sub><sup>3-</sup> groups and one HPO<sub>4</sub><sup>2-</sup> group, and the Ca(3) ions are combined with four PO<sub>4</sub><sup>3-</sup> groups. In column A, Mg and P(1) are aligned on a straight line, as their all x and y atomic coordinates are in the value of zero. However, the B column is garbled due to the various values of the x and y atomic coordinates of Ca(1), Ca(2), Ca(3), P(2), and P(3).  $\beta$ -TCP and Mg-WH show an equal column B in their structures, while column A contains Ca<sup>2+</sup> ions at the Ca(5) and Ca(4) sites in  $\beta$ -TCP, which are replaced by Mg and H from HPO<sub>4</sub><sup>2-</sup> in Mg-WH [35].

#### 1.4. Synthesis of Calcium Phosphates

The synthesis of CaPs can be achieved through various methods, broadly classified into high-temperature and low-temperature techniques, each of which offers distinct advantages depending on the desired material properties. High-temperature methods, such as solid-state reactions, typically involve heating calcium and phosphate precursors at temperatures ranging from 750 to 1000 °C. These techniques produce highly crystalline phases, which exhibit excellent mechanical stability but slow dissolution rates, making them suitable for load-bearing applications [194,195]. For example, sintered HAP has been a significant advancement in bone defect reconstruction, but it also has limitations for certain clinical cases. Although its stability and mechanical strength are beneficial in some situations, these same properties can be a drawback in others. Specifically, sintered HAP cannot fully replace the biological functions of bone, and its high Young's modulus can lead to stress shielding, which may cause bone resorption around the implant.

Moreover, certain CaP phases, such as CHA, OCP, Mg-WH, and amorphous calcium phosphate, are thermally unstable and cannot be synthesized using high-temperature methods [35]. On the contrary, low-temperature synthesis approaches, including precipitation, dissolution-precipitation, sol-gel, hydrothermal, and biomimetic methods, allow CaP formation of CaPs under milder conditions [196]. These methods offer better control over particle size, phase composition, and surface properties, which can improve bioactivity and resorption rates [197]. Moreover, these processes

are more energy efficient and environmentally friendly compared to high-temperature approaches.

By selecting an appropriate synthesis method, researchers can tailor the physicochemical properties of CaPs to meet specific biomedical requirements, optimizing their performance for applications such as bone graft substitutes, implant coatings, and drug delivery systems.

#### 1.4.1. Dissolution-precipitation synthesis

A low-temperature dissolution-precipitation synthesis method offers a highly effective approach to the fabrication of materials with low crystallinity, high  $S_{BET}$ , and a porous structure [37]. These characteristics are essential for optimizing interactions with biological systems, making synthesized CaPs ideal for various biomedical applications. The dissolution-precipitation process unfolds in two distinct stages: first, the dissolution of the reactant occurs, followed by the precipitation of the final product [198]. This approach is commonly used to synthesize thermodynamically stable phases, such as CHA and HAP [199–201]. By carefully controlling the reaction conditions (temperature, pH, and reactant concentration), the dissolution-precipitation method allows the stabilization of metastable phases [199–202]. One such phase, OCP, is often considered to be a precursor to more stable phases such as HAP. Compared to these more stable phases, OCP can exhibit distinct advantages, including enhanced bioactivity and faster potential for bone mineralization[198].

However, achieving metastable products requires specific conditions to be met. First, the starting reactant must possess a higher solubility than the metastable phase, ensuring that the system remains in a state that allows the formation of OCP. Second, the rate of formation of the metastable phase must be faster than its transformation into a more stable phase, such as HAP. In 2018, Sugiura *et al.* published the fabrication of porous OCP foam through a dissolution-precipitation reaction [202]. In vivo studies demonstrated that OCP foam elicited an excellent tissue response, promoting bone growth in its porous structure. Its osteoconductivity and bone replacement rate were significantly higher compared to those of nonporous OCP. Furthermore, OCP blocks were successfully synthesized by dissolution-precipitation from DCPD blocks immersed in a phosphate-rich solution, while maintaining their macroscopic structure, as well as calcium sulphate hemihydrate (CSH;  $\text{CaSO}_4 \cdot 0.5\text{H}_2\text{O}$ ) blocks [198,203].

A major advantage of the dissolution-precipitation method is its ability to retain the shape of the initial reactants in the final product, making it particularly useful for the fabrication of structures with precise geometries [199]. Using this method, bone substitutes have been produced from various initial materials, such

as calcite ( $\text{CaCO}_3$ ), calcium sulfate ( $\text{CaSO}_4$ ),  $\alpha$ -TCP, DCPD blocks [200,204,205]. During the process, consecutive dissolution-precipitation reactions facilitate the gradual transformation of precursor materials into specific CaP. As the reaction progresses, newly precipitated apatite crystals interlock at the microscopic level, creating a dense and cohesive structure. The dissolution-precipitation method is valued for its ability to retain the shape of the initial reactant, however, complete shape preservation is not always guaranteed. Reaction conditions such as pH, temperature, and ion concentration significantly impact shape retention. Rapid or uneven dissolution can cause deformation before precipitation restores the structure. Highly porous materials may shrink or collapse, while phase transitions can lead to slight expansions or contractions. Uneven nucleation and crystal growth may introduce distortions, and mechanically weak precursors are susceptible to deformation during handling. Therefore, careful optimization of reaction parameters enables a high degree of shape retention while improving the bioactivity and mechanical properties of CaP materials [199].

In a 2010 study, Ishikawa *et al.* successfully demonstrated the transformation of a  $\text{CaCO}_3$  block into CHA [37]. In this reaction, calcite was dissolved, releasing  $\text{Ca}^{2+}$  and  $\text{CO}_3^{2-}$  ions, which, in the presence of  $\text{PO}_4^{3-}$  ions, led to the formation of CHA due to its significantly lower solubility. The precipitated CHA was identified as B-type carbonate apatite, naturally found in bone. CHA granules synthesized *via* the dissolution-precipitation method were implanted into bone defects (see Figure 5). They promoted new bone formation, resembling the behavior of autografts.



**Figure 5.** Histological pictures of CHA after implantation in a bone defect made in the cranial bone of rats (figure adapted from [37]).

#### 1.4.2. Synthesis Methods and potential application fields of Mg-WH

Due to the complexity of its synthesis, Mg-WH is widely believed to be under-researched in terms of its properties, functions, and behavior in the human body [24,27]. Monitoring pH,  $Mg^{2+}$  ion concentration, and temperature during the synthesis process is critical to achieving the successful formation of pure-phase Mg-WH, as deviations can lead to the formation of intermediate CaP phases, including DCPD, DCPA, OCP, and HAP [29,34]. A variety of products can be obtained through different methods of Mg-WH synthesis, including powders, granules, coatings on  $\beta$ -TCP ceramics, various composites, and a variety of morphologies and particle sizes [35,206].

The researchers classify the synthesis of CaPs into wet and dry methods [207]. For Mg-WH fabrication, wet methods include techniques such as precipitation, hydrothermal processing, microwave-assisted hydrothermal synthesis, dissolution-precipitation, dissolution-precipitation under hydrothermal conditions, and solid-liquid-solution (SLS) process [22,178,188,208–210]. On the other hand, dry synthesis methods mainly involve the solid-state approach [179,211].

Due to the instability of Mg-WH at high temperatures, wet synthesis, particularly the **precipitation method**, remains the most commonly used fabrication technique [24,35,201]. In 2013, Jang *et al.* reported the precipitation synthesis of Mg-WH under acidic conditions in a simple ternary  $Ca(OH)_2$ – $Mg(OH)_2$ – $H_3PO_4$  aqueous system with a controlled excess of  $Mg^{2+}$  ions. They highlighted the critical role of pH control and the precise addition of  $Mg^{2+}$  ions to prevent the formation of HAP and other intermediate CaP phases during the synthesis of the Mg-WH phase [24]. To better understand the transitional phases and clarify the precipitation mechanism of the Mg-WH compound, the reaction pH was systematically varied from basic to neutral and then acidic, thereby dividing the process into distinct sequential stages [34]. During the process, the pH of the system experienced significant changes, fluctuating from 11.2 to 5.8, then from 5.8 to 4.5, and finally from 4.5 to 3.5. In stage I, HAP and  $Mg(OH)_2$  were the primary phases of the precipitate, as shown in Figure 6.

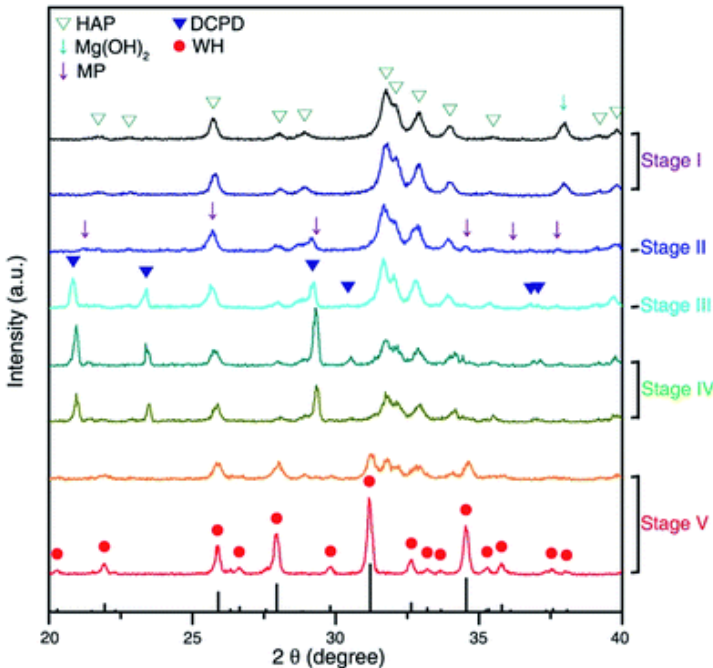


**Figure 6.** XRD pattern of intermediate precipitants collected during the synthesis of Mg-WH. The peaks corresponding to each phase of HAP,  $\text{Mg}(\text{OH})_2$ , MP, DCPD, and Mg-WH in the XRD data are marked as the green triangle, the cyan arrow, the purple arrow, the navy triangle, and the red circle, respectively [34].

In stage II, as  $\text{Ca}(\text{OH})_2$  was nearly depleted,  $\text{Mg}(\text{OH})_2$  began to react with  $\text{H}_3\text{PO}_4$ , leading to the formation of XRD peaks corresponding to dimagnesium phosphate (MP,  $\text{MgHPO}_4 \cdot x\text{H}_2\text{O}$ ). As the system became more acidic in stage III, partial conversion of HAP to the DCPD phase was observed. When the total amount of  $\text{H}_3\text{PO}_4$  was added, the presence of HAP, DCPD, and MP phases was confirmed. In stage IV, during aging in the acidic solution at a pH of 3.3, HAP, DCPD, and MP underwent gradual dissolution, while the XRD peak intensities of the Mg-WH phase increased during the 5-hour aging period. Finally, in stage V, after 24 h of aging, only the pure Mg-WH phase remained. In 2017, Kim *et al.* conducted a study examining the conversion of Mg-WH compounds to HAP synthesized by the precipitation method and its effect on bone regeneration [29]. They compared the surface characteristics of Mg-WH and HAP, analyzed the kinetics of ionization, assessed the stability of resorption, and evaluated other key properties relevant to bone regeneration. The researchers found that Mg-WH facilitates bone regeneration by enhancing osteogenic differentiation while inhibiting osteoclast activity,

which is attributed to the presence of phosphate and magnesium ions in its structure. As a result, it promotes the formation of denser neobone tissue.

Pillai *et al.* utilized the precipitation method to synthesize Mg-WH and develop an Mg-WH compound with CS for hemostasis [208]. Compared to a standalone CS hydrogel and commercial hemostatic agent, the composite demonstrated injectability, cytocompatibility, and hemocompatibility. In vitro (blood clot test) and in vivo (hemostasis tests on rat liver and femoral artery injuries) studies confirmed its superior hemostatic performance. The authors concluded that Mg-WH nanoparticles (NPs) improve hemostasis by promoting rapid and effective coagulation through calcium, magnesium, and phosphorus ions, forming a stable plug at the injury site.

In 2021, Kaliannagounder *et al.* synthesized Mg-WH NPs with piezoelectric properties, essential to enhance osteogenic differentiation and mimic the bioelectric fields of natural bone, using a modified precipitation method based on Jang *et al.* [29,30]. The noncentrosymmetric structure of Mg-WH enables its piezoelectric properties, allowing it to function as a self-induced electrical nanogenerator and biosensor. Further experiments showed that Mg-WH annealed at 750 °C exhibited improved ferroelectric and dielectric properties. When exposed to low-intensity pulsed ultrasound in a noninvasive manner, these annealed samples generated electrical signals similar to those found in natural tissue, reinforcing their potential for enhanced osteogenic differentiation.

Amirthalingam *et al.* recently used the precipitation technique to incorporate Mg-WH or bioglass NPs, along with human fibroblast growth factor-18 (FGF-18), into an injectable hydrogel [212]. Their study aimed to evaluate the bioproperties of these formulations compared to a commercial hydrogel containing HAP NPs with FGF-18. Mg-WH maintained the injectability of the hydrogel, while FGF-18 slightly reduced its flow. Nano-Mg-WH stimulated angiogenesis, promoting new blood vessel formation. Mg-WH with FGF-18 exhibited the strongest osteogenic differentiation through a synergistic effect. In vivo, implantation studies confirmed its superior bone regeneration potential, outperforming HAP NPs and bioglass NPs with FGF-18, as the defect site was nearly filled with new bone tissue.

In 2022, Du *et al.* synthesized Mg-WH using a precipitation method to evaluate its potential for bone tissue engineering [213]. The Mg-WH was incorporated into a polyurethane matrix to fabricate a composite scaffold, which demonstrated excellent suitability for bone regeneration. The scaffold was biocompatible, nontoxic, elastic, and porous, with compressive strength comparable to human spongy bone.

Awan *et al.* synthesized Mg-WH powder with various morphologies using a precipitation method [167]. Morphological diversity was achieved by adjusting the pH, reactant concentration, temperature, and reaction time. The pH control produced irregular plate-shaped Mg-WH (121–263 nm), while the temperature influenced cubic, spherical, and rectangular shapes (76.4–263 nm). Extended reactions led to clustering (516 nm – 1  $\mu$ m). The study concluded that temperature and pH are key factors in the morphology of Mg-WH, broadening its potential for bone regeneration materials.

The **hydrothermal approach** is a crucial method for the synthesis of Mg-WH, allowing the production of CaPs with diverse morphologies and compositions under high-temperature and high-pressure conditions [214]. A.C. Tas manufactured Mg-WH using a hydrothermal method using a DCPD precursor [215]. Specifically, 0.35 g of DCPD was suspended in 100 ml of 1.5 mM MgCl<sub>2</sub>, ultrasonicated for 1 minute, and aged in a controlled oven at 70 °C for 1 day, 150 °C for 1 day, and 37 °C for 21 days, resulting in the conversion flat plate morphology of DCPD to Mg-WH hexahedral crystallites, as confirmed by SEM and EDX, with additional phases (DCPA, OCP, apatitic CaP, and biphasic compounds) forming under varying conditions (see Figure 7).

Konishi *et al.* employed a hydrothermal method to synthesize Mg-WH in just 3 h, with the reaction conducted in a solution of 1 mol/L HCOOH, 10 mmol/L MgCl<sub>2</sub>, and 0.8 g DCPD under 2.3 MPa at 220 °C, resulting in a homogeneous product, while a reduction in the concentration of MgCl<sub>2</sub> resulted in a biphasic mixture of DCPA and Mg-WH [214]. Stefanovich *et al.* recently synthesized Mg-WH using a hydrothermal method [216]. High-quality single crystals (~1 mm) were manufactured using DCPD, NaCl, and Mg(NO<sub>3</sub>)<sub>2</sub> in a 4:1:1 ratio.

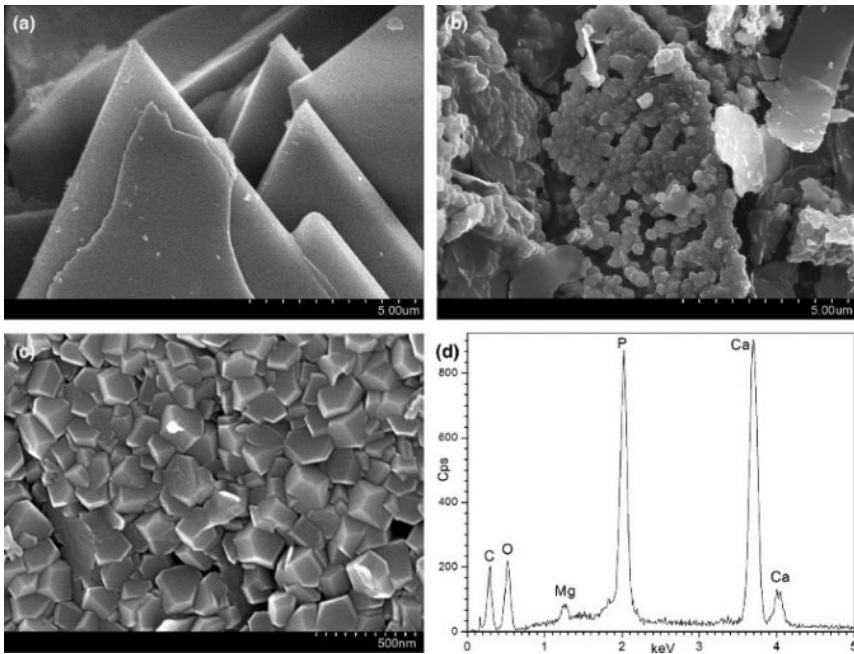


**Figure 7.** (a) SEM image of DCPD crystals, (b) and (c) SEM image of Mg-WH crystals, (d) EDX spectrum of Mg-WH crystals [215].

Maximiano *et al.* synthesized Mg-WH NPs using a hydrothermal method to explore their anti-inflammatory and anticancer potential [191]. Biological tests showed that Mg-WH NPs reduced inflammatory markers and inhibited breast cancer cell proliferation.

The **microwave-assisted method** offers faster synthesis, uniform heating, improved energy efficiency, and greater effectiveness compared to traditional heating techniques [217,218]. Qi *et al.* reported the microwave-assisted synthesis of porous hollow Mg-WH microspheres [219]. Aqueous solutions of 100 mM CaCl<sub>2</sub>, 100 mM MgCl<sub>2</sub>·6H<sub>2</sub>O, and 60 mM creatine phosphate disodium salt were mixed in deionized water and stirred at room temperature. The mixture was then microwaved at 120 °C for 10 minutes. A Ca/Mg molar ratio of 7:3 was required for single-phase Mg-WH; other CaPs formed in different ratios. The optimal reaction temperature for hollow porous microspheres was 150 °C; higher temperatures led to larger polyhedral structures. Mg-WH exhibited high stability in physiological and phosphate buffered saline, excellent biocompatibility, and enhanced adhesion and spreading. Its sustained and controlled drug release supports long-term chemotherapeutic efficacy, suggesting potential use in various biomedical applications.

**Microwave-assisted hydrothermal synthesis** combines traditional hydrothermal methods with microwave heating, offering advantages such as faster processing, high efficiency, and economic feasibility, making it particularly effective in the production of CaP compounds [218,220]. In 2016, Qi *et al.* synthesized single-phase Mg-WH hollow microspheres using fructose 1,6-bisphosphate through conventional and microwave-assisted hydrothermal methods for comparison [221]. The XRD results showed faster and higher crystallinity product formation with microwave-assisted synthesis (see Figure 8). The products exhibited excellent biocompatibility and protein adsorption capacity, making them suitable for biomedical applications.

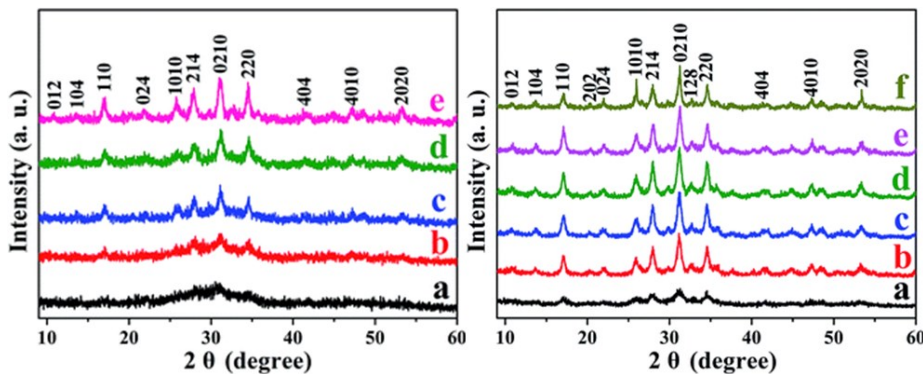


**Figure 8.** XRD patterns: The left image shows products synthesized using the microwave-assisted hydrothermal approach under different circumstances: (a) 120 °C for 10 min; (b) 120 °C for 60 min; (c) 140 °C for 10 min; (d) 160 °C for 10 min; (e) 180 °C for 10 min, while the right image presents products synthesized employing a conventional hydrothermal approach at 180 °C for different durations: (a) 1 h; (b) 2 h; (c) 4 h; (d) 7 h; (e) 12 h; (f) 24 h [221].

Zhou *et al.* used a microwave-assisted hydrothermal method to fabricate Mg-WH scaffolds with CS for bone restoration and compared their biological properties [188]. Prepared scaffolds promoted human MSC proliferation, osteogenic differentiation, and improved biocompatibility in rat calvarial defects, outperforming scaffolds made of HAP and CS. The Mg-WH scaffold (macropores of 105 µm) showed better bone repair ability than both nonporous and porous scaffolds made of HAP and CS. Another instance of microwave-assisted hydrothermal synthesis to produce Mg-WH microspheres with nanopores for the investigation of their capacity to adsorb heavy metals was provided by Lin in 2019 [222]. The low crystallinity, high SBET Mg-WH with nanopores exhibited strong adsorptive properties for Pb<sup>2+</sup> ions, achieving

adsorption equilibrium in a 200 mg/L Pb<sup>2+</sup> solution in 5 min. Additionally, Mg-WH can selectively adsorb Pb<sup>2+</sup> ions from a mixture of Cd<sup>2+</sup>, Cu<sup>2+</sup>, and Pb<sup>2+</sup> ions. These findings indicate that porous Mg-WH microspheres could be used effectively in the treatment of water contaminated with heavy metals such as Pb<sup>2+</sup> ions.

Another promising approach for synthesizing Mg-WH is the ***dissolution-precipitation method***, which is both cost-effective and time-efficient. This straightforward technique allows for easy control over the reaction conditions and the synthesis process. The simplicity of this method reduces the need for complex equipment, making it an attractive option for the large-scale production of Mg-WH materials, while also minimizing energy consumption and reaction time [37,201,223]. A. Afonina *et al.* used the dissolution-precipitation method to synthesize Mg-WH powders with varying Ca/Mg molar ratios (15, 12, 10, 8, 6, and 4). DCPD and magnesium acetate tetrahydrate ( $\text{Mg}(\text{Ac})_2$ ) were dissolved in an aqueous solution of phosphoric acid. After adjustment of pH to 5.6 with ammonia, the reaction mixture was stirred at 65 °C for 24 h, followed by vacuum filtration, washing, and drying at 60 °C. The chemical composition and the morphology of the synthesized material were adjusted by the Ca/Mg molar ratio in the initial synthesis solution. Pure samples were obtained in Ca/Mg ratios of 12, 10, 8, 6, and 4, while a biphasic sample with CDHA was found in Ca/Mg=15.

In 2023 A. Afonina *et al.* applied the dissolution-precipitation method to study the formation of Mg-WH from GYP under static and rotating conditions (see Figure 9) [178]. The target phase was derived from GYP through intermediate products within 12 h. Rotating conditions favored smaller Mg-WH crystals (16 nm) compared to static conditions (30 nm). Rietveld refinement of the 12h and 24h samples showed slight changes in lattice parameters, magnesium occupancy, and lattice volume. However, the synthesis conditions (static versus rotating) had a greater impact on crystallite size, crystallinity, and structural parameters. These findings highlight the influence of reaction time and conditions on the formation, composition, and properties of Mg-WH, offering insights into the control of material properties.

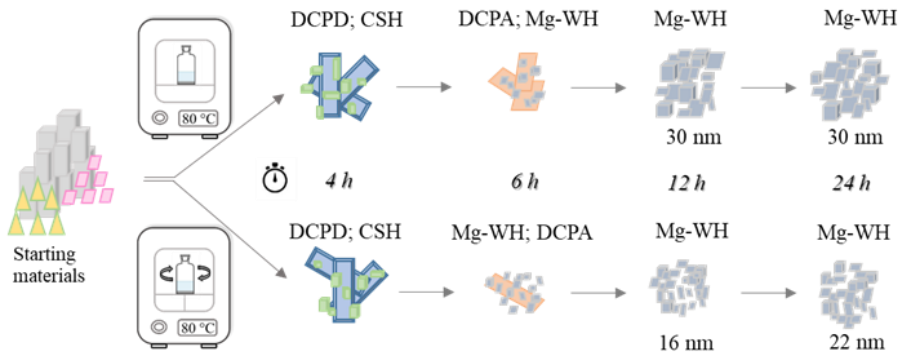


**Figure 9.** Schematic representation of the formation of Mg-WH NPs using the dissolution-precipitation method under static and rotating conditions [178].

Kizalaite *et al.* studied the **dissolution-precipitation synthesis** of Mg-WH powder **under hydrothermal conditions** [180], focusing on its thermal degradation. To synthesize Mg-WH, DCPD and Mg(Ac)<sub>2</sub> were mixed to achieve a Ca/Mg molar ratio of 9, dissolved in 50 mL deionized water and 5.6 mL 1 M phosphoric acid. The pH was adjusted to 6.4 with ammonia and the mixture was heated at 160 °C for 3 h. The product was then heated over the temperature intervals of 400 to 1300 °C (see Figure 10). It was found that Mg-WH began decomposing at 700 °C, forming β-TCP and Ca<sub>2</sub>P<sub>2</sub>O<sub>7</sub> polymorphs. These results highlight that high-temperature methods are not suitable for producing pure Mg-WH bioceramics.

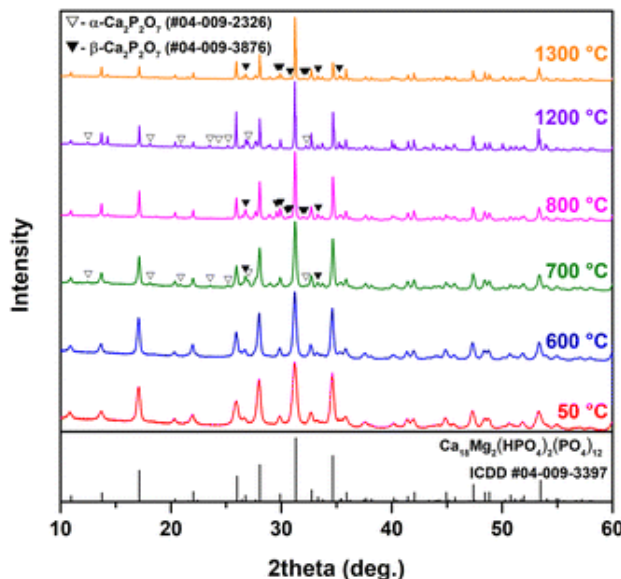


**Figure 10.** XRD patterns of Mg-WH powder heated at various temperatures [35].

The ***solid-liquid-solution (SLS) method***, first described by Wang *et al.* in 2020, offers precise control over the size, morphology (nanoplates, nanospheres), and surface properties (hydrophobic, hydrophilic) [22]. This approach enables the reaction at the liquid-solid-solution interfaces, improving traditional precipitation methods. For synthesis, oleic acid, ethanol, and NaOH were mixed, followed by the addition of CaCl<sub>2</sub>, MgCl<sub>2</sub>, and Na<sub>2</sub>HPO<sub>4</sub> in varying ratios. The mixture was stirred for 30 min, heated at 200 °C for 12 h, then cooled, washed with ethanol, and vacuum-dried. Reactant ratios and ethanol concentration influenced crystallinity, morphology, and diffusion rates. Mg-WH demonstrated potential in osteogenic differentiation of human MSCs, making it promising for bone tissue engineering.

Later, Lee *et al.* introduced a fabrication method for interconnected porous Mg-WH granules, employing vacuum filtration followed by sintering of Mg-WH synthesized by the SLS method [33]. The authors also conducted a detailed investigation into its potential to promote the healing of osseous tissue (Figure 11).

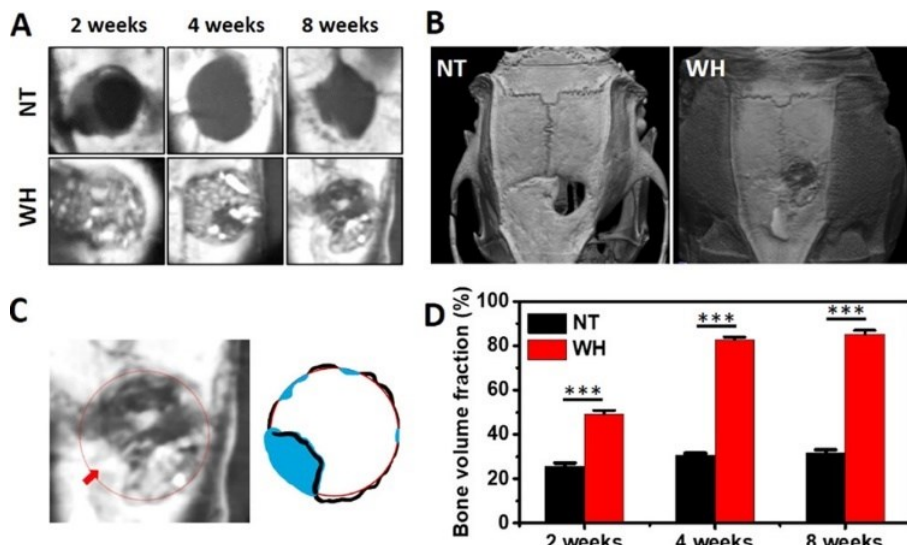


**Figure 11.** (A) 3D μ-CT horizontal images of rat calvaria in nontreated (NT) and Mg-WH (WH) groups 2–8 weeks after implantation. (B) 3D μ-CT image of the rat calvaria in the NT (left image) and Mg-WH (right image) group at 8 weeks after surgery. (C) New bone formation (left, marked with red arrow) was observed around the Mg-WH granule. The blue areas in the circles represent a newly formed bone (right). (D) Bone volume fraction (%) at 2–8 weeks (\*\*\*(P < 0.001) [33].

This study highlighted the significant bone healing potential of Mg-WH granules, demonstrating their excellent biocompatibility and osteogenic capacity. The absence of inflammation or foreign body reactions, along with the formation of new bone at the original thickness, underscored its suitability for bone regeneration. Furthermore, Mg-WH granules enhanced osteogenesis by promoting the expression of key bone-related proteins without the need for exogenous cells or growth factors. These findings suggested that Mg-WH holds great promise for applications in bone tissue engineering, particularly in the regeneration of human bone and the reconstruction of alveolar bone deficiencies in oral and maxillofacial surgery.

## 2. EXPERIMENTAL PART

### 2.1. Reagents

The following reagents were used in this study: calcium sulphate dihydrate (gypsum,  $\text{CaSO}_4 \cdot 2\text{H}_2\text{O}$ , 99%, Sigma-Aldrich), magnesium acetate tetrahydrate ( $\text{Mg}(\text{CH}_3\text{COO})_2 \cdot 4\text{H}_2\text{O}$ ,  $\text{Mg}(\text{Ac})_2$ , 98%, Roth), disodium hydrogen phosphate ( $\text{Na}_2\text{HPO}_4$ , 98%, Merck), sodium dihydrogen phosphate ( $\text{NaH}_2\text{PO}_4$ , 99%, Merck), ammonium dihydrogen phosphate ( $\text{NH}_4\text{H}_2\text{PO}_4$ , ≥99%; Chempur), diammonium hydrogen phosphate ( $(\text{NH}_4)_2\text{HPO}_4$ , ≥99%; Chempur), magnesium hydrogen phosphate trihydrate ( $\text{MgHPO}_4 \cdot 3\text{H}_2\text{O}$ , 99%; Alfa Aesar), and deionized water.

### 2.2. Synthesis methodology

#### 2.2.1. Large-scale synthesis of Mg-WH powders: influence of reaction time

GYP,  $\text{Mg}(\text{CH}_3\text{COO})_2 \cdot 4\text{H}_2\text{O}$ ,  $\text{Na}_2\text{HPO}_4$ , and  $\text{NaH}_2\text{PO}_4$  were used as starting materials for the fabrication of Mg-WH powders *via* a dissolution-precipitation reaction. The representation of the main synthesis stages is shown in Figure 12. To begin the synthesis, 5.00 g of GYP was placed in a glass bottle, followed by the addition of 31.25 mL of 0.233 M  $\text{Mg}(\text{Ac})_2$  and a mixture of 250.0 mL each of 1.00 M  $\text{Na}_2\text{HPO}_4$  and 1.00 M  $\text{NaH}_2\text{PO}_4$  solutions.

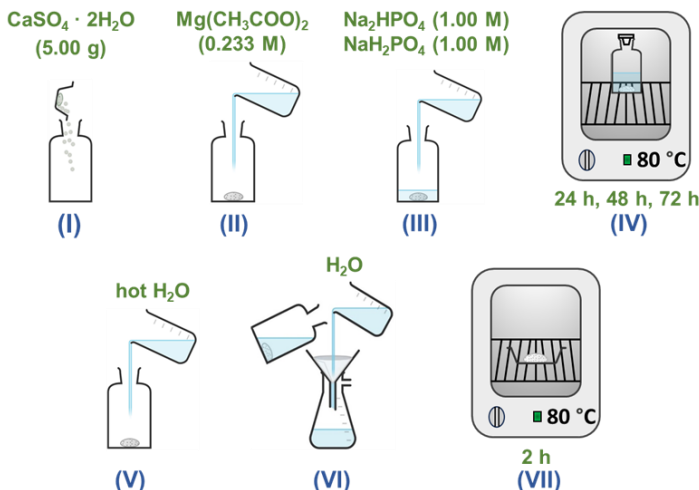


**Figure 12.** Scheme of Mg-WH powder synthesis: GYP powder was mixed with  $\text{Mg}(\text{Ac})_2$ , and phosphate solutions (I–III) and placed in an oven (IV). After synthesis, the product was decanted, washed with hot water (V), rinsed with water and vacuum-filtered (VI), and dried in an oven (VII).

The pH of the resulting mixture was determined as 6.2. Such a pH value promotes the formation of Mg-WH and prevents the formation of other CaPs, because pH is one of the key factors influencing the precipitation of particular CaP phases. The sealed bottle was subsequently placed in an oven at 80 °C for 24 h, 48 h, and 72 h allowing the reaction to progress. After synthesis, the liquid phase was decanted from the bottle, and the resulting powder was rinsed with 500 mL of hot (~80 °C) deionized water, followed by several additional rinses with 250 mL of room-temperature deionized water. Finally, the vacuum-filtered product was dried at 80 °C for 2 h. This meticulous procedure ensures precise control and sequential execution of each stage, contributing to the reproducibility and reliability of Mg-WH powder synthesis.

#### 2.2.2. Large-scale synthesis of Mg-WH granules: the effect of reaction pH on phase composition

CSH obtained by heating GYP at 150 °C for 5 h, at a speed of 5 °C/min., served as the Ca<sup>2+</sup> source. For the preparation of GYP granules (see schematic representation in Figure 13a), 20.0 g of CSH was homogenized with 8.00 g of NH<sub>4</sub>H<sub>2</sub>PO<sub>4</sub> and mixed with 12.0 mL of deionized water.

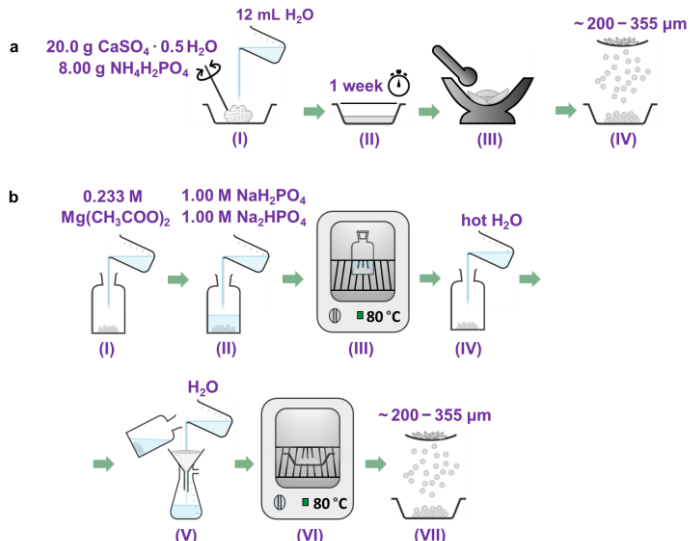


**Figure 13.** Scheme of Mg-WH granule synthesis: (a) CSH powder are mixed with NH<sub>4</sub>H<sub>2</sub>PO<sub>4</sub> and water, solidified, crushed, and sieved to obtain GYP granules (I–IV), and (b) GYP granules are mixed with Mg(Ac)<sub>2</sub>, phosphate solutions, and reacted in an oven (I–III). The liquid was decanted, the granules were washed with hot water, room-temperature water, vacuum-filtered, dried, and sieved to obtain Mg-WH granules (IV–VII).

The resulting viscous mass was thoroughly mixed and left at room temperature for a week. The solidified sample was then broken into small pieces, crushed in an agate mortar, and sieved to collect granules of the size of  $\sim$ 200 – 355  $\mu\text{m}$ . The final Mg-WH granules were synthesized using a dissolution-precipitation method, as illustrated in Figure 13b. To synthesize Mg-WH, in addition to GYP granules,  $\text{Mg}(\text{Ac})_2$ ,  $\text{NaH}_2\text{PO}_4$ , and  $\text{Na}_2\text{HPO}_4$  were selected as source materials. Specifically, 3.00 g of GYP granules were placed in a bottle and mixed with 15.00 mL of 0.233 M  $\text{Mg}(\text{Ac})_2$  solution. Subsequently, 3 different types of solutions were added to the bottle: 75.0 mL of 1.00 M  $\text{Na}_2\text{HPO}_4$  and 225.0 mL of 1.00 M  $\text{NaH}_2\text{PO}_4$  (the resulting granules were named as 1GR); 150.0 mL of 1.00 M  $\text{Na}_2\text{HPO}_4$  and 150.0 mL of 1.00 M  $\text{NaH}_2\text{PO}_4$  (granules were named as 2GR); 225.0 mL of 1.00 M  $\text{Na}_2\text{HPO}_4$  or 75.0 mL of 1.00 M  $\text{NaH}_2\text{PO}_4$  (granules were named as 3GR). The sealed bottles were then placed in an oven and kept at 80 °C for 5 days to facilitate the progression of the reaction. After the synthesis, the liquid in the bottles was decanted, and the granules were washed with hot deionized water (approx. 80 °C; 500 mL), vacuum filtered, again washed with deionized water (500 mL) at room temperature, and dried in the oven for 12 h at 80 °C. Finally, the resulting samples were sieved to collect the product of  $\sim$ 200 – 355  $\mu\text{m}$  in size.

### 2.2.3. Synthesis of Mg-WH granules with different morphology through variations in precursor compositions

Mg-WH granules were fabricated through a dissolution-precipitation reaction, as illustrated schematically in Figure 14. Calcium sulphate (CASU;  $\text{CaSO}_4$ ), used as the  $\text{Ca}^{2+}$  source, was selected as the starting material, which was prepared by heating GYP at 170 °C for 5 h. Initially, three types of precursor granules with different chemical compositions were synthesized: monophasic (R1) and mixed (R2, and R3) granules. Monophasic precursor granules R1 were prepared by thoroughly mixing 20.0 g of CASU with 12 mL of deionized water. Mixed granules R2 were prepared by homogenizing 20.0 g of CASU with 8.0 g of  $(\text{NH}_4)_2\text{HPO}_4$  and then mixing with 12 mL of deionized water. Mixed granules R3 were prepared by homogenizing 20.0 g of CASU with 8.0 g of  $(\text{NH}_4)_2\text{HPO}_4$  and 4.0 g of  $\text{MgHPO}_4 \cdot 3\text{H}_2\text{O}$ , then mixing with 12 mL of deionized water. The R1–R3 samples were kept at room temperature for a week to allow the solidification process to occur. Then, solidified samples were crushed in an agate mortar and sieved to obtain granules with a size of approximately 200 – 355  $\mu\text{m}$ .

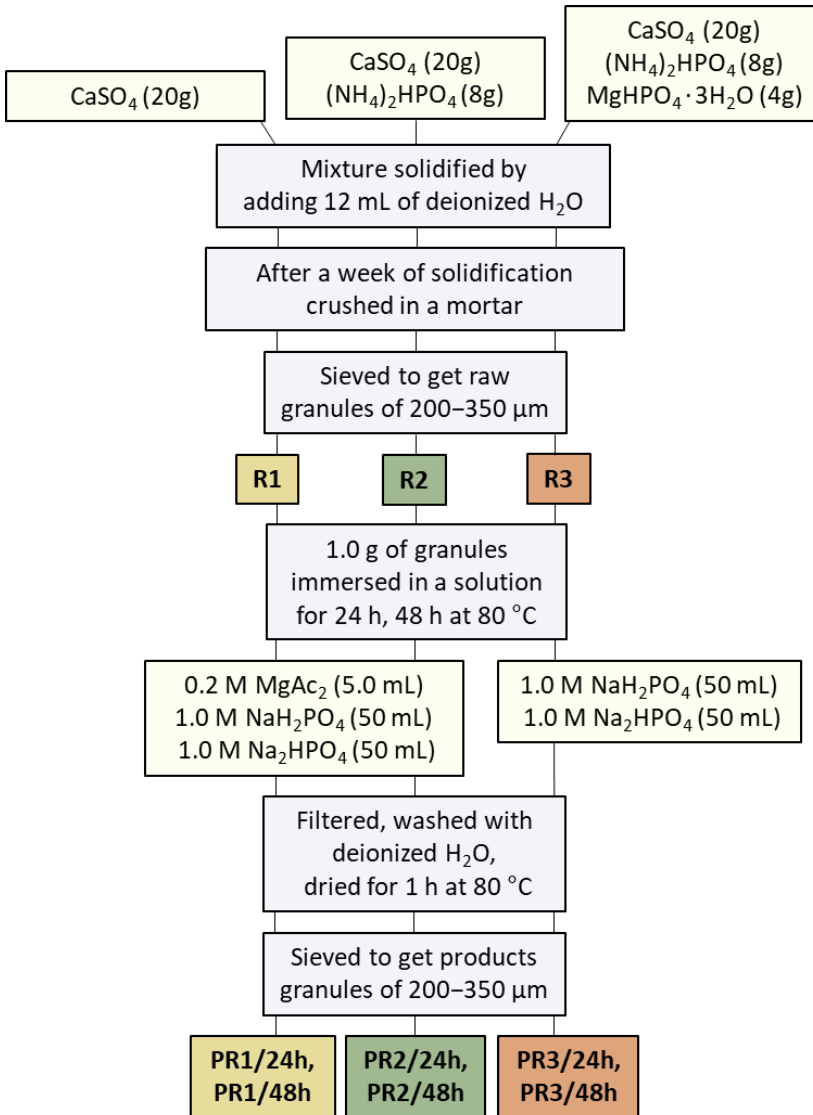


**Figure 14.** The following schematic diagram illustrates the preparation process of the raw R1–R3 granules, which are later converted into the final product, PR1/24h, PR1/48h, PR2/24h, PR2/48h, PR3/24h, and PR3/48h granules.

The synthesis of the Mg-WH product granules from R1 and R2 precursor granules was carried out as follows: 1.0 g of each sample was mixed with a 0.20 M Mg(Ac)<sub>2</sub> solution (0.20 g Mg(Ac)<sub>2</sub> dissolved in 5.0 mL of water) (see Figure 14). Then, 50 mL of 1.0 M NaH<sub>2</sub>PO<sub>4</sub> and 50 mL of 1.0 M Na<sub>2</sub>HPO<sub>4</sub> solutions were added sequentially. The mixture was placed in a capped bottle

and kept in a drying oven at 80 °C for 24 h and 48 h. The synthesis of Mg-WH from R3 granules followed the same procedure, except that adding the Mg(Ac)<sub>2</sub> solution was omitted. After 24 h and 48 h, all synthesized samples were filtered, washed several times with deionized water, and dried in the oven at 80 °C for 1 h. The samples were then sieved to collect granules of approximately 200 – 355 µm in size. Granules synthesized from R1, R2 and R3 granules for 24 h and 48 h were named PR1/24h, PR2/24h, PR3/24h, PR1/48h, PR2/48h, and PR3/48h granules, respectively.

## 2.4. Characterization

The prepared samples were characterized by XRD analysis using a Rigaku MiniFlex II diffractometer (Tokyo, Japan) equipped with CuK $\alpha$  radiation ( $\lambda = 1.541838 \text{ \AA}$ ) over a 2 $\theta$  ranges of 10 – 60° or 10 – 70° scanning angles. All XRD patterns were recorded using the following measurement conditions: a tube voltage of 30 kV, a tube current of 15mA, and a step scan mode with a step size of 0.02° at a scan speed of 2°/min. Crystalline phases identification was achieved through a comparative analysis of the obtained diffraction patterns with the database standards provided by the International Center for Diffraction Data (ICDD). The single-phase Mg-WH samples endured Le Bail structure refinement with FullProf software. Rietveld refinement was applied to quantitatively determine the phases present in multiphasic samples using the FullProf software. In addition, some multiphasic compounds were subjected to a thorough semi-quantitative analysis, a process intricately executed through the normalized corundum reference intensity ratio (RIR) method facilitated by the Match! (version 3.13; Dr. Holger Putz, Crystal Impact, Bonn, Germany). Standard lanthanum hexaborate (LaB<sub>6</sub>) measurements were performed to account for instrumental broadening, which is essential to eliminate its contribution from the width of the experimental diffraction peak and to ensure an accurate determination of the crystallite size [224]. To evaluate the crystallinity of the fabricated Mg-WH samples, considering the presence of both crystalline and amorphous phases in the experimental XRD pattern, the analysis was carried out using a zero-background Si sample holder with the assistance of the aforementioned XRD apparatus and Match! software (<https://www.crystalimpact.com/match/>).

A Fourier transform infrared spectrometer with attenuated total reflectance (FT-IR/ATR) (Appha Bruker, Inc., Germany) was used to obtain FT-IR spectra of the synthesized samples in the ranges of 4000 – 400 cm<sup>-1</sup>, 2000 – 400 cm<sup>-1</sup>, and 1400 – 400 cm<sup>-1</sup>. The deconvolution and fitting of the FT-IR bands of the 2GR sample into distinct peaks in the range of 1300 – 650 cm<sup>-1</sup>

was performed using the Peak analyzer procedure in an Origin software (OriginPro 9, Origin Lab Corporation, Northampton, MA, USA). For the FT-IR spectrum, the selected region was baseline-linearized before curve fitting. The Gaussian, Lorentzian, and Voigt functions were assessed and, ultimately, the Voigt line shape was chosen for the fitting.

The thermal decomposition of the samples was examined through thermogravimetric analysis and differential scanning calorimetry (TG-DSC) using a Perkin Elmer STA 6000 Simultaneous Thermal Analyzer (Pittsburgh, PA, USA). Approximately 10 mg of dried sample was heated from 25 °C to 900 °C at a controlled heating rate of 10 °C/min, all within a dry flowing air environment (20 mL/min).

The microstructure of the synthesized products was characterized using a scanning electron microscope SU-70 (Hitachi, Tokyo, Japan) and a scanning electron microscope equipped with an EDX detector (SEM Hitachi TM 3000, Tokyo, Japan). The samples underwent imaging, maintaining their original surfaces or fractured for internal observations. ImageJ analysis software (U.S., NIH) was employed for the quantitative evaluation of synthesized Mg-WH granule size on the base of SEM images. Measurement involved determining the longest chord-connecting points in the discernible granules.

The Brunauer–Emmet–Teller (BET) method was used to measure the  $S_{\text{BET}}$  of synthesised materials [225]. Prior to a measurement, the samples were degassed at 120 °C for 2 h. The Tristar II instrument from Norcross, GA, USA, was used for this purpose. Furthermore, the pore size distribution of the material produced was determined using the Barrett–Joyner–Halenda (BJH) method [226]. The  $S_{\text{BET}}$  and pore size distribution were calculated using the built-in software of the Tristar II apparatus. The total volume ( $V_p$ ) was estimated from the amount of  $N_2$  adsorbed at a relative pressure ( $p/p_0$ ) close to unity. The T-plot method was used to determine the micropore volume ( $V_\mu$ ) [227].

Antibacterial tests for pure Mg-WH specimen were conducted by preparing stock suspensions (2 g/L) in ultrapure water (Direct-Q, MilliQ, Merck, Germany) with a final volume of ~20 mL. The suspension was probe-sonicated for 2 min at 40 W (Branson Digital Sonifier®, USA) and stored at room temperature in the dark. For antibacterial testing, serial dilutions of the stock suspensions were prepared in ultrapure water. The stock suspension was probe-sonicated immediately before each experiment. Antibacterial effect tests were performed using the “spot test” as described in [228]. Briefly, *Escherichia coli* (*E. coli*) MG1655 and *Staphylococcus aureus* (*S. aureus*) RN4220, maintained at –80 °C, were streaked on Luria Bertani agar and cultivated at 30 °C for 24 h. Several colonies from the agar plate were

transferred into 3 mL of Luria Bertani medium and grown overnight (16–18 h) at 30 °C, 200 rpm. Overnight culture (400 µL) was used to inoculate 20 mL of fresh Luria Bertani medium in a 100-mL conical flask, incubated at 30°C, 200 rpm until mid-exponential growth phase (~1 h 50 minutes for *E. coli* and ~2 h for *S. aureus*, optical density at 600 nm, OD<sub>600</sub>, of bacterial cultures was ~0.6). The bacterial cultures were then harvested by centrifugation (5000xg, 7 minutes), washed with ultrapure water twice, and re-suspended in ultrapure water at ~10<sup>7</sup> colony forming units or CFU/mL (OD<sub>600</sub> 0.1). Bacterial exposures to chemicals were performed in 96-well microplates. For that, 100 µL of bacterial suspension in ultrapure water was added to 100 µL of chemical suspension in a microplate well. The sample was tested at 0.1, 1, 10, 100, and 1000 mg/L in two replicates. Bacteria in ultrapure water were used as a control for 100% viable bacteria and ZnSO<sub>4</sub>-exposed bacteria were used as a positive control for the antibacterial effect. The microplate was incubated at 30 °C for 2 h or 24 h before “spotting” 3 µL from each microplate well on Luria Bertani agar to evaluate bacterial growth. Bacterial growth on agar plates was assessed after 24 h of incubation at 30 °C. The minimum bactericidal concentration (MBC) of the tested sample was determined as the lowest tested concentration of the chemical that completely inhibited the formation of visible colonies.

### 3. RESULTS AND DISCUSSION

The first part of the study will focus on preparing large-scale Mg-WH powders from gypsum at different reaction durations. The second part of the study will be devoted to forming the Mg-WH granules from gypsum granules, evaluating the pH impact on the composition, morphology and surface properties of products. In the last part of the study a method for synthesising Mg-WH granules with tailored morphologies and phase compositions will be explored.

#### 3.1. Large-scale synthesis and characterization of Mg-WH powders: influence of reaction time

To investigate the time required for the formation of the Mg-WH phase, the reaction time was gradually extended from 24 h to 72 h, maintaining a constant synthesis temperature of 80 °C. The composition of the obtained samples was confirmed by analyzing the powder XRD patterns shown in Figure 15.

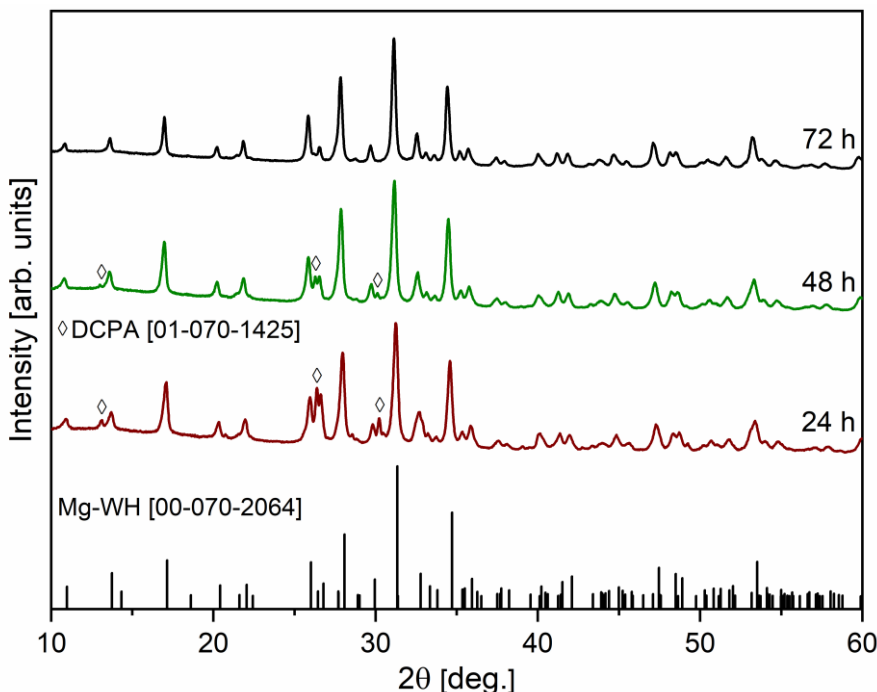


**Figure 15.** XRD patterns were measured for samples synthesized for various reaction durations, specifically 24 h, 48 h, and 72 h. The vertical lines below depict reflections from the standard XRD pattern of Mg-WH, according to ICDD #00-070-2064.

When examining the XRD patterns of the samples synthesized for durations of 24 h and 48 h, a mixture of DCPA (ICDD #01-070-1425) and the Mg-WH phase (ICDD #00-070-2064) were obtained. DCPA, due to its reactivity and solubility, is a valuable precursor material, allowing for the synthesis of various phases of CaP, including GYP, CPCs, and HAP [229,230]. DCPA is known to be the most stable CaP phase in solutions with a pH less than 5 [231]. However, it should be noted that DCPA stability is modulated in the presence of Mg<sup>2+</sup> ions [192]. The appearance of the Mg-WH formation under magnesium-rich and mildly acidic and magnesium-rich pH conditions confirms the critical influence exerted by Mg<sup>2+</sup> ions on the stability of DCPA [192]. This influence establishes the requisite conditions for the successful realization of the Mg-WH phase from GYP *via* the DCPA phase within the synthesis parameters implemented in our study. In particular, the amount of DCPA diminished over time from 24 h to 48 h with a simultaneous increase in the Mg-WH content (see Figure 15). To investigate the crystalline phases present in these samples and to precisely quantify their compositions, the RIR method was employed. The results obtained are summarized in Table 1.

**Table 1.** Phase compositions were determined for the samples synthesized using different synthesis times.

Synthesis time (h)	Phase composition (%)	
	DCPA	Mg-WH
24	35	65
48	22	78
72	-	100

It was revealed that the 24 h sample exhibited a composition of 35 wt.% DCPA and 65 wt.% Mg-WH, while the 48 h sample demonstrated a distinctive composition of 22 wt.% DCPA and 78 wt.% Mg-WH. Prolonging the reaction time to 72 h revealed the disappearance of the DCPA phase in the XRD patterns, while the peaks associated with Mg-WH prevailed. Importantly, the discernible absence of any peaks associated with other crystalline phases, including precursor phases or intermediate compounds, in the XRD pattern confirmed the high purity of the prepared sample. Therefore, using the described synthesis procedure, 3.00 g of a single-phase Mg-WH structure sample was obtained in a single batch. This observation underscores the efficacy of the described synthesis procedure, demonstrating its capability to yield a large quantity of single-phase Mg-WH.

XRD analysis of the 72 h synthesized sample through Le Bail fitting matched well the standard provided by the ICDD No.: 00-070-2064 and, in turn, aligned with the rhombohedral Mg-WH crystal structure with the R3c space group (#161) (see Figure 16) [232].

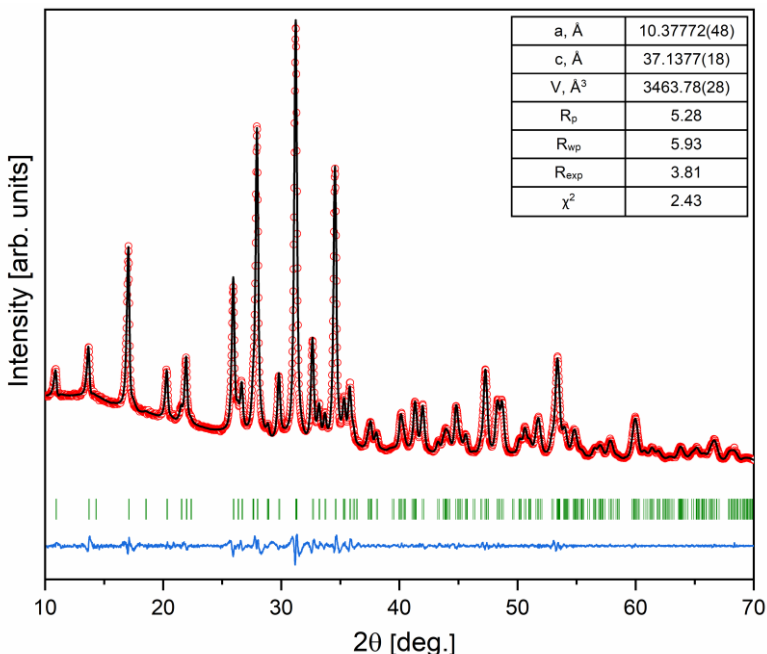


**Figure 16.** XRD pattern with the fitting curve through Le Bail refinement (red circles represent experimental points, and the solid line represents refined data; the blue line shows the difference between experimental and refined data; the  $2\theta$  positions marked in green are the allowed Bragg peaks) of 72 h synthesized Mg-WH.

Here, it should be noted that Mg-WH might be conceptualized as a material in which magnesium potentially substitutes calcium in the structure of synthetic  $\beta$ -Ca<sub>3</sub>(PO<sub>4</sub>)<sub>2</sub>. Despite the apparent similarity in the XRD patterns of these materials, a profound examination through advanced analytical techniques of their crystal structures revealed a substantial disparity [232,233].

The XRD data were further analyzed to determine the lattice parameters. The refined lattice parameters,  $a = 10.37772(48)$  Å and  $c = 37.13776(180)$  Å, are in good correlation with the values provided in the literature [35]. Furthermore, the observed XRD pattern of the Mg-WH sample aligns closely with the calculated one (see Figure 16).

It is important to note that the XRD pattern observed for the Mg-WH sample exhibited diffraction peaks of notable widths. Furthermore, it was determined that the synthesized Mg-WH powder was composed of crystallites with an average size of 34 nm. A comprehensive analysis was conducted to assess the crystallinity, considering the coexistence of the crystalline and amorphous phases in the XRD pattern. The evaluation revealed a degree of crystallinity of 78%. It is well known that the crystallinity of CaPs significantly influences the dissolution behavior of a material [234]. Typically, more crystalline regions exhibit slower dissolution rates than their amorphous counterparts, affecting the performance of the material in biological or environmental settings. This understanding is crucial for predicting the long-term stability and potential applications of synthesized materials.

FT-IR spectroscopy is a widely utilized analytical technique because of its capability to discern the presence of structural units within inorganic materials. FT-IR analysis was performed to confirm the structure of our 72 h synthesized Mg-WH sample (see Figure 17). The observed spectral characteristics are indicative of distinct vibrational modes associated with the  $\text{PO}_4^{3-}$  and  $\text{HPO}_4^{2-}$  groups. A set of vibrations at  $1171\text{ cm}^{-1}$ ,  $1134\text{ cm}^{-1}$ ,  $1064\text{ cm}^{-1}$ ,  $1013\text{ cm}^{-1}$ , and  $954\text{ cm}^{-1}$  were associated with the stretching vibrations of the P–O bonds, denoted as  $v_3$  and  $v_1$ , respectively [235]. A wide absorption band centered at  $861\text{ cm}^{-1}$  was observed, indicating the stretching of the P–O(H) bond intrinsic to the crystal structure of Mg-WH [235]. The bands observed at  $601\text{ cm}^{-1}$ ,  $542\text{ cm}^{-1}$ , and  $459\text{ cm}^{-1}$  were associated with the bending vibrations  $v_4$  of the P–O and  $v_2(\text{O–P–O})$  vibrations, respectively [236].

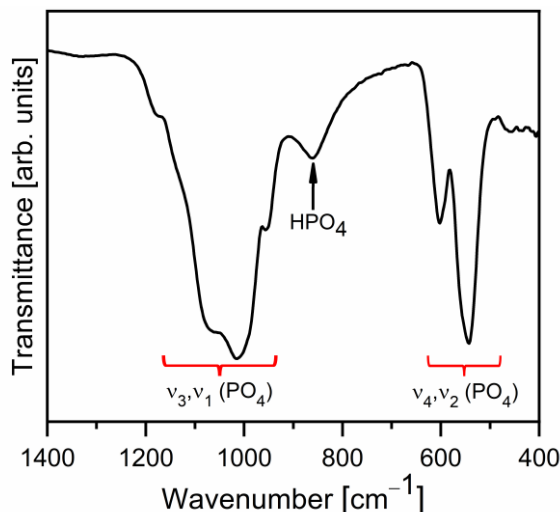


**Figure 17.** FT-IR spectrum of the 72 h synthesized Mg-WH.

The thermal decomposition behavior of the 72 h sample was investigated through simultaneous TG-DTG measurements. The TG-DTG curves of the analyzed sample are shown in Figure 18. In particular, Mg-WH was predicted to undergo dehydration and condensation of the  $\text{HPO}_4^{2-}$  group at around 600 °C, resulting in the formation of magnesium-substituted  $\beta$ -TCP ( $(\text{Ca},\text{Mg})_3(\text{PO}_4)_2$ ),  $\text{Ca}_2\text{P}_2\text{O}_7$  (calcium pyrophosphate), and water, according to the predicted chemical pathway elucidated in a previous study [210]. This process is associated with a theoretical weight loss of less than 1 wt.%. Notably, the synthesized Mg-WH was quite stable up to 500 °C. Upon gradual heating of the 72 h synthesized sample, a continuous weight loss was observed, reaching completion at approximately 750 °C, with a total mass loss of approximately 3 wt.%. The observed disparity in weight loss implies the existence of absorbed water in the as-prepared material, which is likely the result of the physically captured water on the sample surface during the synthesis process.

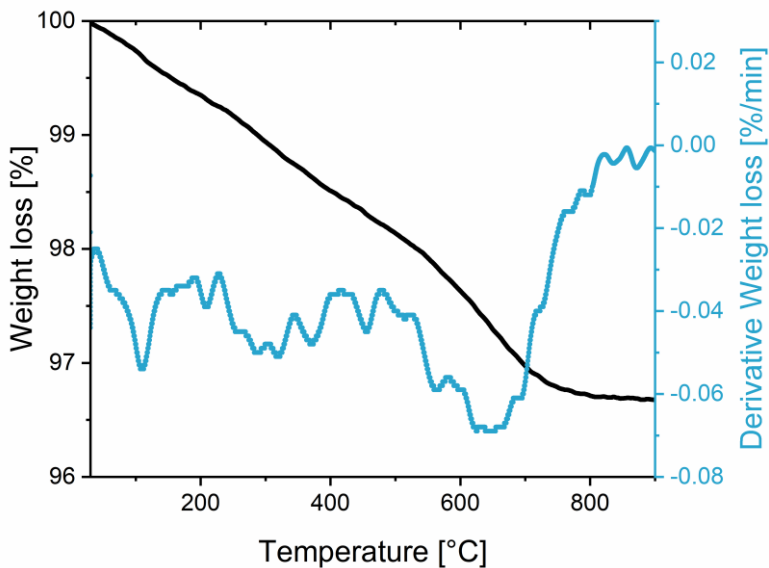


**Figure 18.** TG/DTG curves of the 72 h synthesized Mg-WH.

The microstructure and surface morphology of the 72 h synthesized Mg-WH were investigated through SEM. Figure 19a,b show the SEM images of the sample. It can be seen that the surface of the sample is composed of uniform, rhombohedrally shaped crystals, featuring pointed tops, sharp edges, and dimensions within the range of approximately 75 to 150 nm. In particular, the observed particle growth mechanism appears to align with Ostwald ripening rather than with continuous nucleation. The ripening of Ostwald

facilitates the dissolution of smaller particles upon synthesis, leading to the growth of larger rhombohedral crystals [178,237]. A small number of pores also formed during synthesis, as shown in Figure 19a. On closer examination at higher magnifications, as shown in Figure 19b, the flat surfaces of each particle were apparent, and no discernible impurities were observed. The well-defined rhombohedral shape is characteristic of WH crystals and agrees well with previously reported studies [34,193].

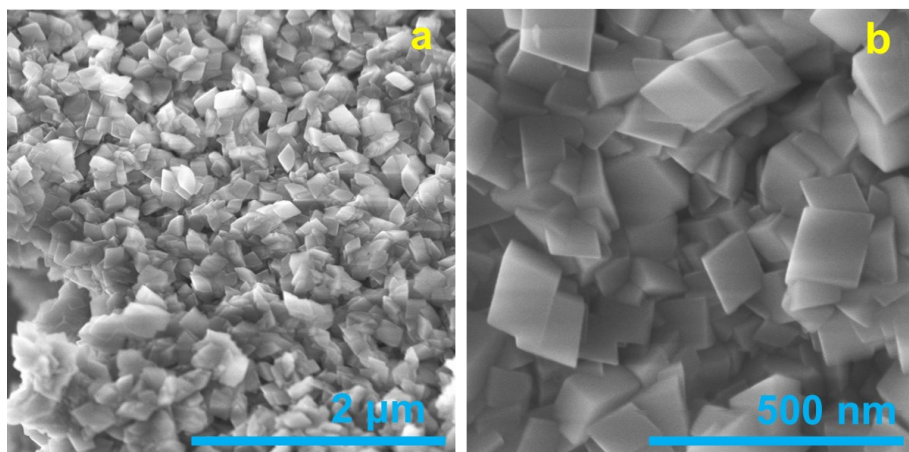


**Figure 19. (a,b)** SEM images of the 72 h synthesized Mg-WH.

The elemental composition of the 72 h synthesized sample was examined using EDX spectroscopy to validate the homogeneity of the elemental distribution within the fabricated sample [238]. The EDX of the elemental analysis results showed the presence of calcium (Ca), magnesium (Mg), phosphorus (P), and oxygen (O) in the Mg-WH sample (see Figure 20). The quantitative analysis yielded atomic concentrations of Ca:Mg:P:O as 21.44:1.53:15.61:61.42 in the Mg-WH sample, closely aligned with the atomic concentration values for stoichiometric Mg-WH, which are 20.00:2.22:15.55:62.22. According to Afonina et al., the inherent flexibility of the Mg-WH structure allows for variation in the calcium-to-magnesium ratio [206]. Consequently, our synthesized sample exhibited a slightly reduced magnesium content compared to that of the stoichiometric Mg-WH, reflecting the adaptability of the Mg-WH structure to accommodate subtle compositional variations. Notably, the absence of sulfur (S) in the EDX spectrum served as a distinctive indicator, confirming the absence of precursor GYP in the final sample. This absence underscores not only the purity of the Mg-WH phase, but also the effectiveness of the chosen synthesis route.

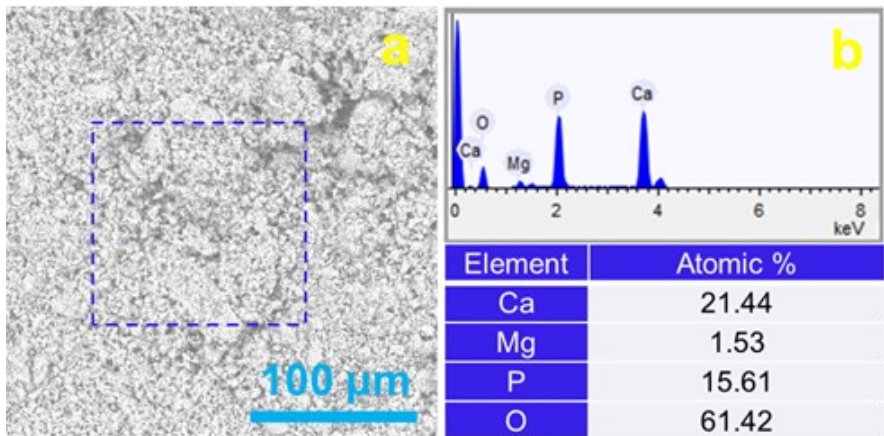


**Figure 20.** (a) Hitachi SEM image acquired with an SEM 3000 and (b) output of EDX spectra and atomic concentration of Ca, Mg, P, and O of the 72 h synthesized Mg-WH.

Elemental mappings of Ca, Mg, and P are illustrated in Figure 21a–d. The results obtained depicted a consistent and uniform distribution of elements throughout the entire sample. In particular, there were no observable indications of segregation or the formation of additional phases, signifying a high level of homogeneity in the elemental composition.

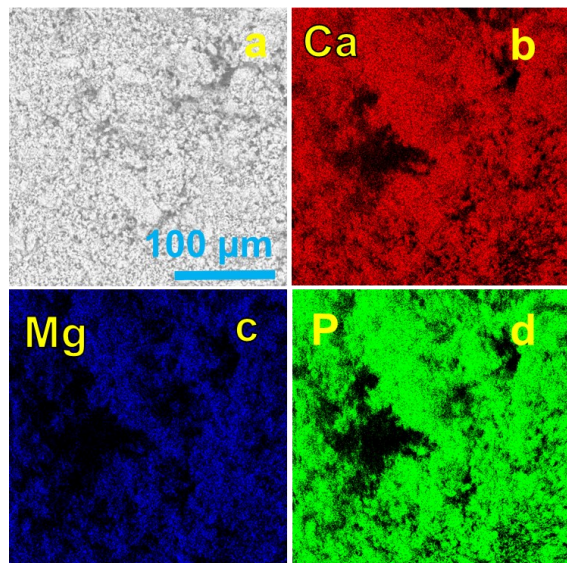


**Figure 21.** (a) SEM image acquired with a SEM Hitachi TM 3000 and corresponding elemental distribution EDX mapping of Ca (b), Mg (c), and P (d) of the 72 h synthesized Mg-WH.

Figure 22 shows the N<sub>2</sub> adsorption-desorption isotherm of the 72 h synthesized Mg-WH sample.

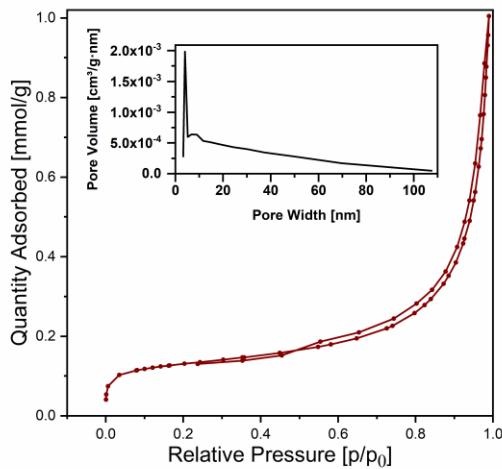


**Figure 22.** N<sub>2</sub> adsorption-desorption isotherms of 72 h synthesized Mg-WH sample. The inset shows the pore size distributions obtained through the BJH method.

In the very low relative pressure range, the adsorption curve demonstrates concavity relative to the  $p/p_0$  axis, transitioning into a semi-linear segment in the middle section and increasing rapidly at  $p/p_0 > 0.6$ . At a high relative pressure region of the isotherm, the adsorption curve exhibits convexity toward the  $p/p_0$  axis, with the amount of adsorbed N<sub>2</sub> capable of increasing without limits when  $p/p_0$  equals 1. In particular, adsorption did not reach saturation (even when reduced to a mere inflection point), which is due to the presence of macropores in the sample [239]. In the course of the analysis, the disparity between the N<sub>2</sub> adsorption and desorption curves becomes visible. This is particularly evident as a narrow gap between the adsorption and desorption branches, accompanied by a discernible hysteresis loop upon reduction of pressure [239]. The curves illustrated in Figure 22 show mixed types of II and IV isotherms characterized by a distinctive H3 hysteresis loop [239,240]. Typically, non-porous and macroporous adsorbents (i.e., materials in which the pores are greater than 50 nm) show type II isotherms, while type IV irreversible isotherms are specified by mesoporous adsorbents (i.e., materials with pores of widths between 2 nm and 50 nm) [239]. Loops of the H3 type are formed by non-rigid aggregates of platy particles that give rise to slit-shaped pores that arise from the stacking of crystal particles [239]. The pore size distribution curve (see inset in Figure 22) reveals a relatively narrow

distribution of pore sizes, with a predominant peak reaching  $\sim$ 4 nm, corresponding to the mesopores [240]. The  $S_{\text{BET}}$  calculated using the BET equation was  $10 \text{ m}^2/\text{g}$  for the 72 h synthesized Mg-WH sample.

### 3.2. Large-Scale synthesis and characterization of Mg-WH granules: the effect of reaction pH on phase composition

To investigate the optimal pH conditions necessary for the precipitation of the Mg-WH phase for the selected synthesis method, various volume combinations of 1 M  $\text{NaH}_2\text{PO}_4$  and 1 M  $\text{Na}_2\text{HPO}_4$  solutions were tested. During the synthesis, the GYP granules were mixed with a magnesium-containing solution and subsequently combined with a mixture of varying volumes of  $\text{Na}_2\text{HPO}_4$  and  $\text{NaH}_2\text{PO}_4$  solutions, resulting in pH values of 5.7 (1GR), 6.2 (2GR), and 6.7 (3GR). Throughout these experiments, a consistent synthesis time (5 days) and a temperature of 80 °C were rigorously maintained. Figure 23 shows the XRD patterns of the samples synthesized by the dissolution-precipitation reactions at varying pH levels.

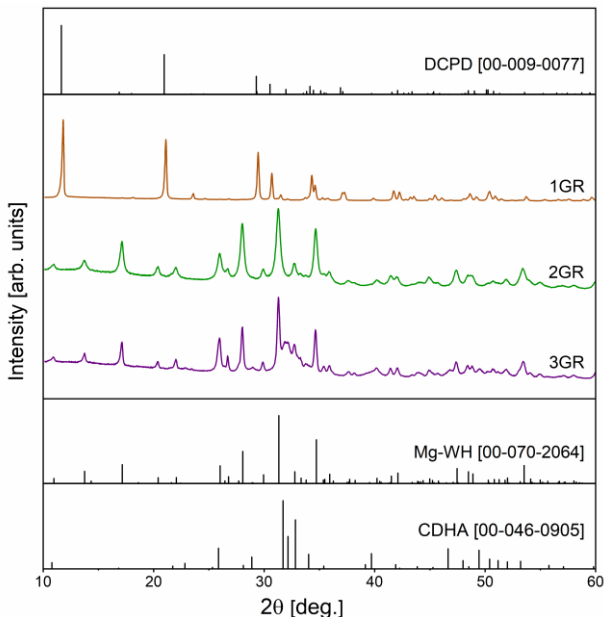


**Figure 23.** XRD patterns of 1GR, 2GR, and 3GR samples synthesized at different pH. The obtained diffraction peaks were identified by standard references for the DCPD, Mg-WH, and CDHA phases.

The pH level during the synthesis process exerts a significant influence on the dissolution-precipitation mechanisms that govern the formation of particular CaP

phases. This influence is achieved by affecting the solubility of precursors and the availability of ions, thereby regulating the processes of nucleation and growth pathways. The 1GR sample synthesized at pH=5.7 consisted of the DCPD (ICDD #00-009-0077) phase, also known as the brushite mineral. DCPD is characterized as a metastable phase, which typically emerges as the predominant crystalline entity when CaPs precipitate in moderately acidic conditions [241]. As many researchers have previously reported, the inclusion of magnesium ions in the reaction solution could impede DCPD transformation into thermodynamically stable CaP phases, such as DCPA, OCP, CDHA, and HAP, even under conditions of elevated pH [215,241]. A.C. Tas showed that the formation of Mg-doped calcium phosphate on the surfaces of DCPD crystals is likely to reduce the solubility of these crystals, thus inhibiting conversion to other phases of CaP phases [215].

A thorough analysis of the XRD pattern of 2GR sample was conducted, revealing that the product synthesized at pH=6.2 corresponds to a rhombohedral Mg-WH phase (ICDD #00-070-2064) with a space group of R3c (#161) [178]. No XRD peaks associated with reactants or other crystalline phases were discerned, indicating the single-phase nature of the 2GR sample. As illustrated in Figure 24, the XRD pattern of the 2GR sample is presented, along with the fit curve obtained from Le Bail refinement, a well-established method for determining lattice parameters, especially for low-crystallinity samples or poorly resolved peaks.

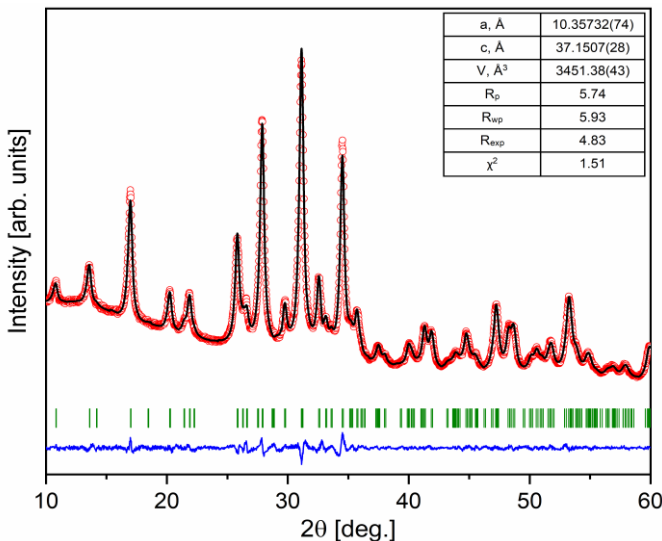


**Figure 24.** XRD pattern with the fitting curve by Le Bail refinement of the synthesized 2GR sample. Red circles represent experimental points and the solid line represents refined data, the blue line shows the difference between experimental and refined data of the synthesized 2GR sample, and the green marks in  $2\theta$  positions are the allowed Bragg peaks.

The refined cell parameters were  $a = b = 10.357(74)$  Å,  $c = 37.15(275)$  Å,  $\alpha = \beta = 90^\circ$ , and  $\gamma = 120^\circ$ . The volume of the unit cell was  $3451.15(433)$  Å<sup>3</sup>. The 2GR granules were synthesized in a solution containing sodium salts, which could potentially lead to sodium adsorption or intercalation into the structure. To minimize possible sodium adsorption, the synthesized products were thoroughly washed with hot water. The refined lattice parameters were consistent with those reported in the literature for Mg-WH, and no systematic XRD peak shifts were observed, suggesting that sodium intercalation did not occur [35,242]. Determining structural parameters is key to identifying crystalline phases. Comparing these with reference data confirms the crystallographic phase, while monitoring lattice parameters during synthesis ensures uniformity, quality control, and reproducibility.

As demonstrated by the XRD pattern acquired for the 2GR sample, the presence of broad diffraction peaks is indicative of a certain degree of structural disorder and/or small crystallite size within the material. On further examination, it was determined that the synthesised Mg-WH powder consisted of crystallites with an average size of 16 nm. A thorough analysis was conducted to assess the crystallinity comprehensively, considering the coexistence of crystalline and amorphous phases in the XRD pattern. This evaluation revealed a degree of crystallinity of 60%. Crystallinity of CaPs significantly affects their dissolution behaviour, with more crystalline regions typically exhibiting slower dissolution rates compared to their amorphous counterpart [234]. The low crystallinity of the 2GR sample presents a significant challenge in the acquisition of high-resolution structural data, particularly in accurately determining both the position and quantity of magnesium within the Mg-WH structure.

The discernible presence of the rhombohedral Mg-WH was also confirmed in the 3GR sample, synthesized at a pH of 6.7 [23]. In addition to the diffraction peaks corresponding to the Mg-WH phase, the 3GR sample showed diffraction peaks corresponding to the crystalline CDHA (ICDD #00-046-0905). As the pH approaches neutrality, the stabilizing effect of Mg<sup>2+</sup> ions diminishes, creating conditions more favorable for the crystallization of apatite, which is thermodynamically stable at neutral pH. This transition underscores the pivotal role of pH in modulating the formation of discrete CaP phases, with Mg<sup>2+</sup> ions exerting a stabilizing influence on the Mg-WH phase at lower pH levels, while higher pH values promote the crystallization of more thermodynamically stable CaPs. To determine the phase composition of the 3GR sample, Rietveld refinement was used (see Figure 25). The refinement results were in agreement with the measured diffraction profiles, affirming the presence of only the Mg-WH and CDHA phases within the sample. The

refinement revealed that the 3GR sample possesses 37 wt.% of Mg-WH and 63 wt.% of CDHA. In aqueous solutions, undoped CaPs subjected to pH conditions that exceed 4.5 are recognized to undergo a gradual transformation into CDHA [243]. The possibility of the formation of biphasic material should be considered as an advantage of the suggested synthetic approach, since BCPs are also widely used in medicine. The co-existence of 2 phases allows for the adjustment of some physical properties of the materials, such as resorption rate. The most popular BCPs are the composites of HAP and  $\beta$ -TCP, which is closely related to Mg-WH.

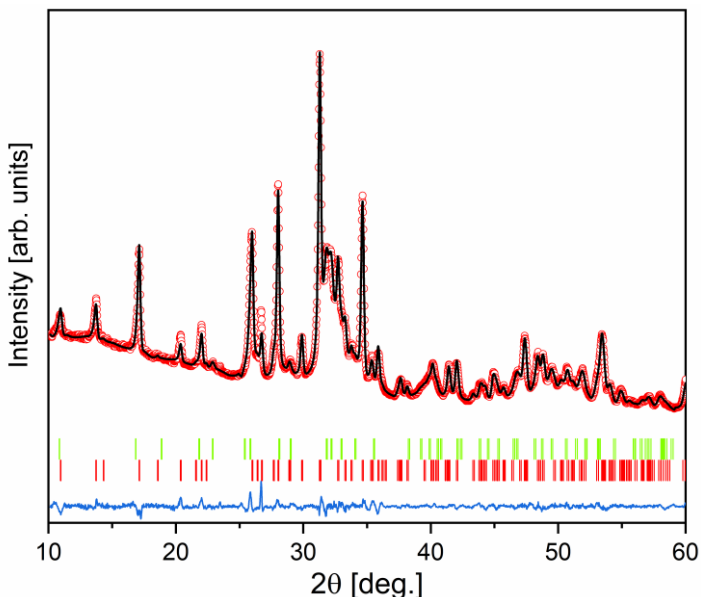


**Figure 25.** The Rietveld refinement plot of the 3GR sample. Vertical red bars represent the peak positions of the Mg-WH phase (ICDD #00-070-2064), while light green ones represent the peak positions of the CDHA phase (ICDD #00-046-0905).

FT-IR spectroscopy was conducted as a supplementary method to XRD to study functional groups. The FT-IR spectrum of the synthesized 2GR sample is shown in Figure 26, while the spectra of 1GR and 3GR are depicted in Figure 27. The crystal structure of Mg-WH contains the phosphate ion ( $\text{PO}_4^{3-}$ ), which exhibits four IR-active vibrational modes:  $\nu_1$ ,  $\nu_2$ ,  $\nu_3$ , and  $\nu_4$ . The bands observed at low wavenumbers  $603\text{ cm}^{-1}$ ,  $544\text{ cm}^{-1}$ , and  $464\text{ cm}^{-1}$ , correspond well to the  $\nu_4(\text{PO}_4^{3-})$  and  $\nu_2(\text{PO}_4^{3-})$  bending modes [232]. The band at  $1187\text{ cm}^{-1}$  corresponds to the bending mode of the P–O(H) bond, while the broad peak at  $869\text{ cm}^{-1}$  is attributed to the P–O(H) stretching vibration within

the Mg-WH structure [24,232,244]. In the spectra examined, it is noteworthy that the discernible band intrinsic to the crystal structure of Mg-WH, centered at  $920\text{ cm}^{-1}$ , which corresponds to the P–O(H) stretching mode of the  $\text{HPO}_4^{2-}$  groups, is notably absent [24,219]. This absence might be attributable to the substantial overlap observed in the region, which is a consequence of the limited atomic arrangement exhibited by the 2GR sample.

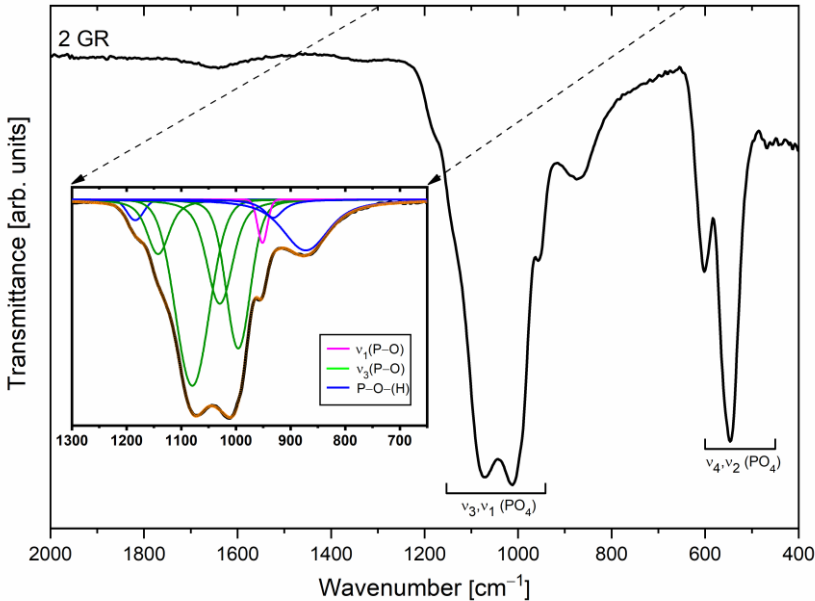


**Figure 26.** FT-IR spectrum of the 2GR sample. Insertion: experimental data are depicted alongside deconvoluted and fitted curves in the  $1300 – 650\text{ cm}^{-1}$  range.

To extract individual components of the overlapped bands from the experimental FT-IR spectrum, we performed a deconvolution analysis within the spectral range of  $1300 – 650\text{ cm}^{-1}$ . To obtain a reconstituted curve as close as possible to the original spectra, we derived eight sub-bands within the examined spectral range. Through this process, a previously indiscernible narrow band centered approximately at  $931\text{ cm}^{-1}$  emerged as distinguishable within the deconvoluted spectrum. The observed deviation at the peak position can be attributed to a disorder of the crystal structure, resulting from various factors, including alterations in the bonding environment or the introduction of defects within the material [232].

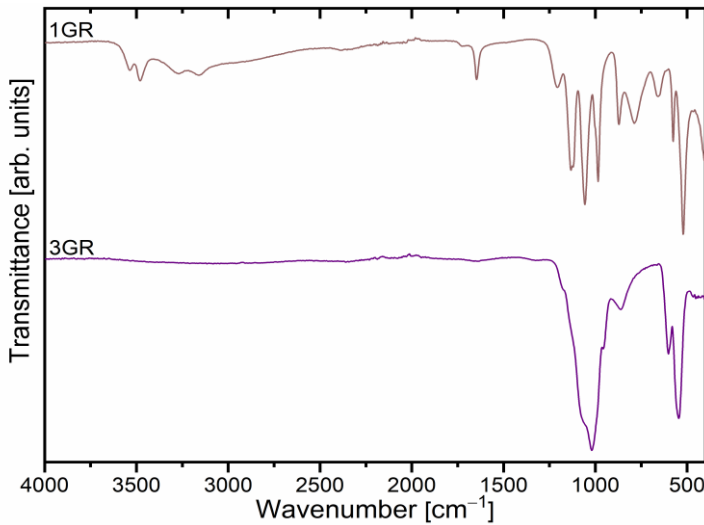


**Figure 27.** The FT-IR spectra of the 1GR and 3GR samples.

A spectral examination of the 1GR sample reveals the presence of  $\text{PO}_4^{3-}$  and  $\text{HPO}_4^{2-}$  groups (see Figure 27). Furthermore, the distinctive band observed at  $1646\text{ cm}^{-1}$  corresponds to the bending mode of structural water molecules found within the DCPD structure, further affirming the composition of the 1GR sample elucidated through XRD analysis [245]. The results from FT-IR analysis of the single-phase Mg-WH (2GR) sample and the 3GR sample, comprising both the Mg-WH and CDHA phases, reveal some alterations. In particular, an increase in the intensity of the  $1071\text{ cm}^{-1}$  band, associated with the Mg-WH phase, is evident in the 3GR sample. Furthermore, the peak corresponding to the P–O asymmetric stretching, located at  $1011\text{ cm}^{-1}$  for the 2GR sample, undergoes a notable shift toward higher wavenumbers, specifically at  $1019\text{ cm}^{-1}$ , indicative of the presence of the CDHA phase within the 3GR sample.

The morphology of GYP and the synthesized 2GR granules was thoroughly investigated using SEM (the results are presented in Figure 28). Following the mixing of CSH powder with water, hydration ensued, resulting in the formation of a solid GYP block through the interlocking of its crystals. The block was then subjected to crushing and sieving to yield the targeted granules. The SEM images of the resulting GYP granules reveal a clustered arrangement of particles on their surface, which is attributed to the crystallization and interlocking of GYP during the hydration process (see Figure 28a). Furthermore, the surface also exhibits microporosity, with tiny pores or voids distributed throughout the material. In Figure 28b, the morphology of 2GR granules is supported by a corresponding granule size distribution histogram, providing a quantitative representation of the sizes of

the Mg-WH granules. It is important to note that the particles observed at low magnification are not randomly formed clusters, but well-structured granules resulting from the selected synthesis process. The SEM images clearly show that granules, rather than a fine powder, of specific sizes have been successfully synthesized. The irregularly shaped granules of the 2GR sample show a wide size distribution ( $210 - 450 \mu\text{m}$ ), with an average size of approximately  $329 \mu\text{m}$  (measured for more than 100 granules). Regarding the surface of the granules, it is composed of interlocked rod-like particles (as seen in Figures 28c and 28d), which consist of fine crystals. The higher magnification SEM micrograph (see Figure 28e) elucidates that the 2GR granules are comprised of a stack of rhombohedral particles, exhibiting a homogeneous size distribution. As aforementioned, the rhombohedral shape is characteristic of Mg-WH crystals and is in good agreement with previously reported studies [34]. The micrograph also elucidates that the sample comprises small particles with an average size of approximately  $70 \text{ nm}$ . Furthermore, for a detailed SEM examination of the internal structure of the granule, the 2GR sample was intentionally fractured (see Figure 28f). On closer examination, the SEM image reveals the presence of rhombohedral monodisperse particles of approximately  $90 \text{ nm}$ , consistent with those observed on the exterior surfaces of the granules.

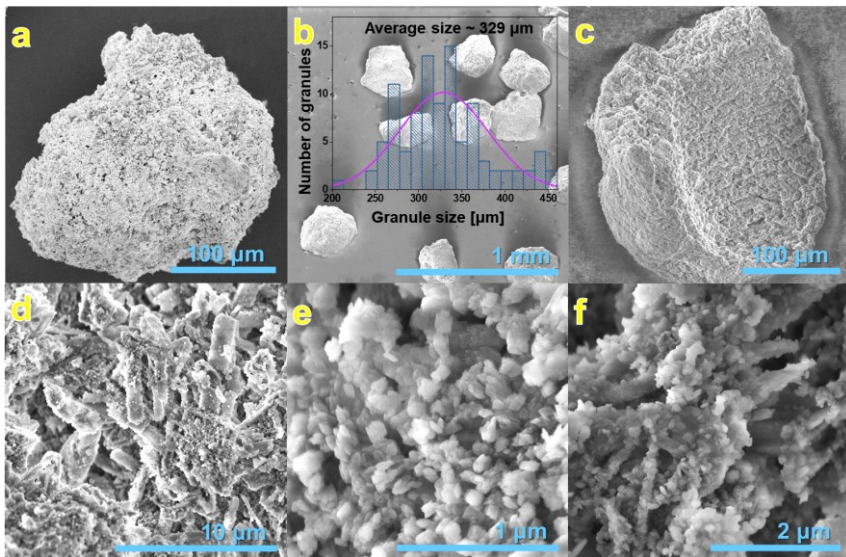


**Figure 28.** SEM images of GYP and the 2GR granules: (a) a micrograph of GYP granule; (b) a micrograph accompanied by the corresponding 2GR granule length distribution histogram; (c), (d), (e) micrographs of the 2GR sample captured at different magnifications, while (f) micrograph of a cross-section of 2GR granule.

This observation suggests a uniform distribution of the crystalline structure throughout the granules, indicating a successful synthesis process. As the dissolution-precipitation reaction progresses from the surface to the interior of the granule, precipitation kinetics favor faster nucleation and growth rates at the surface, forming numerous small grains [246]. This occurrence arises because of the higher availability of reactants on the surface of the precursor granule. Concurrently, within the bulk of the granule, the reaction progresses at a slower rate, facilitating the dissolution of smaller Mg-WH particles and the selective growth of larger crystals. This is evidenced by SEM images, which reveal an increase in the size of interior Mg-WH crystals. This phenomenon can be attributed to Ostwald ripening, a process observed in certain systems where small particles dissolve while larger ones grow over time [247]. This dynamic interplay between dissolution and precipitation processes contributes to the nuanced evolution of the crystal size distribution within the granule.

Morphological analysis of the 1GR and 3GR granules by SEM revealed distinct characteristics (see Figure 29).

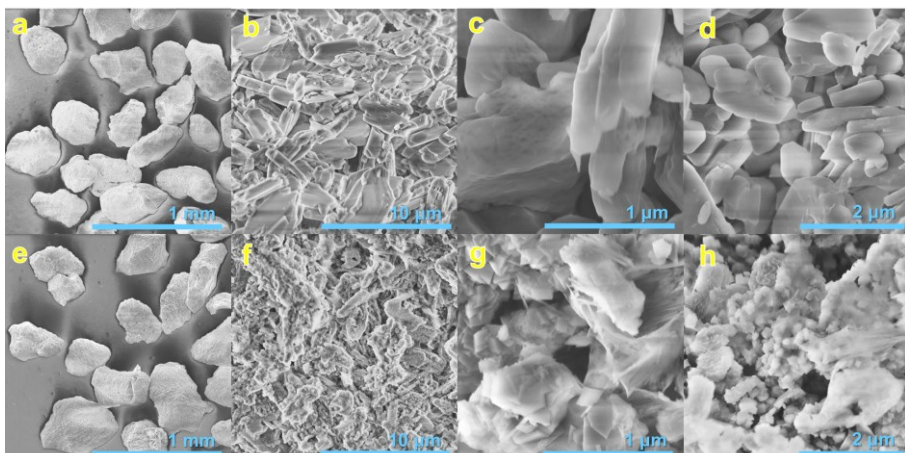


**Figure 29.** SEM images of 1GR and 3GR granules are presented: (a), (b) and (c) depict micrographs of the 1 GR sample captured at different magnifications; (d) displays an image of a fractured 1GR granule; (e), (f) and (g) depict micrographs of the 3GR sample captured at varying magnifications; (h) displays an image of a fractured 3GR granule.

The synthesized 1GR granules exhibited smooth volumetric crystals with irregular shapes. On the contrary, the 3GR sample displayed rhombohedral Mg-WH crystals varying in size from approximately 100 to 250 nm along with

cloud-like agglomerates, which can be attributed to the CDHA phase [194]. The co-existence of particles of different morphology correlates very well with the biphasic composition of 3GR, as revealed by XRD analysis.

$N_2$  adsorption-desorption measurements were performed to assess the surface properties of the synthesized 1GR – 3GR samples (see Figure 30 for the 2GR sample).

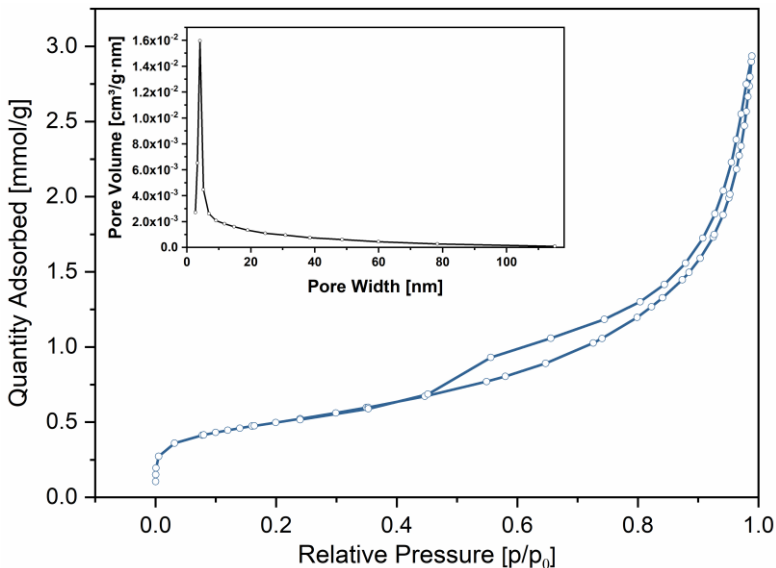


**Figure 30.**  $N_2$  adsorption-desorption isotherm of the 2GR sample. The inset shows the pore size distributions obtained by the BJH method based on the desorption branch of the isotherm.

In the low relative pressure regime, the adsorption isotherm exhibits concavity relative to the  $p/p_0$  axis, indicative of micropore filling, which transitions into a moderate adsorption process. At higher relative pressures, the isotherm exhibits a convex curve toward the  $p/p_0$  axis, followed by a rapid increase in  $N_2$  adsorption as  $p/p_0$  approaches unity, lacking a distinct inflection point, as discussed in the previous section, mainly due to the presence of macropores in the sample pore structure [239]. In particular, during the analysis, a distinct disparity becomes apparent between the  $N_2$  adsorption and desorption curves, evidenced by a narrow gap between the branches upon pressure reduction, suggesting that mesopores were present in the samples [239]. All of these observations strongly suggest the presence of a diverse range of pore sizes within the analyzed sample, with a certain number of micropores and macropores along with mesopores, which appear to be particularly prominent. The  $N_2$  adsorption-desorption curve illustrated in

Figure 30 exhibits characteristics of both type II and type IV isotherms, with a distinctive H3 hysteresis loop. Type II isotherms are typical of nonporous or macroporous materials, while type IV isotherms indicate mesoporous structures. The H3 loop is indicative of pores that are slit, probably resulting from the assembly of Mg-WH particles or a macropore network [248]. The inset of Figure 30 shows the pore size distribution in the 2GR sample, calculated from the desorption branch using the BJH method. The analysis of the pore size distribution revealed a relatively wide range of pore sizes, with a prominent peak observed around 4.1 nm, providing additional confirmation of the predominantly mesoporous nature of the material (as defined by the International Union of Pure and Applied Chemistry, IUPAC [247]).

Information on  $S_{\text{BET}}$ ,  $V_{\mu}$  (micropore volume), and  $V_p$  (total pore volume) of the 1GR – 3GR samples is given in Table 2. It is noteworthy that the 2GR granule, comprising the Mg-WH phase, exhibits a significantly larger  $S_{\text{BET}}$  compared to the powdered form [201]. This increased  $S_{\text{BET}}$  confers several advantages, including increased reactivity and enhanced interaction with surrounding biological tissues, which can lead to improved integration and healing outcomes [249]. Sample 2GR exhibits the highest  $V_{\mu}$  and  $V_p$  values among the materials analysed. However, the contribution of micropores to the overall porosity of this sample is minimal. These results indicate that the 2GR sample has a porous structure, primarily mesoporous in nature, as supported by the BJH pore size distribution analysis.

**Table 2.** Data derived from  $N_2$  adsorption-desorption measurements:  $S_{\text{BET}}$ ,  $V_{\mu}$ , and  $V_p$  of the 1GR – 3GR samples.

Sample	1GR	2GR	3GR
$S_{\text{BET}}$ ( $\text{m}^2/\text{g}$ )	3	40	25
$V_{\mu}$ ( $\text{cm}^3/\text{g}$ )	0.0017	0.0026	0.0019
$V_p$ ( $\text{cm}^3/\text{g}$ )	< than 0.010	0.095	0.073

To the best of our knowledge, the antibacterial properties of Mg-WH have not been previously studied. In order to investigate this aspect, we conducted measurements to assess the antibacterial efficacy of Mg-WH. The 2GR sample was not bactericidal for two common bacterial species: *E. coli* (gram-negative bacterium) or *S. aureus* (gram-positive bacterium). Both bacteria were viable and grew on Luria Bertani agar after exposure to chemical suspensions even at 1000 mg/L. No antibacterial effects appeared after 2-h or 24-h exposure to chemicals.

### 3.3. Synthesis of Mg-WH granules with different morphology through variations in precursor compositions

The XRD patterns of synthesised R1–R3, PR1/24h–PR3/24h, and PR1/48h–PR3/48h granules are presented in Figure 31(a-c). The results reveal that the synthesis of the R1–R3 granules predominantly led to the formation of GYP as the major crystalline phase. This observation indicates that the CASU powder utilized as a precursor underwent a hydration reaction during synthesis in an aqueous environment, resulting in its transformation into the dihydrate form of calcium sulfate. This hydration-induced phase transformation facilitated the transition from a loose powder to a consolidated solid through crystal growth and interlocking, which was subsequently processed into granules [250].

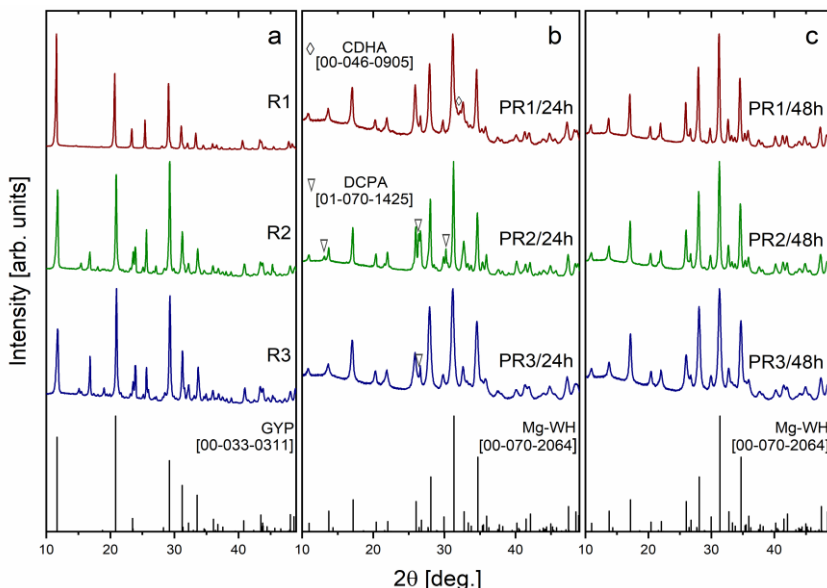


**Figure 31.** XRD patterns of R1–R3 (a), PR1/24h–PR3/24h (b), and PR1/48h–PR3/48h (c) granules synthesised *via* a dissolution-precipitation reaction. The obtained diffraction peaks were identified by standard references for the GYP, CDHA, DCPA, and Mg-WH phases.

The XRD patterns of the reaction products, obtained after the R1–R3 precursor granules were immersed in a solution containing  $Mg^{2+}$ ,  $H_2PO_4^{2-}$ ,  $HPO_4^{2-}$ , and  $PO_4^{3-}$  ions for a period of 24 h, are shown in Figure 31b. These include PR1/24h, PR2/24h, and PR3/24h, which are derived from the monophasic R1 granules and the mixed R2 and R3 granules, respectively, along with the standard Mg-WH diffractogram. The XRD patterns of

PR1/24h, PR2/24h, and PR3/24h granules revealed the formation of biphasic materials, with PR1/24h consisting of Mg-WH and CDHA phases, while PR2/24h and PR3/24h were composed of Mg-WH and DCPA phases. Notably, the amount of DCPA in the PR2/24h sample was significantly higher compared to PR3/24h. The formation of the CDHA phase is commonly observed at higher pH values, as Mg-WH is thermodynamically more stable than apatite under moderately low pH conditions. In this study, however, all syntheses were performed under nearly identical pH conditions, suggesting that the appearance of CDHA is influenced by variations in the Ca/Mg ratio within the reaction solution, as previously reported in [251]. The presence of the DCPA phase in the PR2/24h and PR3/24h samples can be ascribed to its function as a transient intermediate in the formation pathway of Mg-WH. It is known that DCPA undergoes a gradual conversion into Mg-WH over time, a transformation that is promoted by magnesium-rich conditions and moderately acidic pH. This observation is consistent with previous findings and underscores the pivotal role of reaction time, precursor composition, and solution composition on the resulting phase [201]. In contrast, the XRD patterns of the products synthesised for 48 h (PR1/48h, PR2/48h, and PR3/48h granules) demonstrated the formation of single-phase materials, as no diffraction peaks corresponding to CDHA, DCPA, or any other secondary phases were observed (see Figure 31c). The broad and low-intensity diffraction peaks indicate the formation of nanocrystallites with moderate crystallinity [252]. The reflection positions identified in the XRD analysis were subjected to careful indexing and were found to correspond with the standard diffractogram for rhombohedral Mg-WH [00-070-2064]. The diffraction peaks observed at  $2\theta$  values of  $10.92^\circ$ ,  $13.72^\circ$ ,  $17.14^\circ$ ,  $28.02^\circ$ ,  $31.28^\circ$ , and  $34.70^\circ$  can be attributed to the  $(0\ 1\ 2)$ ,  $(1\ 0\ 4)$ ,  $(1\ 1\ 0)$ ,  $(2\ 1\ 4)$ ,  $(0\ 2\ 10)$ , and  $(2\ 2\ 0)$  crystallographic planes of the Mg-WH phase, respectively. Additionally, smaller peaks align with the reference data. A 48 h synthesis duration was sufficient for the complete phase transformation of the raw granules into Mg-WH. The resulting products exhibited consistent composition, irrespective of whether the starting granules contained magnesium salts or were synthesised using magnesium-containing or magnesium-free solutions.

In order to ascertain the structural parameters of the synthesised single-phase PR1/48h–PR3/48h samples, a Le Bail refinement of the XRD data was conducted. The XRD patterns, together with the fitting curves derived from the Le Bail refinement, are displayed in Figure 32. The Le Bail refinement plots demonstrate an excellent correlation between the observed XRD patterns (red circles) and the calculated patterns (black line), which correspond to the

Bragg reflections (green ticks). This confirms the successful formation of the Mg-WH phase with a rhombohedral structure and space group R3c. The structural parameters of the Mg-WH phase synthesized from various starting compositions of raw granules during the 48 h synthesis process are presented in Table 3. The resulting products exhibited consistent structural characteristics, both within the set of samples and when compared to previously published data [242].

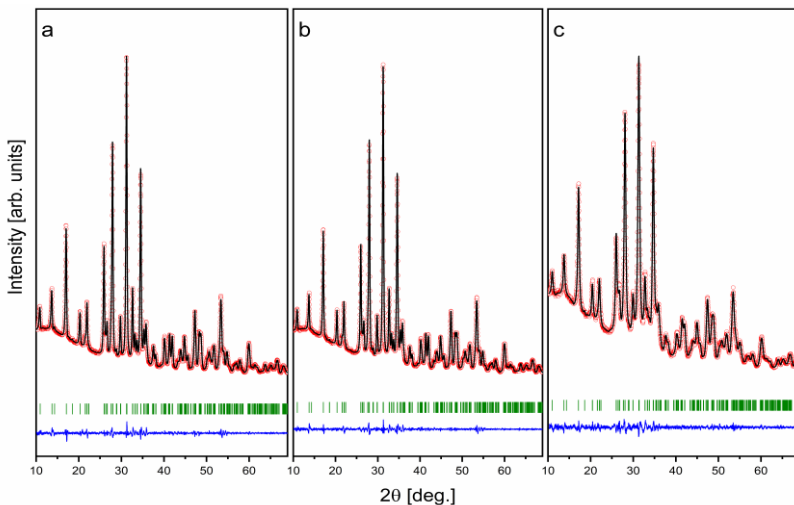


**Figure 32.** XRD patterns with the fitting curve by Le Bail refinement of the synthesized PR1/48h (a), PR2/48h (b), and PR3/48h (c) granules. The red circles represent the experimental data points, while the solid black lines correspond to the refined data. The blue lines indicate the discrepancy between the experimental and refined data for the synthesised samples, while the green markers at the  $2\theta$  positions represent the allowed Bragg peaks.

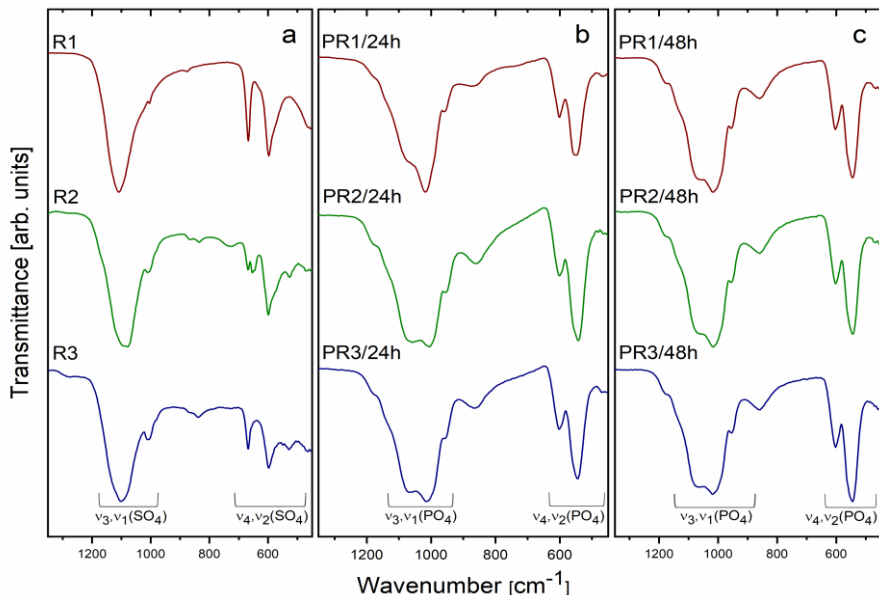
**Table 3.** Structural, R-values,  $\chi^2$ , and microstructural data elucidated from XRD for PR1/48h, PR2/48h, and PR3/48h samples.

Sample	PR1/48h	PR2/48h	PR3/48h
$a$ , Å	10.38042(44)	10.36717(46)	10.33965(92)
$c$ , Å	37.1445(17)	37.1087(17)	37.1038(35)
Cell volume, Å <sup>3</sup>	3466.21(26)	3454.04(27)	3435.27(54)
$R_p$	2.01	1.82	1.72
$R_{wp}$	2.68	2.38	2.19
$\chi^2$	1.74	1.39	1.19
Crystallite size, nm	46	52	17

The granules synthesised by a dissolution-precipitation reaction were subjected to analysis by FT-IR spectroscopy. Figure 33(a-c) illustrates the FT-IR spectra of the materials obtained under varying conditions. The FT-IR spectra of the R1–R3 raw granules display absorption bands centred at  $1110\text{ cm}^{-1}$ ,  $669\text{ cm}^{-1}$  and  $598\text{ cm}^{-1}$ , which are attributed to the stretching and bending modes of the sulfate ( $\text{SO}_4^{2-}$ ) ion (see Figure 33a) [253]. A weak absorption band centered at  $869\text{ cm}^{-1}$  is attributed to the stretching vibration of hydrogen phosphate ( $\text{P}-\text{O}(\text{H})$ ) groups, originating from the precursor salts  $(\text{NH}_4)_2\text{HPO}_4$  and  $\text{MgHPO}_4 \cdot 3\text{H}_2\text{O}$ .

The FT-IR spectra of the granules PR1/24h-PR3/24h display the presence of absorption bands corresponding to  $\text{PO}_4^{3-}$  and  $\text{HPO}_4^{2-}$  functional groups (see Figure 33b). The absence of  $\text{SO}_4^{2-}$ -related absorption bands suggests that the sulphate-containing precursors were completely dissolved and subsequently transformed into CaP materials during the 24 h synthesis process. These findings are corroborated by the XRD analysis, which identified specific CaP phases: the PR1/24h sample exhibited the presence of CDHA and Mg-WH, the PR2/24h and PR3/24h samples displayed the presence of DCPA and Mg-WH phases (see Figure 31b). The observed absorption bands at  $1180\text{ cm}^{-1}$ ,  $1065\text{ cm}^{-1}$ ,  $1011\text{ cm}^{-1}$  and  $954\text{ cm}^{-1}$  are attributed to the P–O and P–O(H) stretching vibrations associated with the  $\text{PO}_4^{3-}$  and  $\text{HPO}_4^{2-}$  groups, which are integral to the crystal structures of the CDHA, DCPA and Mg-WH phases, are present to different extents in the synthesised granules. The differences in the intensity of the absorption band at  $1065\text{ cm}^{-1}$  between the PR1/24h and PR2/24h samples provide further insight into the phase composition. In the case of PR1/24h, which comprises CDHA in conjunction with the Mg-WH phase, the increased intensity of the  $1065\text{ cm}^{-1}$  band can be attributed to the absence of a notable contribution from CDHA, given that this phase does not exhibit a pronounced absorption at this wavenumber [254]. In contrast, the  $1065\text{ cm}^{-1}$  band is prominent in the PR2/24h sample and barely noticeable in the PR3/24h sample, where it corresponds to the P–O stretching vibration characteristic of the DCPA phase, resulting in a smaller intensity for this absorption band [255]. Furthermore, the PR1/24h and PR2/24h samples display a relatively broad absorption band with a maximum at  $863\text{ cm}^{-1}$ , which is attributed to the stretching vibration of the P–O(H) bond. The broadness of this band indicates the coexistence of two distinct crystallographic environments for hydrogen phosphate ions, which are likely the result of the presence of two different calcium phosphate phases in the samples. At lower wavenumbers, the absorption bands at  $601\text{ cm}^{-1}$ ,  $545\text{ cm}^{-1}$ , and  $465\text{ cm}^{-1}$  are primarily associated with the Mg-WH phase and correspond to the bending modes of P–O and O–P–O bonds [35]. In the case of the PR1/24h sample, the peak at  $545\text{ cm}^{-1}$  displays a slight degree of broadening due to the presence of

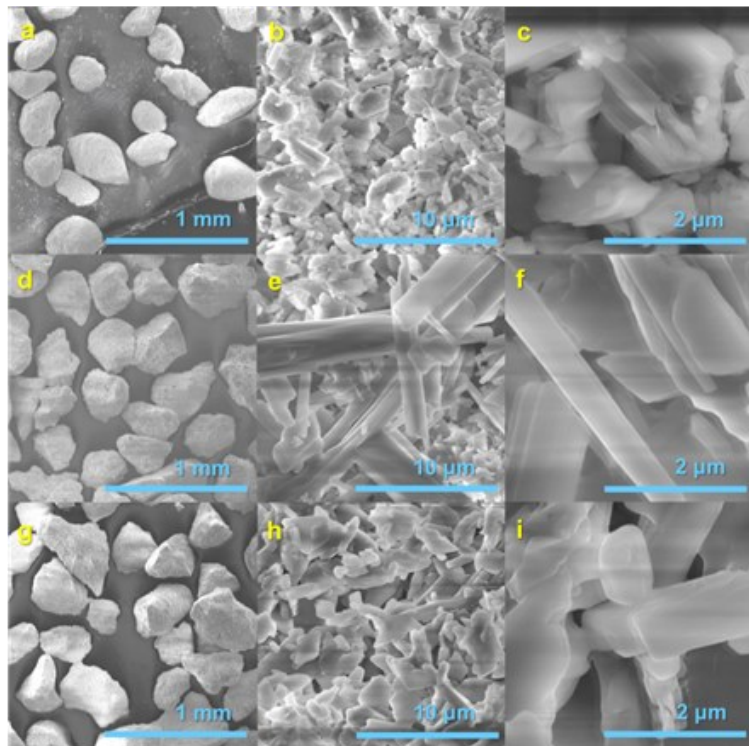
CDHA, which exhibits an absorption band in the vicinity of  $560\text{ cm}^{-1}$ . The FT-IR spectra of PR1/48h–PR3/48h granules display a series of absorption bands at  $1180\text{ cm}^{-1}$ ,  $1065\text{ cm}^{-1}$ ,  $1011\text{ cm}^{-1}$ ,  $954\text{ cm}^{-1}$ ,  $865\text{ cm}^{-1}$ , and within the  $600$ – $460\text{ cm}^{-1}$  range (see Figure 33c). These bands are ascribed to the P–O and P–O(H) stretching and deformation vibrations of the  $\text{PO}_4^{3-}$  and  $\text{HPO}_4^{2-}$  groups, which are distinctive of the crystal structure of the Mg-WH phase.



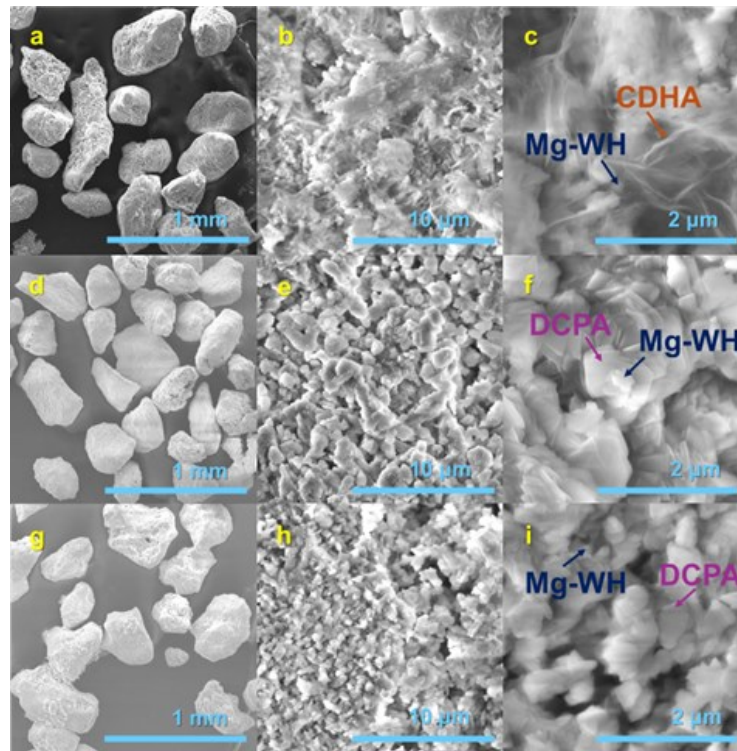
**Figure 33.** FT-IR spectra of R1–R3 (a), PR1/24h–PR3/24h (b), and PR1/48h–PR3/48h (c) granules synthesised *via* a dissolution-precipitation reaction.

Figure 34, Figure 35, and Figure 36 present the SEM micrographs of the synthesized R1–R3 raw granules, the PR1/24h–PR3/24h granules, and the PR1/48h–PR3/48h granules, respectively. A thorough inspection of the surface of  $200$ – $400\text{ }\mu\text{m}$  rough-edged raw granules discloses the presence of rod-like crystals, which are indicative of calcium sulfate dihydrate (see Figure 34a, d, g; surface views in Figure 34b, e, h). These crystals are accompanied by randomly oriented plate-shaped crystals, as observed in the higher-magnification images (see Figure 34c, f, i). The surface morphology of the irregularly shaped PR1/24h to PR3/24h granules shows notable variation, influenced by both the type of raw granules used and possible differences in local reaction environments during synthesis (see Figure 35a, d, g; surface views in Figure 35b, e, h). A thorough inspection of the surface of the PR1/48h–PR3/48h granules reveals that they are composed of interlocked spherical and rod-like particles, which are composed of fine crystals (see Figure 36a, d, g; surface views in Figure 36b, e, h). The higher magnification

SEM micrograph provides a detailed analysis of the granules, revealing their composition as a stack of characteristic Mg-WH rhombohedral crystals with an average size of approximately 150 – 200 nm (see Figure 36c, f) [35]. As illustrated in Figure 36i, the PR3/48h specimen displays a well-developed porous microstructure, which is composed of an assembly of plate-like crystallites with an approximate diameter of 200 nm.



**Figure 34.** SEM images of raw granules R1 (a-c), R2 (d-f), and R3 (g-i).



**Figure 35.** SEM images of PR1/24h (a-c), PR2/24h (d-f), and PR3/24h (g-i) granules.

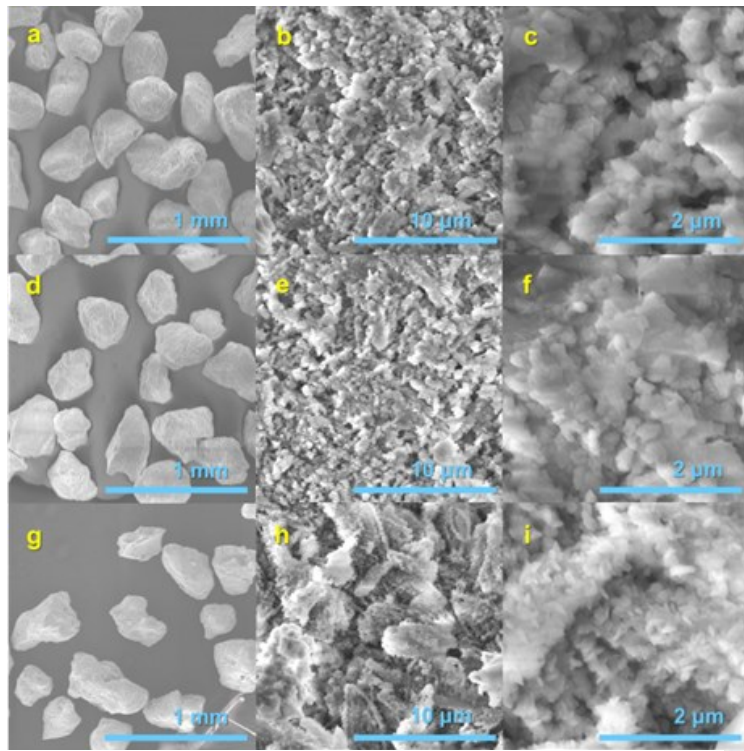


**Figure 36.** SEM images of PR1/48h (a-c), PR2/48h (d-f), and PR3/48h (g-i) granules.

A thorough examination of the textural characteristics of samples PR1/24h, PR2/24h, PR3/24h, PR1/48h, PR2/48h and PR3/48h, as determined by N<sub>2</sub> adsorption-desorption measurements, reveals significant differences in surface area and porosity characteristics (see Table 4).

**Table 4.** Data derived from N<sub>2</sub> adsorption-desorption measurements: S<sub>BET</sub>, S<sub>ext</sub> (external surface area), V <sub>$\mu$</sub> , and V<sub>p</sub> of all synthesized product samples.

Sample	PR1/24h	PR2/24h	PR3/24h	PR1/48h	PR2/48h	PR3/48h
S <sub>BET</sub> (m <sup>2</sup> /g)	35	4	30	9	11	38
S <sub>ext</sub> (m <sup>2</sup> /g)	30	3	27	7	8	35
V <sub><math>\mu</math></sub> (cm <sup>3</sup> /g)	0.0020	0.00050	0.0013	0.0011	0.0012	0.0011
V <sub>p</sub> (cm <sup>3</sup> /g)	0.13	0.010	0.069	0.025	0.027	0.077

PR1/24h, consisting of a biphasic mixture of Mg-WH and CDHA, exhibits the highest BET surface area (35 m<sup>2</sup>/g) and total pore volume (0.13 cm<sup>3</sup>/g), indicating a highly porous structure with significant external surface exposure. In contrast, PR2/24h, composed mainly of Mg-WH and a significant amount of monetite, has a much lower surface area (4 m<sup>2</sup>/g) and pore volume (0.010 cm<sup>3</sup>/g), reflecting a denser microstructure. PR3/24h, which contains Mg-WH and only a small amount of monetite, has intermediate properties with a relatively high surface area (30 m<sup>2</sup>/g) and moderate porosity (0.069 cm<sup>3</sup>/g). The PR1/48h, PR2/48h, and PR3/48h samples, each composed solely of the Mg-WH phase, were derived from three chemically distinct precursor granules. These samples exhibit marked differences in textural features as a result of their initial composition and synthesis conditions. Specifically, PR3/48h exhibited a substantially higher BET surface area (38 m<sup>2</sup>/g) in comparison to PR1/48h and PR2/48h, which registered values of 9 m<sup>2</sup>/g and 11 m<sup>2</sup>/g, respectively. The lower surface areas of PR1/48h and PR2/48h suggest denser, less permeable structures with reduced surface exposure, which may limit their bioactivity and hinder effective tissue integration. The samples display S<sub>ext</sub> (7 m<sup>2</sup>/g, 8 m<sup>2</sup>/g, and 35 m<sup>2</sup>/g for samples PR1/48h, PR2/48h, and PR3/48h, respectively) values that closely correspond to their S<sub>BET</sub>, indicating that the surface is predominantly external. Micropores account for a mere 12%, 17%, and 8%, respectively, of the total surface area for these specimens, indicating the mesoporous nature of the materials. This assertion is further substantiated by the uniformity in micropore volumes across all samples (V <sub>$\mu$</sub>  ≈ 0.0011 – 0.0012 cm<sup>3</sup>/g), thereby confirming the predominance of meso- to macroporous characteristics in the material. A significant disparity in total pore volume is evident among the samples, with

PR1/48h exhibiting a value of 0.025 cm<sup>3</sup>/g, PR2/48h measuring 0.027 cm<sup>3</sup>/g, and PR3/48h reaching 0.077 cm<sup>3</sup>/g. The significantly higher pore volume of PR3/48h indicates a more open and accessible structure, likely enhancing its interaction with biological environments, such as proteins, cells, and ions, and can be attributed to its finer particle morphology. In contrast, PR1/48h and PR2/48h exhibit markedly denser microstructures, characterized by diminished surface areas and pore volumes, as well as underdeveloped mesoporous architecture. This may have a deleterious effect on their performance in surface-driven biological or chemical processes.

#### 4. CONCLUSIONS

1. Large-scale synthesis (3.00 g per synthesis) of Mg-WH powder was successfully achieved with a 89% yield *via* a simple, cost-effective, environmentally benign dissolution-precipitation method starting from gypsum. Controlled formation of the pure Mg-WH phase was achieved by systematically varying the reaction duration. XRD analysis revealed a phase transition from DCPA to Mg-WH over 72 h. FT-IR analysis confirmed the presence of the  $\text{PO}_4^{3-}$  and  $\text{HPO}_4^{2-}$  groups in the Mg-WH phase obtained. The average crystallite size was determined to be 34 nm, with a degree of crystallinity of 78%. SEM-EDX analysis confirmed the formation of rhombohedral Mg-WH crystals ranging from 75 to 150 nm in size with a homogeneous distribution of the Ca, Mg, P, and O elements. The  $S_{\text{BET}}$  of the 72-hour Mg-WH sample was calculated to be 10  $\text{m}^2/\text{g}$ .
2. Mg-WH granules were formed using a scalable dissolution-precipitation synthesis process starting with gypsum-based granules. Each synthesis using 3.00 g of precursor granules resulted in 1.75 g of Mg-WH granules. The impact of pH on product composition was assessed, revealing that pure Mg-WH was obtained at a pH of 6.2. Phase purity was confirmed by XRD, LeBail refinement, and FT-IR spectroscopy. Synthesized Mg-WH granules exhibited a crystallinity degree of 60%. SEM analysis demonstrated that the granules had an average size of  $\sim 329 \mu\text{m}$  and were composed of rhombohedral particles averaging 70 nm in size. BET analysis revealed that the Mg-WH granules had a mesoporous structure and  $S_{\text{BET}}$  of 40  $\text{m}^2/\text{g}$ . Synthesis performed at a pH of 6.7 produced a biphasic sample containing 37 wt.% Mg-WH and 63 wt.% CDHA, as verified through XRD analysis and refinement. A significant advantage of this synthesis method is its ability to produce monophasic or biphasic materials, allowing selection of the most suitable option for applications.
3. Mg-WH granules were successfully fabricated through a tunable dissolution-precipitation procedure from three distinct precursor granules with chemical compositions modified by varying the proportions of diammonium hydrogen phosphate, magnesium hydrogen phosphate, and gypsum. The influence of reaction duration on product composition, morphology, and surface properties was investigated. The biphasic granules (Mg-WH with CDHA or Mg-WH with DCPA) formed within 24 h, while single-phase Mg-WH granules were achieved after 48 h of synthesis. FT-IR analysis confirmed the presence of characteristic functional groups of Mg-WH, CDHA, and DCPA in the intermediate

products, which were absent in the final products. SEM analyses revealed notable morphological transformations from the raw granules to the product granules, with the latter exhibiting interlocked spherical and rod-like agglomerates composed of fine Mg-WH crystals with an average size of approximately 150 – 200 nm. The study demonstrated that the surface area and porosity of Mg-WH-based granules are highly dependent on the composition of the precursor and the duration of the synthesis.

## SUMMARY IN LITHUANIAN

### SANTRUMPU SARAŠAS

BCP	Bifazis kalcio fosfatas
BET	Brunauer–Emmet–Teller
CaP	Kalcio fosfatas
CDHA	Kalcio deficitinis hidroksiapatitas ( $\text{Ca}_9(\text{HPO}_4)(\text{PO}_4)_5\text{OH}$ )
CS	Kalcio sulfatas ( $\text{CaSO}_4$ )
CSH	Kalcio sulfato hemihidratas ( $\text{CaSO}_4 \cdot 0.5\text{H}_2\text{O}$ )
DCPA	Bevandenis kalcio vandenilio fosfatas (monetitas; $\text{CaHPO}_4$ )
DCPD	Kalcio vandenilio fosfato dihidratas ( $\text{CaHPO}_4 \cdot 2\text{H}_2\text{O}$ )
DTG	Diferencinė termogravimetrija
EDX	Rentgeno spindulių energijos disperzija
FT-IR	Furje transformacinė infraraudonųjų spindulių spektroskopija
GYP	Kalcio sulfato dihidratas ( $\text{CaSO}_4 \cdot 2\text{H}_2\text{O}$ )
HAP	Kalcio hidroksiapatitas ( $\text{Ca}_{10}(\text{PO}_4)_6(\text{OH})_2$ )
ICDD	Tarptautinis difrakcijos duomenų centras
Mg-WH	Magnio vitlokitas ( $\text{Ca}_{18}\text{Mg}_2(\text{HPO}_4)_2(\text{PO}_4)_{12}$ )
$S_{\text{BET}}$	Specifinis paviršiaus plotas
SEM	Skenuojanti elektroninė mikroskopija
$S_{\text{ext}}$	Išorinis paviršiaus plotas
TG-DTG	Termogravimetrinė - diferencinė termogravimetrinė analizė
$V_p$	Bendras porų tūris
$V_\mu$	Mikroporų tūris
XRD	Rentgeno spindulių difrakcija

## IVADAS

Visame pasaulyje įvairios traumos įtakoja žmonių gyvenimo kokybę ir kelia rimtų iššūkių šalių sveikatos priežiūros sistemoms, nes kaulų defektai dažnai viršija natūralų jų gijimo pajėgumą ir reikalauja išorinės intervencijos. Dėl senėjančios visuomenės ir augančios populiacijos didėja sutrikimų, susijusių su kaulų defektais, paplitimas, o kartu ir kaulų implantų poreikis. Yra sukurtos įvairios sintetinės kalcio fosfatų (CaP) pakaitinės medžiagos, skatinančios naujo kaulinio audinio formavimąsi kaulų defektų vietose. Šie junginiai yra plačiai pritaikyti medicinoje ir odontologijoje, ypač dantų implantų, alveolių kaulo augmentacijos, ortopedijos ir vaistų pernašos sistemų srityse. CaP sulaukė daug dėmesio dėl savo išskirtinio biologinio suderinamumo, kontroliuojamo biologinio skaidumo, osteolaidumo ir sugebėjimo integruotis į kaulą. Šiuo metu sintetinės kaulo pakaitinės medžiagos gaminamos miltelių, granulių, tankių arba porėtų karkasų, bioaktyvių dangų ant metalinių protезų pavidalu.

Mokslinės bendruomenės yra priimta, kad kaulinio audinio neorganinę dalį sudaro karbonatinis apatitas ( $\text{Ca}_{10-a}(\text{PO}_4)_{6-b}(\text{CO}_3)_c(\text{OH})_{2-d}$ ). Pastaruoju metu aktyviai vyksta tyrimai dėl magnio vitlokito (Mg-WH:  $\text{Ca}_{18}\text{Mg}_2(\text{HPO}_4)_2(\text{PO}_4)_{12}$ ) vaidmens, svarbos ir egzistavimo kauliniame audinyje. Kai kurios mokslinės studijos atskleidžia, kad Mg-WH yra vienas iš pagrindinių neorganinių kaulinio audinio komponentų, sudarantis maždaug 25–35 masės % kietujų audinių. Tuo tarpu kiti tyrimai rodo, kad Mg-WH pirmiausia yra susijęs su kalcifikacijos procesais, susijusiais su patologinėmis būklėmis arba mineralizacija tam tikromis sąlygomis, pavyzdžiui, kalcifikuoto tendinito arba kalcifikuotų aterosklerozinių plokštelių susidarymo atvejais. Nors Mg-WH buvimas kauliniame audinyje tebėra diskutuotinas, tačiau jo sintetinė forma išsiskiria tarp kitų CaP pakaitalų dėl magnio ( $\text{Mg}^{2+}$ ) jonų struktūroje, kurie yra būtini įvairioms fiziologinėms žmogaus organizmo funkcijoms. Be to, fiziologinėmis sąlygomis iš kaulo pakaitinių medžiagų išsiskiriantys  $\text{Mg}^{2+}$  jonai, skatina osteogeninę diferenciaciją ir spartina kaulo susidarymą aplink implantus. Ankstesni tyrimai pabrėžė poreikį kurti didelio kiekio Mg-WH sintezės metodus, siekiant užtikrinti jo taikymą kaulų regeneracijoje ir biomedžiagų tyrimuose.

Odontologijoje ir ortopedijoje dažnai naudojamos sintetinės CaP pakaitinės medžiagos granulių pavidalu, siekiant regeneruoti kietuosius audinius, užpildyti netaisyklingos formos kaulų defektus ar įvairių formų tušumas. Granulės lengvai panaudojimos, efektyviai užpildo defekto vietą.

Nepaisant daug žadančio Mg-WH granulių potencialo kaulinio audinio inžinerijoje, šios formos Mg-WH tyrimų kol kas yra labai nedaug. Dauguma

mokslinių tyrimų orientuoti į Mg-WH miltelių sintezę ir tyrimus, ir, galbūt, tik vienoje mokslinėje publikacijoje nagrinėta granuliota jo forma.

Lee kartu su bendraautoriais nesenai apraše Mg-WH granulių sintezę iš Mg-WH nanodalelių, kurios buvo gautos panaudojant trijų tirpiklių sistemą. Gautos granulės pasižymėjo puikiomis kaulo regeneracinėmis savybėmis žiurkių kauliniuose defektuose, veiksmingai atkurdamos kaulo storį, nesukeliant jokių uždegiminių procesų. Sintetinis Mg-WH yra laikomas biomedžiaga, kuri potencialiai galėtų būti panaudota implantalogijoje, tačiau dėl sudėtingos jo grynos fazės sintezės, šios medžiagos savybių ir elgsenos tyrimų trūksta. Mg-WH sintezė vykdoma siaurame pH ir temperatūros intervale. Be to, Mg-WH yra termiškai nestabili fazė (Mg-WH suyra virš ~ 600 °C, susidarant Mg pakeisto  $\beta$ -Ca<sub>3</sub>(PO<sub>4</sub>)<sub>2</sub> ir Ca<sub>2</sub>P<sub>2</sub>O<sub>7</sub> mišiniui bei vandeniu), todėl ją sudėtinga susintetinti taikant įprastus aukštos temperatūros metodus. Be to, yra žinoma, kad įprastiniai aukštatemperatūriai sintezės metodai dažnai padidina galutinių produktų kristališkumą, o tai sumažina jų suderinamumą su biologiniais audiniais. Priešingai, mažo kristališkumo porėtos CaP granulės skatina kaulinio audinio gjimą, nes porėtumas yra būtinės bioaktyvumui ir osteolaidumui, o jo stoka gali turėti neigiamą poveikį šioms savybėms.

Sprendžiant šias problemas, galima pritaikyti tirpinimo-nusodinimo reakcijas gaminti žemo kristališkumo ir didelio specifinio paviršiaus porėtai keramikai. Pagrindinis šio metodo privalumas yra labai panašios pirmtako medžiagos formos išlaikymas galutiniame produkte. Be to, šis sintezės būdas leidžia gaminti granules – produktą, kuris gali būti tiesiogiai naudojamas kaulų augmentacijos procedūrose. Tirpinimo-nusodinimo metodas yra paprastas ir ekonomiškas, nereikalaujantis brangios, specializuotos įrangos, tokios kaip hidroterminiai reaktoriai ar aukštos temperatūros krosnys. Jis taip pat sumažina veiklos sąnaudas, nes neberekia nuolat stebeti esminių parametrų, tokį kaip temperatūra ir pH, lemiančių Mg-WH sintezės efektyvumą.

**Šios daktaro disertacijos tikslas** – ištirti tirpimo-nusodinimo metodų sintetinamų Mg-WH miltelių ir granulių fazinius virsmus, bei optimizuoti didelio produkto kiekiui gauti tinkamas sintezės sąlygas, užtikrinant Mg-WH miltelių ir granulių grynumą.

**Tyrimo uždaviniai yra šie:**

- ištirti Mg-WH produkto, gauto iš aplinkai nekenksmingo pirmtako – gipso miltelių susidarymą, priklausomai nuo sintezės laiko, ir įvertinti Mg-WH miltelių fazinę sudėtį ir grynumą, kristalografinius parametrus, funkcines grupes, terminį stabilumą, paviršiaus morfologiją, elementinę sudėtį ir paviršiaus savybes;

- nustatyti optimalias pH sąlygas Mg-WH granulių gavimui iš gipso granulių, įvertinti pH įtaką susidarančių fazių sudėčiai, nustatyti Mg-WH granulių grynumą, kristalografinius parametrus, funkcinės grupes, granulių dydį ir morfologiją, paviršiaus ir antibakterines savybes;
- sukurti įvairios cheminės sudėties pirmtakų granules, keičiant diamonio vandenilio fosfato, magnio vandenilio fosfato ir kalcio sulfato kiekius; ištirti jų transformaciją į bifazes arba vienfazes Mg-WH granules, įvertinti gautų granulių fazinę sudėtį ir grynumą, kristalografinius parametrus, funkcinės grupes, granulių morfologiją ir paviršiaus savybes.

## DISERTACIJOS NAUJUMAS

Šiame tyrime pristatoma inovatyvi Mg-WH sintezė, naudojant tirpimino-nusodinimo sintezės metodą, lenkiančia įprastus metodus reikšmingais pranašumais. Priešingai nei tradiciniai sintezės būdai, reikalaujantys brangios įrangos, ir nuolatinio kritinių parametrų, tokii kaip pH ir temperatūra, stebėjimo, siūlomas metodas supaprastina procesą, nemažinant sintetinamos medžiagos kokybęs. Šiame tyrime pirmą kartą Mg-WH granulių sintezei pirmtaku naudojamas gipsas - natūraliai gausi, ir aplinkai nekenksminga medžiaga, todėl sintezės tampa tvaresnė ir prieinamėsnė. Svarbu ir tai, kad šiame darbe pirmą kartą pasiūlyta didelio masto Mg-WH miltelių ir granulių pavidalo sintezės strategija, parodanti, kad metodas praktiškai pritaikomas pramoninei gamybbai. Be to, keičiant pirmtakų sudėtį ir reakcijos sąlygas, galima kontroliuoti Mg-WH fazinę sudėtį, dalelių morfologiją ir struktūrines savybes, kurios yra itin svarbios potencialiam pritaikymui. Tyrimo rezultatai atskleidžia siūlomo sintezės metodo universalumą, nes jis leidžia sintetinti tiek vienfazes, tiek bifazes kalcio fosfatų (BCP) medžiagas.

## GINAMIEJI TEIGINIAI

1. Didelio kieko Mg-WH miltelių ir granulių sintezė, atlikta paprastu, ekonomišku ir aplinkai draugišku tirpinimo-nusodinimo metodu, naudojant gipso pirmtaką, leidžia kontroliuoti fazinę produkto sudėtį, o struktūrinė, morfoliginė ir fazinės sudėties analizė patvirtina sintezės sąlygų optimizavimą.
2. Faziniai virsmai, vykstantys sintetinant Mg-WH miltelius gali būti tiriami keičiant reakcijos laiką. Mg-WH milteliai susideda iš romboedrinių kristalų, pasižymi homogeniniu Ca, Mg, P elementų pasiskirstymu ir kristalinės gardelės parametrais, atitinkančiais literatūroje pateiktas vertes.

3. Tirpinimo-nusodinimo metodu gautų granulių fazinė sudėtis gali būti kontroliuojama reakcijos mišinio pH. Siūlomas sintezės būdas yra universalus, nes jis leidžia sintetinti tiek vienfazes Mg-WH, DCPD, tiek BCP (Mg-WH su CDHA) granules.
4. Skirtingos morfologijos, paviršiaus savybių ir fazinės sudėties granulės gali būti susintetintos taikant darbe optimizuotą tirpimo-nusodinimo sintezę. Keičiant pirmtako granulių sudėtį ir reakcijos laiką, galima gauti tiek bifazes (Mg-WH su CDHA arba Mg-WH su DCPA), tiek vienfazes Mg-WH granules.

## DISERTACIJOS SANDARA

Disertacija parašyta anglų kalba ir susideda iš šių dalių: įvado, santrumpų, literatūros apžvalgos, eksperimentinės dailies, tyrimų rezultatų bei jų aptarimo, išvadų, santraukos lietuvių kalba, cituojamų literatūros šaltinių sąrašo, publikacijų sąrašo, konferencijų sąrašo, padékos. Darbe pateikiamos 4 lentelės ir 36 paveikslai. Bendra disertacijos apimtis 136 lapai. Darbe cituojami 255 literatūros šaltiniai.

### 1. LITERATŪROS APŽVALGA

Literatūros apžvalgoje poskyryje 1.1. pateikiamas informacija apie kaulinj audinį, jo struktūrą, remodeliavimo eigą. Kitoje dalyje aptariamas sintetinių pakaitinių medžiagų poreikis (poskyris 1.2.). Poskyryje 1.3 apžvelgiamos kalcio fosfatinės (CaP) sintetinės pakaitinės biomedžiagos, aprašomos jų pagrindinės savybės, dažniausiai medicinos praktikoje naudojamos formos bei Mg-WH savybės. Paskutiniajame poskyryje pristatomos pagrindiniai kalcio fosfatų gavimo būdai, išsamiau aptariamas šiame darbe taikytas tirpinimo-nusodinimo sintezės metodas bei apžvelgiami Mg-WH sintezės būdai ir galimos jo taikymo sritys.

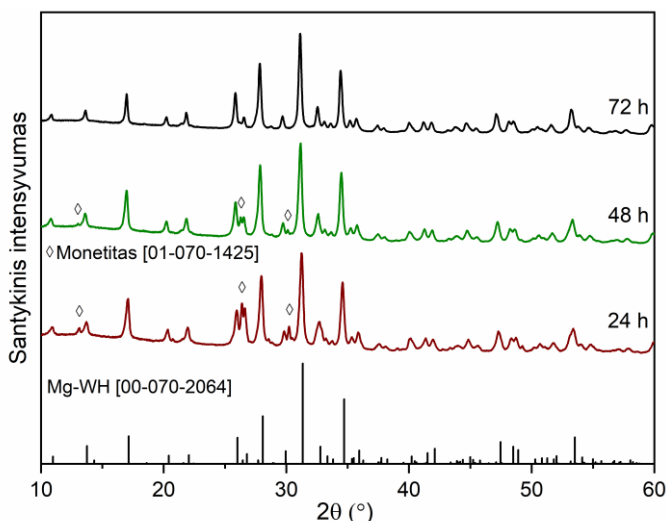
### 2. EKSPERIMENTO METODIKA

Šią dalį sudaro trys pagrindiniai poskyriai, iš kurių antrasis padalintas į tris skyrelius. Pirmajame poskyryje išvardyti cheminiai reagentai, panaudoti medžiagų sintezei ir ištyrimui, pateikti jų grynumai ir gamintojai. Sintezės metodikos poskyryje aprašyti skirtinės formos Mg-WH sintezės būdai. Skyrelyje 2.2.1. pateiktos didelio kiekio Mg-WH miltelių skirtinės trukmės sintezės iš gipso pirmtako. Skyrelyje 2.2.2 aprašyta Mg-WH granulių gamyba, įvertinant reakcijos mišinio tirpalo pH įtaką galutinių produktų sudėčiai. Paskutiniame 2.2.3 skyrelyje pateikta skirtinės morfologijos Mg-WH granulių sintezė iš vieninių ir mišrių pirmtako granulių. Paskutiniame poskyryje aprašomi susintetintų mėginių tyrimo ir apibūdinimo metodai, jų specifinės atlikimo sąlygos ir naudoti prietaisai.

### 3. REZULTATAI IR JŪ APTARIMAS

### 3.1. Didelio kieko Mg-WH miltelių sintezė ir apibūdinimas

Tirpinimo-nusodinimo metodu iš gipso (kalcio sulfato dihidrato,  $\text{CaSO}_4 \cdot 2\text{H}_2\text{O}$ , GYP) miltelių, magnio acetato tetrahidrato ( $\text{Mg}(\text{CH}_3\text{COO})_2 \cdot 4\text{H}_2\text{O}$ ), natrio divandenilio fosfato ( $\text{NaH}_2\text{PO}_4$ ) ir dinatrio vandenilio fosfato ( $\text{Na}_2\text{HPO}_4$ ) buvo susintetinti Mg-WH milteliai. Tyrime įvertinti faziniai virsmai, priklausomai nuo reakcijos trukmės. Gautų produktų fazinių ir cheminių sudėties nustatymas, morfologijos, terminio stabilumo, paviršiaus savybių tyrimai buvo atlikti įvairiais analizės metodais. Siekiant nustatyti optimalų reakcijos laiką didelio kieko grynos Mg-WH fazės susidarymui, sintezės trukmė buvo keista nuo 24 iki 72 val., išlaikant pastovią  $80^\circ\text{C}$  sintezės temperatūrą (žiūrėti 1 paveikslą).

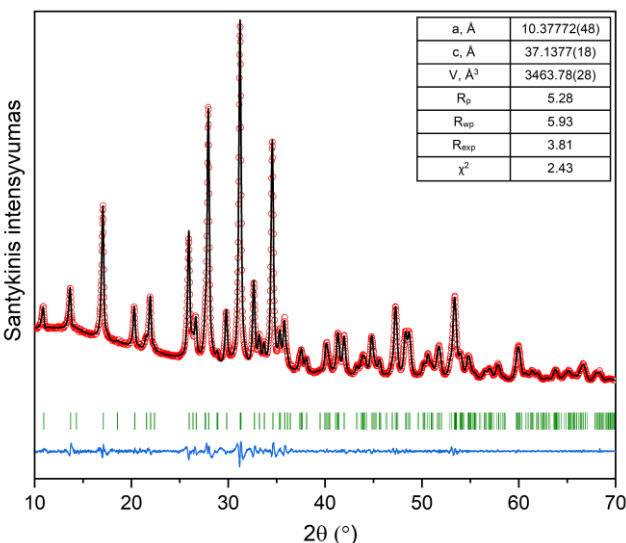


**1 pav.** Mg-WH miltelių, sintezę vykdant 24–72 h, XRD. Apačioje esančios vertikalios linijos žymi standartinius Mg-WH XRD atspindžius (ICDD #00-070-2064).

Susintetintų mėginių XRD rezultatai atskleidė, kad po 24 ir 48 val. susidarė bifaziniai mišiniai, susidedantys iš monetito ( $\text{CaHPO}_4$ ; DCPA; ICDD #01-070-1425) ir Mg-WH. Yra žinoma, kad DCPA yra stabiliausia kalcio fosfato (CaP) fazė, kai reakcijos terpės pH yra mažesnis nei 5. Tačiau yra žinoma, kad DCPA stabilumą įtakoja tirpale esantys  $\text{Mg}^{2+}$  jonai. Dėl  $\text{Mg}^{2+}$  jonų poveikio silpnai rūgščiame tirpale DCPA formavimasis yra slopinamas, o tai skatina Mg-WH fazės susidarymą iš GYP per tarpine DCPA fazę. 1 paveiksle matyti,

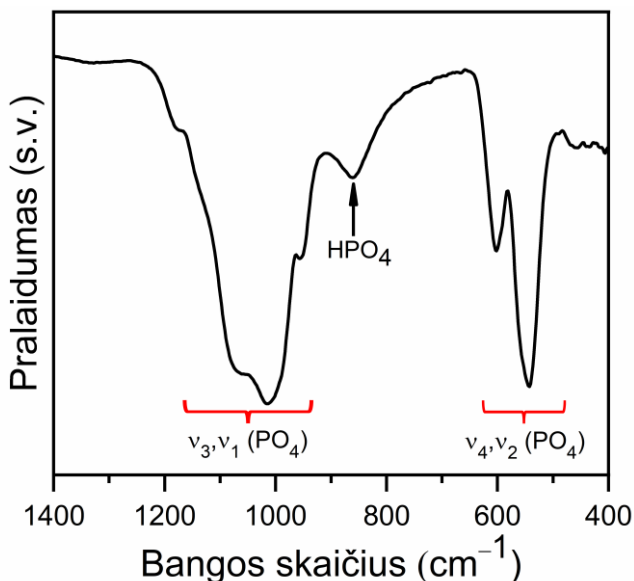
kad DCPA kiekis sumažėjo, o Mg-WH padidėjo, kai reakcijos trukmė pailgėjo nuo 24 iki 48 val. Nustatyta, kad po 24 val. mèginį sudarė 35 masës % DCPA ir 65 masës % Mg-WH, o po 48 val. mèginys susidėjo iš tų pačių sudedamujų dalių, tačiau Mg-WH fazę buvo pagrindinę (78 masës %), DCPA komponentas sudarė tik 22 masës %. Ilginant reakcijos laiką iki 78 val., XRD matomos tik Mg-WH fazei bûdingos smailës. Pažymétina, kad darbe išvystyta sintezës metodika leidžia viename reakcijos indelyje iš 5,00 g GYP miltelių susintetinti 3,00 g Mg-WH miltelių.

Siekiant papildomai ivertinti susidariusio produkto grynumą ir nustatyti jo struktūrinius parametrus, 72 val. sintetinto mèginio iš XRD duomenų buvo atliktas Le Bail metodu tikslinimas, naudojant *FullProf* programą. Eksperimentiniai XRD duomenys atitiko Mg-WH junginiui bûdingus standartinës difraktogramos smailių atspindžius, patvirtino tipinę Mg-WH romboedrinę kristalinę struktûrą (R3c (#161) erdinë grupë), o nustatyti struktūriniai gardeles parametrai sutapo su atitinkamais mokslinës literatûros duomenimis (žiûreti 2 paveikslą). Patikslinimo rezultatai gerai atitiko eksperimentiškai išmatuotus difrakcijos profilius, o tai patvirtino, kad mèginyje yra vienfazis Mg-WH. Nustatyta, kad susintetinti Mg-WH milteliai buvo sudaryti iš 34 nm kristalitų, kristališkumo laipsnis siekë 78 %.



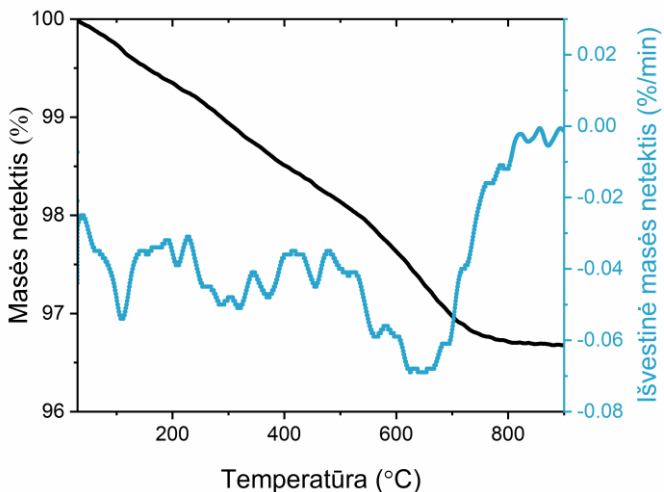
**2 pav.** Mg-WH miltelių, gautų sintezę vykdant 72 val., XRD su Le Bail tikslinimo kontûru (raudoni apkritimai žymi eksperimentinius duomenis; ištisinë juoda linija rodo patikslintus duomenis; melyna linija vaizduoja skirtumą tarp eksperimentinių ir patikslintų duomenų; žalios spalvos vertikalës brûkšneliai nurodo Brego padëtis).

Siekiant identifikuoti 72 val. sintetinto Mg-WH mèginio struktûroje esančias funkcinės grupes, buvo atlikta miltelių FT-IR analizë (žiûrëti 3 paveikslą). Spektre stebimi virpesiai, susiję su  $\text{PO}_4^{3-}$  ir  $\text{HPO}_4^{2-}$  funkcinėmis grupėmis. Virpesių rinkinys ties  $1171 \text{ cm}^{-1}$ ,  $1134 \text{ cm}^{-1}$ ,  $1064 \text{ cm}^{-1}$ ,  $1013 \text{ cm}^{-1}$  ir  $954 \text{ cm}^{-1}$  atitinka P–O ryšio tempimo  $v_3$  ir  $v_1$  virpesius. Plati absorbcijos juosta, kurios centras yra ties  $861 \text{ cm}^{-1}$ , žymi P–O(H) ryšio, bûdingo Mg-WH kristalinei struktûrai, tempimą. Juostos ties  $601 \text{ cm}^{-1}$ ,  $542 \text{ cm}^{-1}$  ir  $459 \text{ cm}^{-1}$ , yra susijusios su P–O ryšio ir O–P–O lenkimo virpesiais, atitinkamai pažymëtais  $v_2$  ir  $v_4$ .



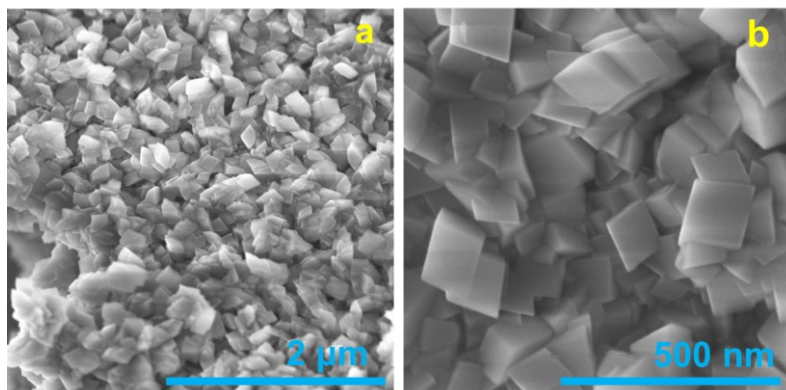
**3 pav.** Mg-WH miltelių, gautų sintezę vykdant 72 val., FT-IR spektras.

Siekiant nustatyti 72 val. sintetinto Mg-WH mèginio terminio skilimo eigą, buvo atliktas TG-DTG tyrimas. 4 paveiksle pateiktos analizuojamo mèginio TG-DTG kreivës. Iš mokslinës literatûros šaltinių žinoma, kad Mg-WH struktûroje esančios  $\text{HPO}_4^{2-}$  grupës kondensacija vyksta maždaug  $600 \text{ }^{\circ}\text{C}$  temperatûroje. Skilimo metu susidaro Mg jonas pakeistas  $\beta$ -trikalcio fosfatas ( $\beta\text{-Ca}_3(\text{PO}_4)_2$ ), kalcio pirofosfatas ( $\text{Ca}_2\text{P}_2\text{O}_7$ ) bei vanduo, o teorinë masës netektis yra mažesnë nei 1 %. Palaipsniui kaitinant tiriamą mèginį, jo masë mažéjo iki  $750 \text{ }^{\circ}\text{C}$  ir bendra masës netektis sieké maždaug 3 masës %. Masës netekties skirtumas, palyginti su mokslinëje literatûroje pateiktais duomenimis, greičiausiai atsirado dël terminio apdorojimo metu nuo susintetintos medžiagos paviršiaus pasišalinusio absorbuoto vandens.



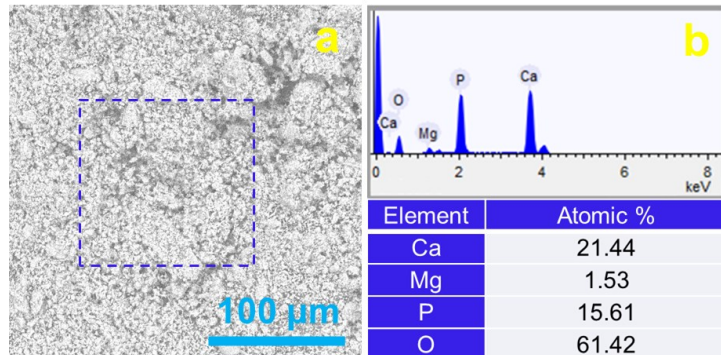
**4 pav.** Mg-WH miltelių, gautų sintezę vykdant 72 val., TG/DTG kreivės.

Susintetinto Mg-WH miltelių mèginio paviršiaus morfologija buvo tirta SEM metodu (žiūrëti 5 paveikslą). Gauri SEM vaizdai atskleidë, kad mèginio paviršių sudaro Mg-WH bûdingi romboedro formos kristalai su smailiomis viršunémis ir aštriomis kraštinémis, kurių dydis svyruoja nuo 75 iki 150 nm. Be to, pastebëta, kad miltelių mèginio paviršius yra šiek tiek porëtas (5a paveikslas), o tai gali bûti naudinga biomedicininiam taikymui, nes porëtumas gali skatinti lâstelių adheziją bei biologinių skysčių patekimą į sintetinį CaP. Didesnio didinimo SEM vaizdas (5b paveiksllo nuotrauka) parodë homogeniškas, lygaus paviršiaus produkto daleles, kas papildomai patvirtina, jog mèginys yra vienfazis ir neturi jokių kitų kristalinių intarpų ar priemaišų. Šis rezultatas atitinka XRD analizës duomenis, rodančius vienfazés Mg-WH struktûros susidarymą.



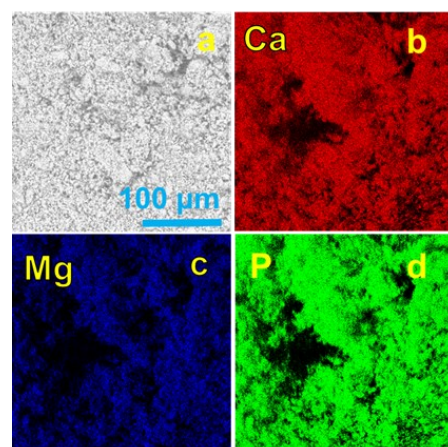
**5 pav.** Mg-WH miltelių, gautų sintezę vykdant 72 val., skirtingo didinimo SEM nuotraukos.

Norint įvertinti cheminių elementų pasiskirstymo tolygumą bei nustatyti susintetinto Mg-WH mėginio sudėtį, buvo atlikta jo EDX spektroskopijos analizė. Šis tyrimo metodas leido identifikuoti mėginyje esančius cheminius elementus ir jų kiekybinius santykius. Kaip matyti 6 paveiksle, galutinis produktas susideda iš kalcio (Ca), magnio (Mg), fosforo (P) ir deguonies (O) atomų, būdingų Mg-WH fazei.



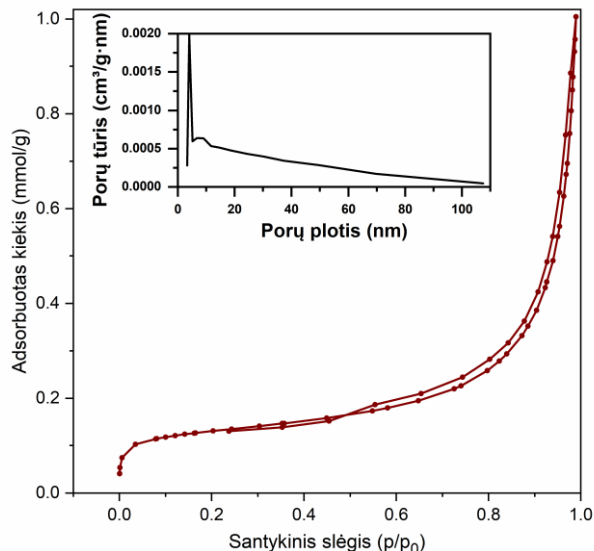
**6 pav.** Mg-WH milteliu, gautų sintezę vykdant 72 val., (a) SEM nuotrauka ir (b) EDX spektras bei nustatytos Ca, Mg, P, O elementų atominės koncentracijos procentais.

7a–d paveiksle pavaizduotas Ca, Mg ir P elementų pasiskirstymas. Rezultatai atskleidė, kad šie elementai yra tolygiai išsidėstę visame mėginyje. Svarbu paminėti, kad nebuvo pastebėta jokių segregacijos ar papildomų fazių susidarymo požymių, o tai patvirtina aukštą mėginio elementų sudėties homogeniškumo lygi.



**7 pav.** Mg-WH milteliu, gautų sintezę vykdant 72 val., (a) SEM nuotrauka ir (b) Ca, (c) Mg, ir (d) P elementų pasiskirstymo EDX žemėlapiai.

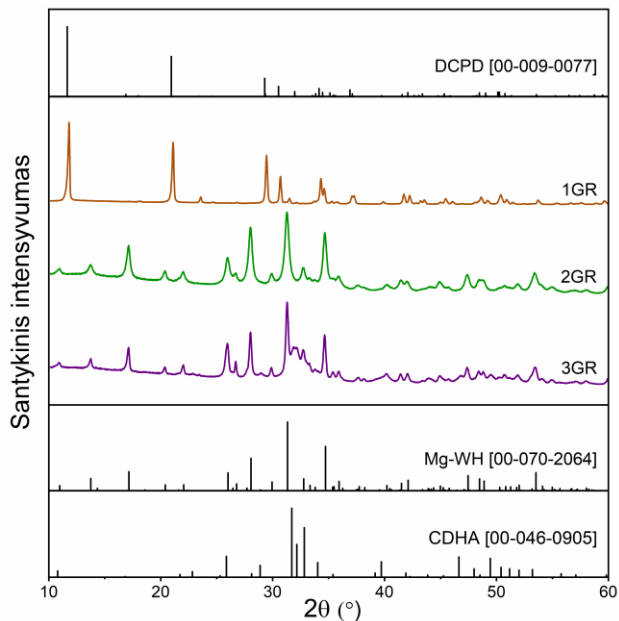
8 paveiksle pavaizduota Mg-WH miltelių, gautų sintezę vykdant 72 val.,  $N_2$  adsorbcijos-desorbcijos kreivė. Esant labai žemam santykiniam slėgiui, adsorbcijos kreivė yra jidubusi p/p<sub>0</sub> ašies atžvilgiu, pereinanti į pusiau linijinį segmentą vidurinėje atkarpoje ir sparčiai didėjanti, kai p/p<sub>0</sub> > 0,6. Esant aukštam santykiniam slėgiui mèginio adsorbuoto  $N_2$  kiekis gali didėti be apribojimų, kai p/p<sub>0</sub> artėja prie 1. Kadangi adsorbcija nepasiekė soties, nustatyta, kad mèginyje yra makroporų. Atliekant analizę, stebimas  $N_2$  adsorbcijos ir desorbcijos kreivių nesutapimas: siauras tarpas tarp adsorbcijos ir desorbcijos šakų bei histerezės kilpa, atsirandanti mažėjant slėgiui.  $N_2$  adsorbcijos ir desorbcijos kreivės atitinka mišrų II ir IV izotermų tipą su H3 tipo histerezės kilpa. Paprastai neporétiems ir makporétiems adsorbentams (kai porų skersmuo yra didesnis nei 50 nm) būdingos II tipo izotermos, o mezoporiniams adsorbentams (kai porų skersmuo yra nuo 2 nm iki 50 nm) – IV tipo izotermos. H3 tipo kilpos būdingos nestandžių plokštelių formos dalelių sankaujoms, dėl kurių susidaro plyšio pavidalo poros, atsirandančios dėl kristalų sankaujų. 8 Paveikslėlėje pavaizduota trito mèginio porų dydžių pasiskirstymo kreivė, o vyraujanti smailė (viršunė ties 4 nm) žymi mezoporas. Mg-WH mèginio specifinis paviršiaus plotas ( $S_{BET}$ ), apskaičiuotas naudojant Brunauer–Emmet–Teller (BET) lygtį, lygus 10 m<sup>2</sup>/g.



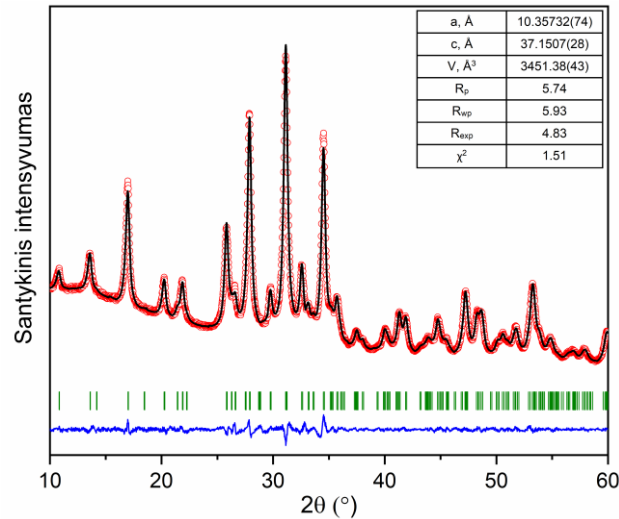
**8 pav.** Mg-WH miltelių, gautų sintezę vykdant 72 val.,  $N_2$  adsorbcijos-desorbcijos bei porų dydžių pasiskirstymo kreivės.

### 3.2. Didelio kieko Mg-WH granulių sintezė ir apibūdinimas

Tirpinimo-nusodinimo sintezės metodu iš anksčiau susintetintų GYP granulių buvo gautos Mg-WH granulės. Norint pasirinkti optimalų pH, reikalingą Mg-WH fazės susidarymui, sintezė buvo vykdoma pirmtako GYP granules atskirai merkiant į trijų skirtingų molinių santiukių  $\text{NaH}_2\text{PO}_4$  ir  $\text{Na}_2\text{HPO}_4$  tirpalų mišinius, į kuriuos papildomai buvo pridėtas tam tikros koncentracijos  $\text{Mg}(\text{CH}_3\text{COO})_2$  tirpalas. Šiame tyime buvo įvertinta gautų produktų fazinė sudėtis, priklausomai nuo skirtingo fosfatinių tirpalų santiukio, kuris nulémė reakcijos mišinio pH ir įtakojo galutinę produktų fazinę sudėtį. Tyrimas buvo vykdomas prie skirtingų pH: 5,7 (susintetintos 1GR granulės), 6,2 (susintetintos 2GR granulės) ir 6,8 (susintetintos 3GR granulės). Eksperimentai buvo vykdomi 80 °C temperatūroje ir truko 5 dienas. 9 paveiksle pavaizduotos susintetintų mèginį XRD. Kai reakcijos mišinio pH = 5,7, susintetintas mèginys buvo sudarytas iš kalcio vandenilio fosfato dihidrato ( $\text{CaHPO}_4 \cdot 2\text{H}_2\text{O}$ ; DCPD; ICDD #00-009-0077) fazės. DCPD apibūdinamas kaip metastabili fazė, dominuojanti esant vidutiniškai rūgščiam tirpalui. Pagal mokslinės literatūros duomenis žinoma, kad magnio jonai reakcijos tirpale apsunkina DCPD transformacijai į termodinamiškai stabilias CaP fazes, tokias kaip oktakalcio fosfatas ( $\text{Ca}_8(\text{HPO}_4)_2(\text{PO}_4)_4 \cdot 5\text{H}_2\text{O}$ ), kalcio deficitinis hidroksiapatitas (CDHA;  $\text{Ca}_9(\text{HPO}_4)(\text{PO}_4)_5\text{OH}$ ) ir kalcio hidroksiapatitas (HAP;  $\text{Ca}_{10}(\text{PO}_4)_6(\text{OH})_2$ ), net esant padidintoms reakcijos terpės pH vertėms. Nustatyta, kad DCPD kristalai virsta į Mg-WH, kai tirpalo pH yra 4,5, esant magnio jonas. Tačiau, atliekant tirpinimo-nusodinimo sintezę pasirinktomis sąlygomis, Mg-WH nesusidarė. Kai reakcijos mišinio pH buvo 6,2, susintetintas 2GR produktas kristalizavosi, sudarydamas Mg-WH būdingą romboedrinę kristalinę struktūrą, o difrakcijos smailės buvo priskirtos R3c (#161) erdvinei grupei (ICDD #00-070-2064). Difraktogramoje nebuvo pastebėta jokių smailių, kurios būtų susijusios su reagentais ar priemaišinėmis CaP fazėmis, kas patvirtina, kad gautas 2GR produktas yra vienfazis. 2GR mèginio XRD difraktograma su Le Bail tikslinimo difraktogramos kontūru pateikta 10 paveiksle. Patikslinus gardelės parametrus, buvo gauta:  $a = b = 10,357(74)$  Å,  $c = 37,15(275)$  Å,  $\alpha = \beta = 90^\circ$  ir  $\gamma = 120^\circ$ . Elementariojo narvelio tūris sudarė  $3451,15(433)$  Å<sup>3</sup>. Gauti struktūriniai parametrai puikiai atitinka literatūroje pateiktas reikšmes.



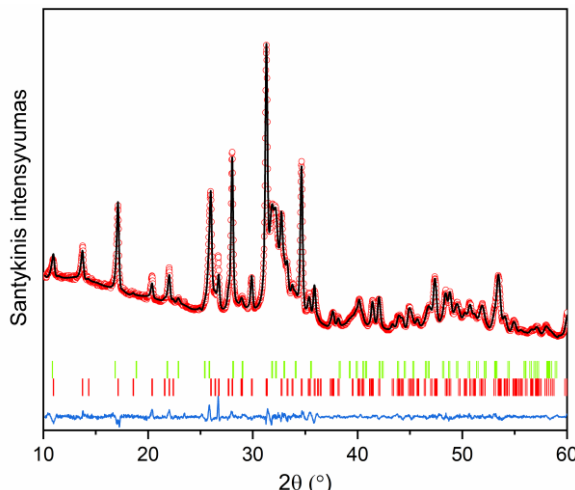
**9 pav.** 1GR, 2GR ir 3GR mèginių, susintetintų esant skirtingiems reakcijos mišinio pH, XRD. Difraktogramų smailës identikuotas pagal standartines DCPD, Mg-WH ir CDHA fazių korteles.



**10 pav.** 2GR mègino XRD difraktograma su Le Bail tikslinimo konturu (raudoni apkritimai nurodo eksperimentinius duomenis; ištisinë juoda linija žymi patikslintus duomenis; melyna linija vaizduoja skirtumą tarp eksperimentinių ir patikslintų duomenų; žalias spalvos vertikalūs brûkšneliai nurodo Brego padëtis).

Pažymėtina, kad 2GR mèginio difrakcinës smailës buvo šiek tiek išsiplėtusios. Tokio pobūdžio difrakcinës smailës dažnai susidaro, kai medžiaga turi ne tik kristalinių, bet ir amorfinių struktūrinių dalių, taip pat kai medžiagą sudarantys kristalitai yra labai mažo dydžio. Skaičiavimais buvo nustatyta, kad susintetintos Mg-WH granulës sudarytos iš kristalitų, kurių vidutinis dydis yra apie 16 nm, kas rodo, kad medžiaga yra nanometrinio dydžio. Be to, medžiagos kristališkumo laipsnis siekë 60 %, kas patvirtina, jog medžiaga turi tam tikrą amorfinį komponentą.

Kai reakcijos mišinio pH = 6,7, mèginyje buvo identikuotos romboedrinës kristalinës Mg-WH struktûros smailës bei papildomos mažo intensyvumo smailës ties  $2\theta \approx 31.73^\circ$  ir  $2\theta \approx 32.20^\circ$ , priklausančios kalcio deficitinio hidroksiapatito ( $\text{Ca}_9(\text{HPO}_4)(\text{PO}_4)_5\text{OH}$ ; CDHA; ICDD #00-046-0905) fazei. 3GR mèginio kiekybinei sudëčiai nustatyti atliktas Rietveld struktûros patikslinimas (žiûrëti 11 paveikslą).



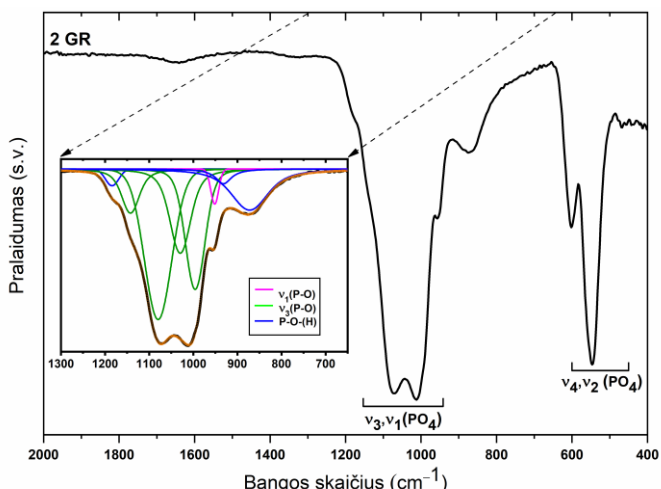
**11 pav.** 3GR mèginio XRD difraktograma su Rietveld tikslinimo kontûru.

Raudonos spalvos vertikalûs brûkšneliai nurodo Mg-WH fazës smailių padétis [ICDD #00-070-2064], o šviesiai žali – CDHA fazës smailių Brego padétis [ICDD #00-046-0905].

Patikslinimo rezultatai atitiko eksperimentiškai išmatuotus difrakcijos profilius, o tai patvirtino, kad mèginyje yra tik Mg-WH ir CDHA fazës. Nustatyta, kad 3GR mèginys sudarytas iš 37 masës % Mg-WH ir 63 masës % CDHA. Kai reakcijos mišinje pH yra didesnis nei 4,5,  $\text{Mg}^{2+}$  jonais nepakeisti CaP laipsniškai virsta CDHA. Todël esant didesnëms pH vertëms (šiuo atveju pH = 6,7), net ir esant  $\text{Mg}^{2+}$ , susidarë termodynamiškai stabilesnë CDHA fazë. Šiame darbe pasiûlytu sintezës metodu ir taikytomis sàlygomis gautas BCP

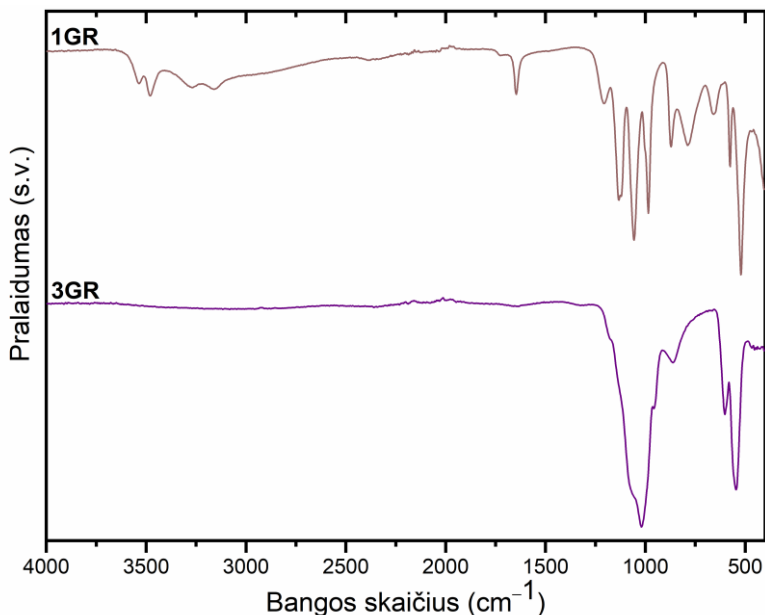
pabréžia metodo pranašumus, nes šios medžiagos yra plačiai naudojamos medicininėje praktikoje, ypač kaip kaulo pakaitalai ir regeneracinių implantų. Dviejų fazų buvimas šiose medžiagose yra itin svarbus, nes jis lemia tam tikras fizines ir biologines savybes, iškaitant rezorbcijos greitį, mechaninį stabilumą ir biologinį suderinamumą. Šis BCP susidarymas parodo, kad taikytas sintezės metodas yra perspektyvus kuriant medžiagas, kurių degradacijos savybės gali būti kontroliuojamos pagal biomedicininius poreikius.

Norint nustatyti susintetintų granulių struktūrose esančias funkcines grupes, buvo atlikta 1GR–3GR granulių FT-IR analizė. Susintetinto 2GR mèginio FT-IR spektras pateiktas 12 paveiksle, o 1GR ir 3GR granulių spektrai pateikti 13 paveiksle. Mg-WH kristalinėje struktūroje esantis fosfato jonas ( $\text{PO}_4^{3-}$ ) turi keturis IR aktyvius virpesio režimus:  $v_1$ ,  $v_2$ ,  $v_3$  ir  $v_4$ . Smailės ties maždaug  $603 \text{ cm}^{-1}$ ,  $544 \text{ cm}^{-1}$  ir  $464 \text{ cm}^{-1}$  atitinka  $v_4(\text{PO}_4^{3-})$  ir  $v_2(\text{PO}_4^{3-})$  lenkimo režimus.  $1180 \text{ cm}^{-1}$ ,  $1071 \text{ cm}^{-1}$ ,  $1011 \text{ cm}^{-1}$  ir  $956 \text{ cm}^{-1}$  virpesių rinkinys yra susijęs su  $v_3(\text{PO}_4^{3-})$  ir  $v_1(\text{PO}_4^{3-})$  tempimo režimais. Plati absorbcijos smailė, esanti ties  $869 \text{ cm}^{-1}$ , priskirta P-O(H) ryšio, esančio Mg-WH struktūroje, tempimo virpesiui. 12 paveiksle pavaizduotame FT-IR spektre nematyti Mg-WH kristalinei struktūrai būdingos juostos ties  $920 \text{ cm}^{-1}$ , kuri atitinka  $\text{HPO}_4^{2-}$  grupės P-O(H) ryšio tempimo režimą. Taip galėjo nutikti dėl juostų persiklojimo, kuris galimai susijęs ribotu atominiu išsidėstymu (žemu kristališkumu) tiriamajame 2GR mèginyje.



**12 pav.** 2 GR mèginio FT-IR spektras. Intarpe pavaizduoti eksperimentiniai duomenys pavaizduoti kartu su išskaidytomis ir sutapatintomis kreivėmis  $1300\text{--}650 \text{ cm}^{-1}$  intervale.

Spektro intervale nuo 1300 iki  $650\text{ cm}^{-1}$  atliktas spektrinių juostų išskaidymas, siekiant iš eksperimentinio FT-IR spektro išskirti atskirus persiklojančių juostų komponentus. Spektro išskleidimo metu šiame intervale buvo išskirtos aštuonios subjuostos, atkuriant spektrą taip, kad gauta kreivė būtų kuo artimesnė pradinei eksperimentiškai gautai spektrinei kreivei. Tai užtikrino tikslesnį vibracinių juostų padėčių nustatymą ir leido aptikti smulkesnius spektrinius komponentus. Išskaidytame spektre buvo identifikuota nepastebėta siaura absorbcijos juosta, kurios centrinė padėtis nustatyta ties  $931\text{ cm}^{-1}$ . Šios smailės spektrinės padėties nuokrypis nuo  $920\text{ cm}^{-1}$  gali būti siejamas su defektais kristalinėje struktūroje.

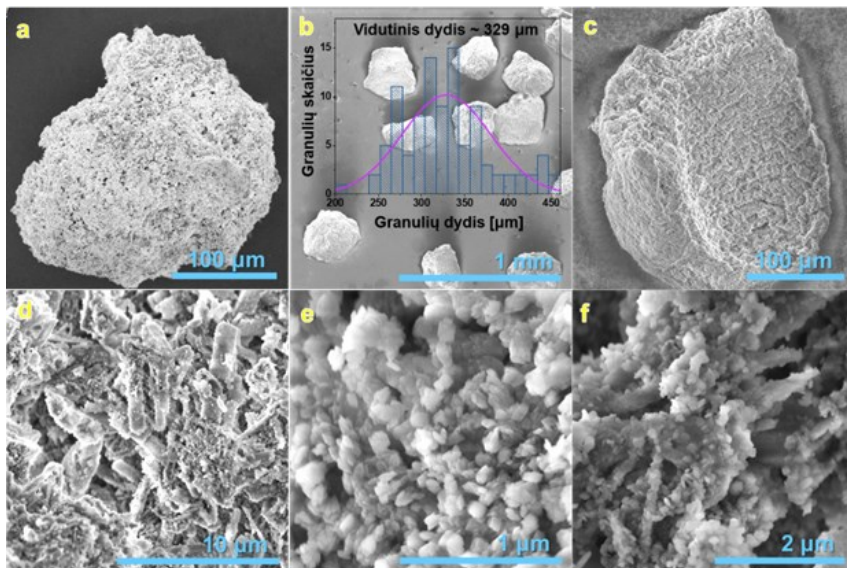


**13 pav.** 1GR ir 3GR mèginių FT-IR spektrai.

1GR mègino FT-IR spektre buvo identifikuotos fosfatų grupëms ( $\text{PO}_4^{3-}$  ir  $\text{HPO}_4^{2-}$ ) bûdingos absorbcijos juostos (žiûrëti 13 paveikslą). Taip pat identifikuota juosta ties  $1646\text{ cm}^{-1}$ , kuri atitinka struktûrių vandens molekulių, esançiu DCPD fazëje, nustatytoje ir XRD tyrimo metu, lenkimo virpesius. Lyginant vienfazio Mg-WH (2GR) mègino ir bifazio 3GR mègino, sudaryto iš Mg-WH ir CDHA fazių, FT-IR spektrus, išryškéjo tam tikri skirtumai. Visû pirma, 3GR mèginyje juostos, susijusios su Mg-WH faze, ypač ties  $1071\text{ cm}^{-1}$ , pasizymiai padidëjusi intensyvumu, kas rodo šios fazës kiekio mažëjimą bifaziam mèginyje. Be to, reikšmingas pokytis pastebimas P-O asimetrinio tempimo juostoje: jei 2GR mèginyje ši smailë buvo ties  $1011$

$\text{cm}^{-1}$ , tai 3GR mèginyje ji pasislinko į didesnius bangos skaičius ir yra ties  $1019 \text{ cm}^{-1}$ . Toks poslinkis patvirtina CDHA fazès susidarymą 3GR mèginyje, nes šios fazès pasižymi skirtingomis fosfatų grupių vibraciniemis savybėmis.

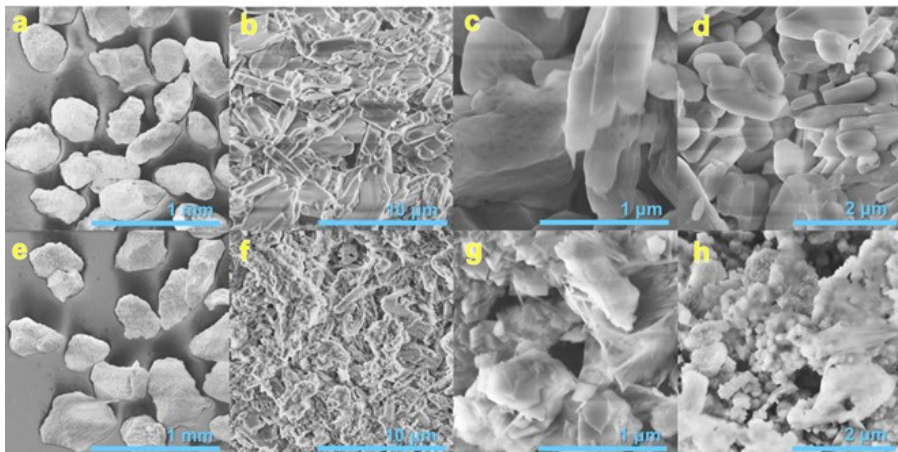
Pradinio pirmtako GYP granulių ir susintetintų 1GR–3GR granulių morfologija buvo ištirta atliekant SEM analizę (žiūrēti 14, 15 paveikslus). GYP granulių paviršius pasižymi nevienalytę struktūrą, sudarytą iš dalelių klasterių, kurie suformuoja nevienalytį reljefą. Be to, granulės paviršius pasižymi mikroporétymu – tame tolygiai pasiskirsčiusios smulkios poros ir tušumas (žiūrēti 14a paveikslą). 14b Paveiksle matyti neapibrėžtos formos 2GR granulės kartu su jų ilgio pasiskirstymo histograma. 2GR mèginio granulių ilgis svyruoja nuo 210 iki  $450 \mu\text{m}$ , o vidutinis granulės ilgis, gautas išmatavas daugiau nei 100 granulių, yra apie  $329 \mu\text{m}$ . 2GR Granulių paviršius sudarytas iš susipynusių strypelio pavidalo kristalų (žiūrēti 14c ir 14d paveikslus), kuriuos formuoja smulkūs dalelių aglomeratai. Didelio didinimo SEM nuotraukoje (žiūrēti 14e paveikslą) aiškiai matyti, kad 2GR granulės susideda iš vienalyčių, romboedrinių, Mg-WH būdingos formos dalelių, kas papildomai patvirtina, jog mèginys yra vienfazis ir neturi jokių kitų kristalinių intarpų ar priemaišų. Mèginyje yra mažų dalelių, kurių vidutinis dydis yra maždaug 70 nm, žymiai didesnis nei kristalito dydis, nustatytas pagal XRD duomenis. Kiekviena dalelė, matoma SEM, sudaryta iš daugybės daug mažesnių kristalitų. Norint atlikti išsamų granulės vidinės struktūros SEM tyrimą, 2GR mèginys buvo perskeltas (žiūrēti 14f paveikslą). Granulės vidaus SEM nuotraukoje matyti romboedrinių, monodispersinių, maždaug 90 nm dydžio dalelių, forma atitinkančią tas, kurios aptiktos granulių paviršiuje. Skerspjūvio vaizdas atskleidžia tolygią granulių sudėtį visame tūryje, patvirtindamas sėkmingą sintezės procesą.



**14 pav.** Pradinių GYP ir 2GR granulių SEM nuotraukos: (a) GYP granulė; (b) 2GR granulės kartu su jų ilgio pasiskirstymo histograma; (c), (d), (e) 2GR mēgino skirtinį didinimų nuotraukos; (f) 2GR granulės skerspjūvis, atskleidžiantis granulės vidinę struktūrą.

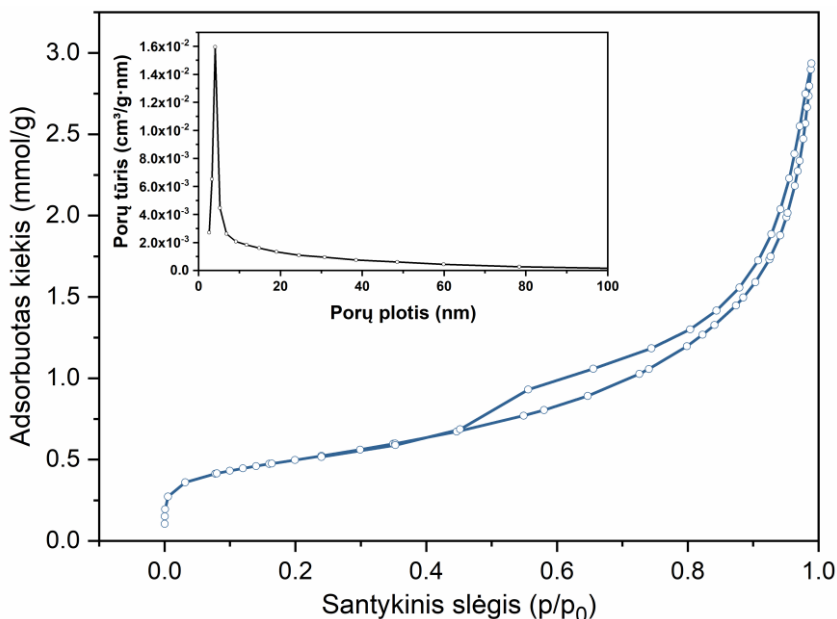
Tirpinimo-nusodinimo reakcija prasideda nuo granulės paviršiaus ir vyksta link jos vidaus. Dėl geresnio reagentų pasiekiamumo pirmiausia intensyviausias nusėdimas vyksta paviršiuje, kur susiformuoja daug smulkų grūdelių. Tuo pačiu metu vidinėje granulės dalyje reakcija vyksta lėčiau, sudarydama palankias sąlygas selektyviam didesnių kristalų formavimuisi. Dėl šio augimo mechanizmo SEM nuotraukose stebimas Mg-WH kristalų dydžio skirtumas granulės viduje ir išorėje. Šis reiškinys gali būti siejamas su Ostwaldo brendimu - procesu, kai mažesnės dalelės ištirpsta, o didesnės ilgainiui auga. Ši dinamiška tirpimo ir nuosėdų susidarymo procesų sąveika įtakoja kristalų dydžio pasiskirstymą granulėje.

Susintetintų 1GR ir 3GR mēginių paviršiaus morfologija buvo tirta SEM metodu (žiūrėti 15 paveikslą). Atliktas granulių paviršiaus ir skerspjūvio tyrimas atskleidė reikšmingus skirtumus tarp šių dviejų mēginių. 1GR granulės suformuotos iš lygaus paviršiaus, netaisyklingos formos tūrių kristalų (15 paveiksllo a–d), tuo tarpu 3GR mēgino paviršiuje matyti romboedriniai Mg-WH kristalai, kurių dydis svyruoja nuo maždaug 100 iki 250 nm (žiūrėti 15 e–h). Be to, šiame mēginyje matyti debeselių formos dalelių aglomeratai, priskirti CDHA fazei. Morfologiškai skirtinį dalelių susidarymas koreliuoja su bifaze 3GR granulių sudėtimi, anksčiau nustatyta XRD, FT-IR tyrimų metu.



**15 pav.** 1GR ir 3GR granulių SEM vaizdai: (a), (b) ir (c) 1GR mèginio skirtinę didinimą vaizdai; (d) 1GR granulés skerspjūvis; (e), (f), (g) 3GR mèginio skirtinę didinimą vaizdai; (h) 3GR granulés skerspjūvis.

1GR–3GR mèginiai paviršiaus savybëms įvertinti buvo atliki N<sub>2</sub> adsorbcijos-desorbcijos matavimai (16 paveiksle pateiktos 2GR mèginio N<sub>2</sub> adsorbcijos-desorbcijos bei porų dydžių pasiskirstymo kreivës).



**16 pav.** 2 GR mèginio N<sub>2</sub> adsorbcijos-desorbcijos bei porų dydžių pasiskirstymo kreivës.

Esant žemam santykiniam slėgiui, adsorbcijos izoterma yra įdubusi p/p<sub>0</sub> ašies atžvilgiu, o tai rodo mikroporų užpildymą, pereinanti į pusiau linijinį segmentą vidurinėje atkarpoje ir sparčiai didėjanti iki p/p<sub>0</sub> artėja prie 1. Kadangi adsorbcijos sotis taip ir nebuvo pasiekta, tai siejama su makroporų buvimu. Be to mėginyje yra ir mezoporų, nes aiškiai matomas ryškėjantis siauras tarpas tarp N<sub>2</sub> adsorbcijos ir desorbcijos kreivią, atsirandantis mažinant slėgi. Šie stebėjimai aiškiai patvirtina, kad analizuojamame mėginyje yra įvairių porų dydžių: tam tikras mikroporų ir makroporų kiekis, dominuojant mezoporoms. N<sub>2</sub> adsorbcijos ir desorbcijos kreivės atitinka mišrų II ir IV izotermų tipą su H3 tipo histerezės kilpa. Kaip jau minėta, neporėtiems ir makroporiams adsorbentams būdingos II tipo izotermos, mezoporių adsorbentų N<sub>2</sub> adsorbcijos ir desorbcijos kreivės priskiriamos IV tipui, o H3 tipo histerezės kilpas formuoja nestandžių plokščių dalelių agregatai, sudarantys plyšio formos poras, kurios, mūsų atveju, gali atsirasti dėl Mg-WH dalelių sankaupų arba dėl makroporų sudaryto porų tinklo mėginyje buvimo. 16 paveikslėlyje intarpas vaizduoja porų dydžio pasiskirstymą 2GR mėginyje, apskaičiuotą iš desorbcijos kreivės, naudojant Barrett-Joyner-Halenda (BJH) metodą. Mėginio porų dydžio pasiskirstymas yra gana platus, o vyraujantį smailė (viršūnė ties 4,1 nm) žymi mezoporas.

1 lentelėje pateikti 1GR-3GR pavyzdžių S<sub>BET</sub>, mikroporų tūris (V<sub>μ</sub>) ir bendras porų tūris (V<sub>p</sub>) dydžiai. Pažymétina, kad 2GR granulės, sudarytos iš Mg-WH fazės, pasižymi gerokai didesniu S<sub>BET</sub>, palyginti su milteliais (S<sub>BET</sub>=10 m<sup>2</sup>/g). Didesnis S<sub>BET</sub> suteikia keletą privalumų, išskaitant didesnį reaktingumą ir implantavus tokią granulę – geresnę sąveiką su biologiniais audiniais, o tai gali lemti geresnę granulės integraciją ir geresnius gjimo rezultatus. 2GR pavyzdžio V<sub>μ</sub> ir V<sub>p</sub> vertės didžiausios iš visų tirtų medžiagų, o mikroporų tūrio indėlis į bendrą šio bandinio porėtumą yra minimalus.

**1 lentelė.** 1GR–3GR mėginių S<sub>BET</sub>, V<sub>μ</sub> ir V<sub>p</sub>, nustatyti iš N<sub>2</sub> adsorbcijos-desorbcijos matavimų.

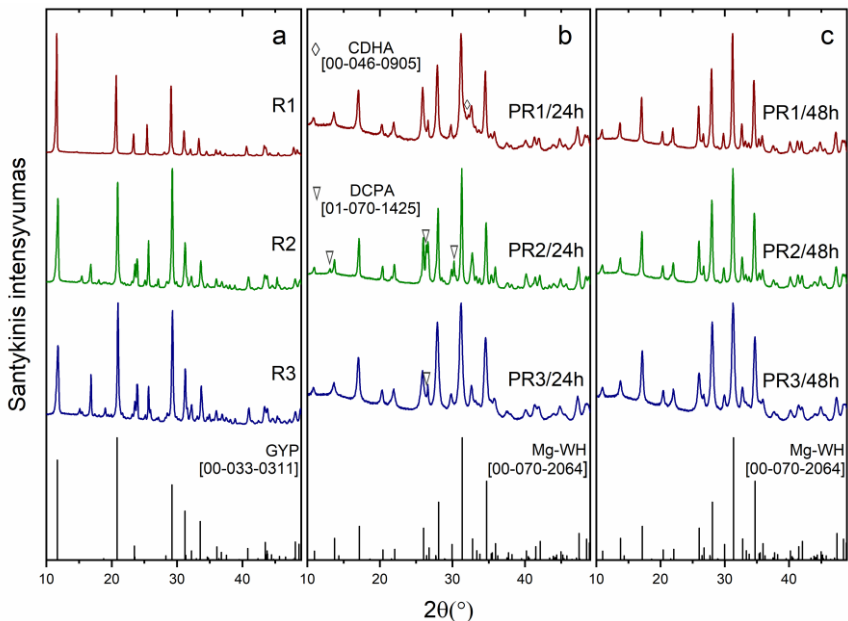
Mėginys	1GR	2GR	3GR
S <sub>BET</sub> (m <sup>2</sup> /g)	3	40	25
V <sub>μ</sub> (cm <sup>3</sup> /g)	0,0017	0,0026	0,0019
V <sub>p</sub> (cm <sup>3</sup> /g)	< nei 0,010	0,095	0,073

Buvo atlikti matavimai Mg-WH antibakterinio veiksmingumo įvertinimui, nes mūsų žiniomis, antibakterinės Mg-WH savybės anksčiau nebuvo ištirtos. 2GR mėginys nebuvo baktericidinis dviem įprastoms bakterijų rūšims: *E. coli* (gramneigama bakterija) arba *S. aureus* (gramteigama bakterija). Abi

bakterijos išliko gyvybingos ir augo ant Luria Bertani agaro, veikiant cheminėmis suspensijomis, net kai jų koncentracija siekė 1000 mg/l. Antibakterinis poveikis nepasireiškė nei po 2 valandų, nei po 24 valandų. Palyginimui, ZnSO<sub>4</sub> buvo baktericidinis *E. coli* esant 1000 mg Zn/l ir *S. aureus* - 10 mg Zn/l po 24 valandų poveikio.

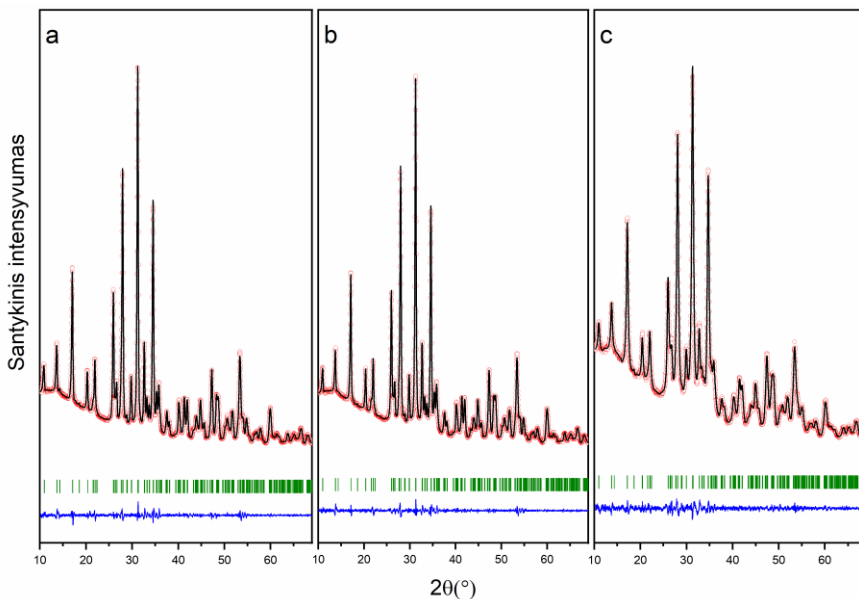
### 3.3. Skirtingos morfologinės sudėties magnio vitlokito granulių sintezė iš skirtinės sudėties pradinių granulių

17(a–c) paveiksluose pateiktos susintetintų R1–R3, PR1/24h–PR3/24h ir PR1/48h–PR3/48h granulių XRD. Iš 17a paveiksle pavaizduotų XRD matyti, kad vieninėse R1 granulėse, gautose iš kalcio sulfato (CS) ir vandens, mišriose R2 granulėse, papildomai naudojant (NH<sub>4</sub>)<sub>2</sub>HPO<sub>4</sub>, bei R3 granulėse su MgHPO<sub>4</sub>·3H<sub>2</sub>O, dominuoja GYP fazė. Tai patvirtina, kad pirmako CS milteliai sintezės metu vandeninėje aplinkoje hidratavosi, susidarant GYP produktui. Augant ir susijungiant kristalams, birūs milteliai sukietėjo į vientisą bloką, iš kurio vėliau buvo suformuotos granulės. 17b paveiksle pateiktos PR1/24h, PR2/24h ir PR3/24h granulių XRD difraktogramos, atitinkamai gautos iš vieninių R1 granulių ir mišrių R2 bei R3 granulių, kartu su standartine Mg-WH difraktograma. Gauti rezultatai atskleidė bifazių produktų susidarymą: PR1/24h sudarė Mg-WH ir CDHA fazės, o PR2/24h ir PR3/24h - Mg-WH ir DCPA fazės. PR2/24h mėginyje DCPA kiekis buvo žymiai didesnis nei PR3/24h. CDHA fazė dažniausiai susiformuoja, esant aukštesnėms pH reikšmėms, o Mg-WH - vidutiniškai žemose pH terpėse. Tačiau šiame tyrime visos sintezės buvo atliktos beveik vienodomis pH sąlygomis, o tai rodo, kad CDHA susidarimą mėginyje nulėmė Ca/Mg santykis reakcijos tirpale. DCPA fazės buvimas PR2/24h ir PR3/24h mėginiuose rodo, kad Mg-WH, minėtujų mėginių sintezės sąlygomis, susidaro palaipsniui per tarpinę DCPA fazę. Ši virsmą skatina pakankamas magnio kiekis ir vidutiniškai rūgštus pH reakcijos tirpale. Šie eksperimentiniai rezultatai leidžia teigti, kad reakcijos laikas, pirmakų ir tirpalų sudėties daro reikšmingą įtaką galutinio produkto sudėčiai. Priešingai, po 48 val. susintetintų granulių (PR1/48h, PR2/48h ir PR3/48h) XRD analizė atskleidė vienfazių medžiagų susidarymą (žiūrėti 17c paveikslą).



**17 pav.** Tirpimo-nusodinimo metodu susintetintų R1–R3 (a), PR1/24h–PR3/24h (b) ir PR1/48h–PR3/48h (c) granulių XRD. Difraktogramų smailės identikuotos pagal standartines GYP, CDHA, DCPA ir Mg-WH fazių korteles.

Siekiant nustatyti susintetintų vienfazių PR1/48h–PR3/48h mėginių struktūrinius parametrus, buvo atliktas XRD duomenų patikslinimas, naudojant Le Bail metodą. Granulių XRD difraktogramos kartu su Le Bail tikslinimo difraktogramos kontūru pateiktos 18 paveiksle. Rezultatai parodė puikią koreliaciją tarp išmatuoto XRD profilio (raudoni apskritimai) ir apskaičiuoto profilio (juoda linija), kurie atitinka Brego padėtis (žali brūkšneliai). 2 lentelėje pateikti Mg-WH fazių, susintetintų po 48 val. iš įvairios sudėties pradinių granulių, struktūriniai parametrai. Gautų produktų struktūriniai rodikliai buvo tarpusavyje panašūs ir gerai atitiko mokslinėje literatūroje skelbiamus rezultatus.



**18 pav.** PR1/48h (a), PR2/48h (b), and PR3/48h (c) granulių XRD difraktogramos su Le Bail tikslinimo kontūru (raudoni apkritimai nurodo eksperimentinius duomenis; ištisinė juoda linija žymi patikslintus duomenis; mėlyna linija vaizduoja skirtumą tarp eksperimentinių ir patikslintų duomenų; žalios spalvos vertikalūs brūkšneliai nurodo Brego padėtis).

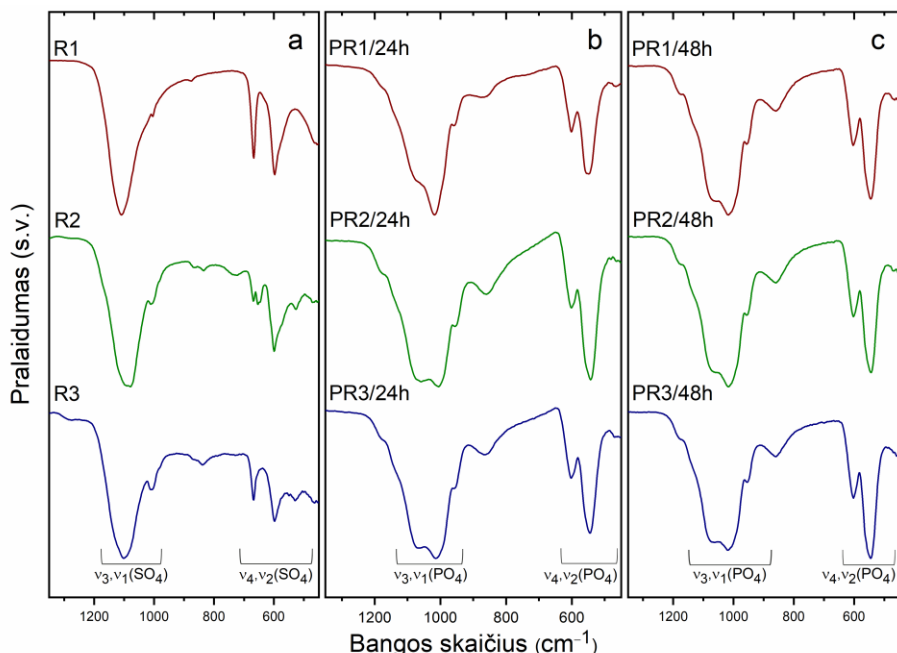
**2 lentelė.** Struktūriniai PR1/48h, PR2/48h, and PR3/48h granulių parametrai.

Méginių	PR1/48h	PR2/48h	PR3/48h
a, Å	10,38042(44)	10,36717(46)	10,33965(92)
c, Å	37,1445(17)	37,1087(17)	37,1038(35)
Gardelės tūris, Å <sup>3</sup>	3466,21(26)	3454,04(27)	3435,27(54)
R <sub>p</sub>	2,01	1,82	1,72
R <sub>wp</sub>	2,68	2,38	2,19
χ <sup>2</sup>	1,74	1,39	1,19
Kristalitų dydis, nm	46	52	17

Siekiant identifikuoti funkcinės grupės granulėse, buvo atlikta jų FT-IR analizė. 19(a–c) paveiksle pavaizduoti įvairiomis sąlygomis gautų produktų FT-IR spektrai. R1–R3 pirmtako granulių FT-IR spektruose yra matomos vibracijos juostos ties  $1110\text{ cm}^{-1}$ ,  $669\text{ cm}^{-1}$  ir  $598\text{ cm}^{-1}$ , kurios priskiriamos  $\text{SO}_4^{2-}$  jono tempimo ir lenkimo virpesiams (žiūrėti 19a paveikslą). Silpna absorbcijos juosta ties  $869\text{ cm}^{-1}$  priskiriamą vandenilio fosfato ( $\text{P–O(H)}$ )

grupei, atsirandančiai dėl pirmtakų druskose ( $(\text{NH}_4)_2\text{HPO}_4$  ir  $\text{MgHPO}_4 \cdot 3\text{H}_2\text{O}$ ) esančios P–O(H) grupės absorbcijos.

Granulių PR1/24h–PR3/24h FT-IR spektruose matomos  $\text{PO}_4^{3-}$  ir  $\text{HPO}_4^{2-}$  funkcinių grupių absorbcijos juostos (žiūrėti 19b paveikslą). Su  $\text{SO}_4^{2-}$  grupe susijusių vibracijos smailių išnykimas rodo, kad sulfatų turintys pirmtakai visiškai ištirpo ir per 24 val. sintezės procesą virto CaP medžiagomis. Šiuos rezultatus patvirtina XRD analizė, kurios metu nustatytos šios CaP fazės: PR1/24h mėginyje buvo CDHA ir Mg-WH, PR2/24h ir PR3/24h mėginiuose – DCPA ir Mg-WH fazės (žiūrėti 19b paveikslą). Stebimos absorbcijos juostos ties  $1180 \text{ cm}^{-1}$ ,  $1065 \text{ cm}^{-1}$ ,  $1011 \text{ cm}^{-1}$  ir  $954 \text{ cm}^{-1}$  priskiriamos P–O ir P–O(H) tempimo virpesiams, susijusiomis su  $\text{PO}_4^{3-}$  ir  $\text{HPO}_4^{2-}$  grupėmis, esančiomis CDHA, DCPA ir Mg-WH fazių kristalinėse struktūrose.

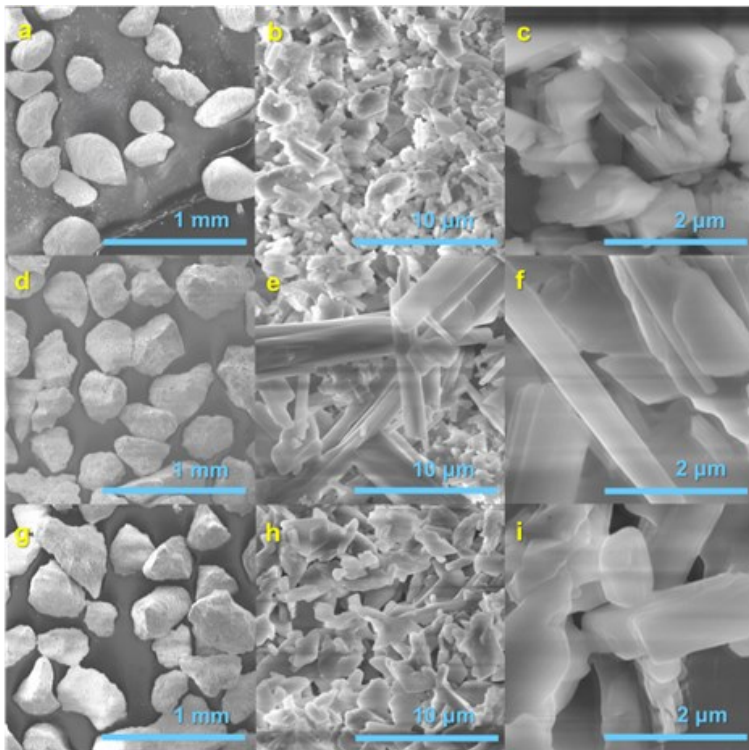


**19 pav.** Tirpimo-nusodinimo metodui susintetintų R1–R3 (a), PR1/24h–PR3/24h (b) ir PR1/48h–PR3/48h (c) granulių FT-IR spektras.

Mėginių PR1/24h ir PR2/24h virpesių juostų ties  $1065 \text{ cm}^{-1}$  intensyvumo skirtumai padeda nustatyti fasinę sudėtį. PR1/24h atveju, kurį sudaro CDHA kartu su Mg-WH faze, padidėjęs  $1065 \text{ cm}^{-1}$  juostos intensyvumas gali būti siejamas su CDHA faze, nes ji nepasižymi ryškia absorbcija ties šiuo bangos skaičiumi. Priešingai,  $1065 \text{ cm}^{-1}$  absorbcijos juosta yra ryški PR2/24h mėginyje ir vos pastebima PR3/24h mėginyje, kuri atitinka DCPA fazei

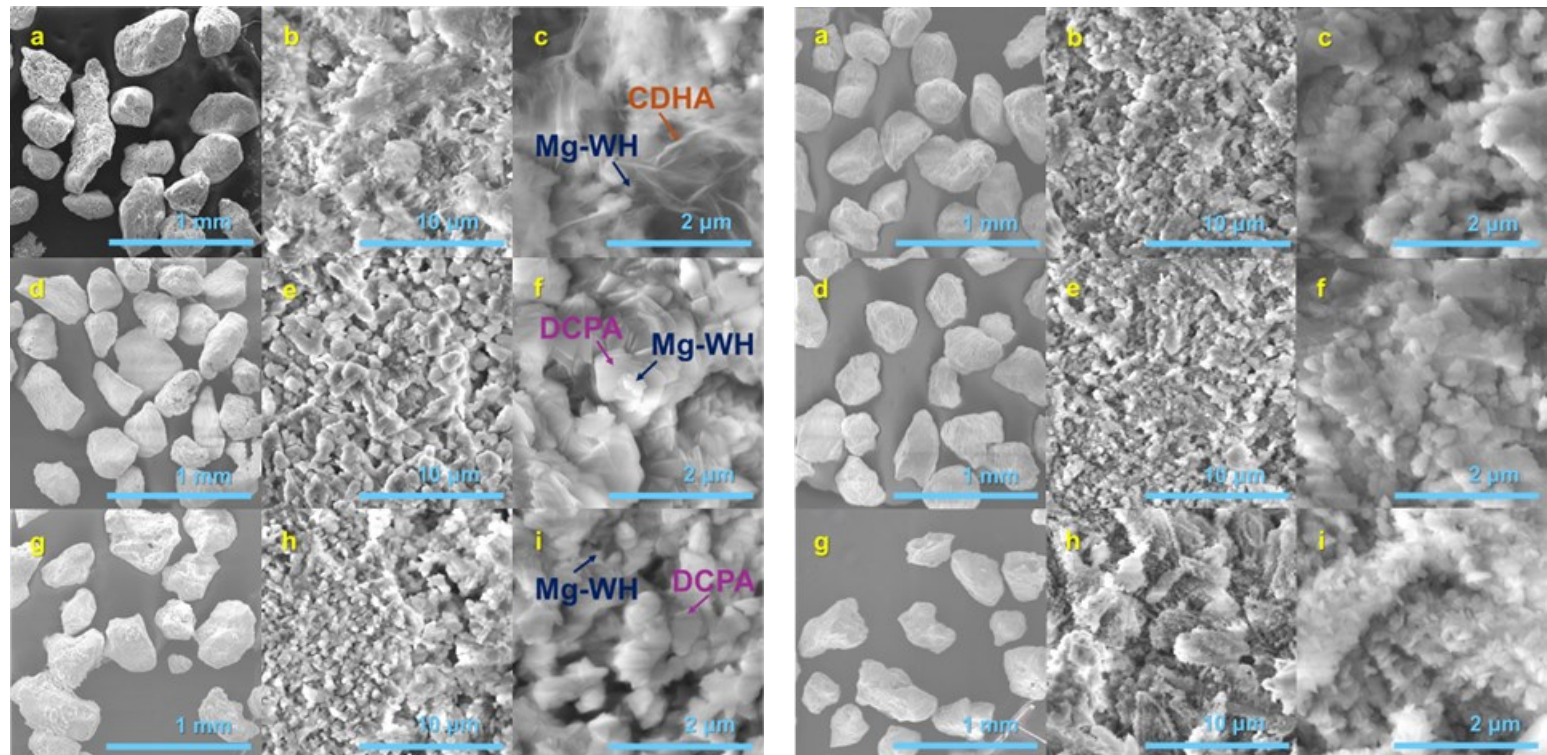
būdingą P–O tempimo vibraciją ir dėl šios sugerties juostos intensyvumas yra mažesnis. Be to, PR1/24h ir PR2/24h mèginiuose yra gana plati sugerties juosta, kurios maksimumas yra ties  $863\text{ cm}^{-1}$ , priskiriama P–O(H) jungties tempimo vibracijai. Šios juostos išplatėjimas rodo, kad vandenilio fosfato jonai egzistuoja dviejose skirtingose kristalografinėse aplinkose – galimai dviejose skirtingose CaP fazėse. Sugerties juostos ties  $601\text{ cm}^{-1}$ ,  $545\text{ cm}^{-1}$  ir  $465\text{ cm}^{-1}$  siejamos su Mg-WH faze ir atitinka P–O ir O–P–O jungčių lenkimo modas. PR1/24h mèginio atveju juosta ties  $545\text{ cm}^{-1}$  šiek tiek išplatėja dėl CDHA buvimo ir spektrinė juosta pasistumia ties  $560\text{ cm}^{-1}$ . PR1/48h–PR3/48h granulių FT-IR spektruose matomos vibracijos juostos ties  $1180\text{ cm}^{-1}$ ,  $1065\text{ cm}^{-1}$ ,  $1011\text{ cm}^{-1}$ ,  $954\text{ cm}^{-1}$ ,  $865\text{ cm}^{-1}$  ir  $600$ – $460\text{ cm}^{-1}$  (žiūrėti 19c paveikslą). Šios juostos priskiriamas  $\text{PO}_4^{3-}$  ir  $\text{HPO}_4^{2-}$  grupių P–O ir P–O(H) tempimo ir deformacijos vibracijoms, būdingoms Mg-WH fazės kristalinei struktūrai.

20, 21 ir 22 paveiksluose pateiktos susintetintų pirmtako R1–R3, produktų PR1/24h–PR3/24h ir PR1/48h–PR3/48h granulių SEM nuotraukos.  $200$ – $400\text{ }\mu\text{m}$  dydžio pradinių granulių su šiurkščiais kraštais paviršių sudaro strypų formos kristalai, būdingi GYP (žiūrėti 20a, b, d, e, g, h paveikslus). Didesnio didinimo vaizduose matyti, kad granules sudaro atsitiktinai išsidėstę plokštelės formos kristalai (žiūrėti 20c, f, i paveikslus). PR1/24h–PR3/24h netaisyklingos formos granulių paviršiaus morfologija pasižymi pastebima įvairove, kurią lemia tiek pirmtako granulių sudėtis, tiek sintezės metu naudojamos reakcijos tirpalo skirtumai (žiūrėti 21a, b, d, e, g, h paveikslus).



**20 pav.** Pirmtako R1 (a–c), R2 (d–f) ir R3 (g–i) granulių SEM nuotraukos.

Produktų PR1/48h–PR3/48h granulių paviršių sudaro susipynusios sferinės ir strypo formos dalelės, suformuotos iš smulkųjų kristalų (žiūrėti 22a, b, d, e, g, h paveikslus). Didesnio didinimo SEM mikrografijose Mg-WH paviršiuje pastebimi romboedriniai kristalitų aglomeratai, kurių vidutinis dydis yra maždaug 150–200 nm (žiūrėti 22c ir f paveikslus). 22i paveiksle matyti, kad PR3/48h mėginys pasižymi tankia porėta mikrostruktūra, kurią sudaro maždaug 200 nm skersmens plokšteliinių kristalų sankupos.



**21 pav.** Granulių PR1/24h (a-c), PR2/24h (d-f) ir PR3/24h (g-i), gautų tirpinimo-nusodinimo metodu po 24 val. sintezės, SEM nuotraukos.

**22 pav.** Granulių PR1/48h (a-c), PR2/48h (d-f) ir PR3/48h (g-i), gautų tirpinimo-nusodinimo metodu po 48 val. sintezės, SEM nuotraukos.

PR1/24h, PR2/24h, PR3/24h, PR1/48h, PR2/48h ir PR3/48h mėginių paviršiaus savybių tyrimas, atliktas naudojant N<sub>2</sub> adsorbcijos-desorbcijos matavimus, atskleidė reikšmingus paviršiaus ploto ir porėtumo skirtumus (žiūrėti 3 lentelę).

**3 lentelė.** Duomenys, gauti iš N<sub>2</sub> adsorbcijos-desorbcijos matavimų: S<sub>BET</sub>, S<sub>ext</sub> (išorinis paviršiaus plotas), V<sub>μ</sub>, and V<sub>p</sub> visų susintetintų produktų mėginių.

Mėginys	PR1/24h	PR2/24h	PR3/24h	PR1/48h	PR2/48h	PR3/48h
S <sub>BET</sub> (m <sup>2</sup> /g)	35	4	30	9	11	38
S <sub>ext</sub> (m <sup>2</sup> /g)	30	3	27	7	8	35
V <sub>μ</sub> (cm <sup>3</sup> /g)	0,0020	0,00050	0,0013	0,0011	0,0012	0,0011
V <sub>p</sub> (cm <sup>3</sup> /g)	0,13	0,010	0,069	0,025	0,027	0,077

Bifazis PR1/24h produktas, sudarytas iš Mg-WH ir CDHA, pasižymi didžiausiu BET paviršiaus plotu (35 m<sup>2</sup>/g) ir bendru porų tūriu (0,13 cm<sup>3</sup>/g). Priešingai, PR2/24h, sudarytas iš Mg-WH ir reikšmingo kieko DCPA, turi daug mažesnį paviršiaus plotą (4 m<sup>2</sup>/g) ir porų tūri (0,010 cm<sup>3</sup>/g), kas atspindi tankesnę jo paviršiaus mikrostruktūrą. PR3/24h, kuriame vyrauja Mg-WH ir tik nedidelis kiekis DCPA, pasižymi tarpinėmis savybėmis – santykinai dideliu paviršiaus plotu (30 m<sup>2</sup>/g) ir vidutiniu porėtumu (0,069 cm<sup>3</sup>/g). Vienfazės PR1/48h, PR2/48h ir PR3/48h Mg-WH granulės pasižymi ryškiais paviršiaus savybių skirtumais, atsirandančiais dėl skirtinės pirmtakų granulių cheminės sudėties ir sintezės sąlygų. PR3/48h pasižymėjo gerokai didesniu BET paviršiaus plotu (38 m<sup>2</sup>/g), palyginti su PR1/48h (9 m<sup>2</sup>/g) ir PR2/48h (11 m<sup>2</sup>/g). Mėginių PR1/48h, PR2/48h ir PR3/48h S<sub>ext</sub> vertės atitinkamai yra 7 m<sup>2</sup>/g, 8 m<sup>2</sup>/g ir 35 m<sup>2</sup>/g ir gerai koreliuoja su jų specifiniais paviršiaus plotais, kas rodo, kad didžioji paviršiaus ploto dalis yra granulės išorėje. Mikroporos atitinkamai sudaro tik 12 %, 17 % ir 8 % viso šių mėginių paviršiaus ploto, todėl akivaizdu, kad juose dominuoja mezoporos. Vienodi mikroporų tūriai visuose mėginiuose (V<sub>μ</sub> ≈ 0,0011–0,0012 cm<sup>3</sup>/g) papildomai patvirtina, kad medžiagoje vyrauja mezoporos. Mėginių taip pat labai skiriasi bendru porų tūriu: PR1/48h V<sub>p</sub> yra 0,025 cm<sup>3</sup>/g, PR2/48h – 0,027 cm<sup>3</sup>/g, o PR3/48h – 0,077 cm<sup>3</sup>/g. Žymiai didesnis PR3/48h porų tūris atskleidžia produkto palyginti labiau pasiekiamą paviršių ir gali būti susijusi su granulių paviršių sudarančiu dalelių dydžiu. Priešingai, PR1/48h ir PR2/48h pasižymi daug tankesnėmis paviršiaus mikrostruktūromis, kurioms būdingas mažesnis paviršiaus plotas ir porų tūris.

## 4. IŠVADOS

1. Paprastas, ekonomiškas ir aplinkai draugiškas tirpinimo-nusodinimo metodas leido vienos sintezės metu gauti didelį kiekį Mg-WH miltelių (3,00 g; 89 % išeiga). Mg-WH susidarymas buvo valdomas keičiant reakcijos trukmę, o XRD analizė atskleidė fazinį virsmą iš tarpinės DCPA į galutinę Mg-WH fazę per 72 sintezės valandas. Apskaičiuota, kad Mg-WH miltelių vidutinis kristalitų dydis siekė 34 nm, o kristališkumo laipsnis 78 %. FT-IR analizė patvirtino fosfatinį ( $\text{PO}_4^{3-}$  ir  $\text{HPO}_4^{2-}$ ) grupių buvimą Mg-WH struktūroje. SEM-EDX analizė atskleidė, kad susiformavo romboedriniai Mg-WH kristalai, kurių dydis siekė apie 75–150 nm, o Ca, Mg, P ir O elementai buvo tolygiai pasiskirstę mėginyje. Mg-WH mėginio  $\text{SBET}$  siekė  $10 \text{ m}^2/\text{g}$ .
2. Tirpinimo-nusodinimo sintezės metodu iš pradinių gipso granulių vienos sintezės metu buvo gauta 1,75 g Mg-WH granulių, naudojant 3,00 g pirmtako. Įvertinus pH įtaką produkto sudėčiai, nustatyta, kad grynas Mg-WH susidaro esant pH 6,2, o fazės grynumą patvirtino XRD, Le Bail struktūros patikslinimas ir FT-IR spektroskopija. Susintetintų Mg-WH granulių kristališkumo laipsnis siekė 60 %. SEM analizė atskleidė, kad granulių vidutinis dydis buvo apie 329  $\mu\text{m}$ , o jos sudarytos iš romboedrinių dalelių, kurių vidutinis dydis siekė apie 70 nm. BET analizė parodė, kad Mg-WH granulėse vyrauja mezoporos, o jų  $\text{SBET}$  lygus  $40 \text{ m}^2/\text{g}$ . XRD ir Rietveldo struktūros patikslinimas patvirtino bifazio mėginio, susidedančio iš 37 masės % Mg-WH ir 63 masės % CDHA fazės susidarymą esant reakcijos pH 6,7. Svarbus optimizuoto sintezės metodo privalumas yra galimybė gauti vienfazes arba bifazes medžiagas.
3. Mg-WH granulės buvo pagamintos, naudojant tirpimo-nusodinimo metodą iš trijų skirtingų pradinių granulių, susidedančių iš skirtingų kiekių diamonio vandenilio fosfato, magnio vandenilio fosfato ir gipso. Buvo tirta reakcijos trukmės įtaka produkto sudėčiai, morfologijai ir paviršiaus savybėms. XRD analizės rezultatai parodė, kad bifazės granulės (Mg-WH su CDHA arba Mg-WH su DCPA) susidarė po 24 valandų, o vienfazės Mg-WH granulės buvo gautos po 48 sintezės valandų. FT-IR analizė patvirtino, kad tarpiniuose produktuose yra Mg-WH, CDHA ir DCPA būdingų funkinių grupių, tačiau galutinėse Mg-WH granulėse šios grupės jau nebuvę aptiktos. SEM analizė atskleidė, kad pradinių ir produktų granulių morfologija akivaizdžiai skiriasi, pastarujujų paviršius suformuotas iš susipynusių sferinių ir strypelių formos aglomeratų, sudarytų iš smulkių Mg-WH kristalų, kurių vidutinis dydis siekė apie 150–200 nm. Tyrimas atskleidė, kad Mg-WH granulių paviršiaus plotas ir porėtumas priklauso nuo pradinių medžiagų sudėties ir sintezės trukmės.

## REFERENCES

- [1] J. Lu, H. Yu, C. Chen, Biological properties of calcium phosphate biomaterials for bone repair: a review, *RSC Adv.* 8 (2018) 2015–2033. <https://doi.org/10.1039/C7RA11278E>.
- [2] E. García-Gareta, M.J. Coathup, G.W. Blunn, Osteoinduction of bone grafting materials for bone repair and regeneration, *Bone* 81 (2015) 112–121. <https://doi.org/10.1016/J.BONE.2015.07.007>.
- [3] X. Hou, L. Zhang, Z. Zhou, X. Luo, T. Wang, X. Zhao, B. Lu, F. Chen, L. Zheng, Calcium Phosphate-Based Biomaterials for Bone Repair, *J. Funct. Biomater.* 13 (2022) 187. <https://doi.org/10.3390/JFB13040187>.
- [4] P. Wang, L. Zhao, J. Liu, M.D. Weir, X. Zhou, H.H.K. Xu, Bone tissue engineering via nanostructured calcium phosphate biomaterials and stem cells, *Bone Res.* 2 (2014) 1–13. <https://doi.org/10.1038/boneres.2014.17>.
- [5] M.E. Bussell, Improving bone health: addressing the burden through an integrated approach, *Aging Clin. Exp. Res.* 33 (2021) 2777–2786. <https://doi.org/10.1007/s40520-021-01971-3>.
- [6] T. Mastnak, U. Maver, M. Finšgar, Addressing the Needs of the Rapidly Aging Society through the Development of Multifunctional Bioactive Coatings for Orthopedic Applications, *Int. J. Mol. Sci.* 23 (2022) 2786. <https://doi.org/10.3390/IJMS23052786>.
- [7] M. Sari, P. Hening, Chotimah, I.D. Ana, Y. Yusuf, Porous structure of bioceramics carbonated hydroxyapatite-based honeycomb scaffold for bone tissue engineering, *Mater. Today Commun.* 26 (2021) 102135. <https://doi.org/10.1016/J.MTCOMM.2021.102135>.
- [8] Y. Li, S.K. Chen, L. Li, L. Qin, X.L. Wang, Y.X. Lai, Bone defect animal models for testing efficacy of bone substitute biomaterials, *J. Orthop. Transl.* 3 (2015) 95–104. <https://doi.org/10.1016/J.JOT.2015.05.002>.
- [9] L. Zhang, G. Yang, B.N. Johnson, X. Jia, Three-dimensional (3D) printed scaffold and material selection for bone repair, *Acta Biomater.* 84 (2019) 16–33. <https://doi.org/10.1016/J.ACTBIO.2018.11.039>.
- [10] T. Lu, X. Yuan, L. Zhang, F. He, X. Wang, Y. Zhang, J. Ye, High throughput synthesis and screening of zinc-doped biphasic calcium phosphate for bone regeneration, *Appl. Mater. Today* 25 (2021) 101225. <https://doi.org/10.1016/J.APMT.2021.101225>.
- [11] L. Huang, B. Zhou, H. Wu, L. Zheng, J. Zhao, Effect of apatite formation of biphasic calcium phosphate ceramic (BCP) on

- osteoblastogenesis using simulated body fluid (SBF) with or without bovine serum albumin (BSA), *Mater. Sci. Eng. C* 70 (2017) 955–961. <https://doi.org/10.1016/J.MSEC.2016.05.115>.
- [12] W. Zhi, X. Wang, D. Sun, T. Chen, B. Yuan, X. Li, X. Chen, J. Wang, Z. Xie, X. Zhu, K. Zhang, X. Zhang, Optimal regenerative repair of large segmental bone defect in a goat model with osteoinductive calcium phosphate bioceramic implants, *Bioact. Mater.* 11 (2022) 240–253. <https://doi.org/10.1016/J.BIOACTMAT.2021.09.024>.
- [13] S. Jiang, T. Liu, G. Wu, W. Li, X. Feng, J.L. Pathak, J. Shi, BMP2-Functionalized Biomimetic Calcium Phosphate Graft Promotes Alveolar Defect Healing During Orthodontic Tooth Movement in Beagle Dogs, *Front. Bioeng. Biotechnol.* 8 (2020) 539849. <https://doi.org/10.3389/FBIOE.2020.00517/BIBTEX>.
- [14] C.Y. Kei Lung, A.S. Khan, R. Zeeshan, S. Akhtar, A.A. Chaudhry, J.P. Matinlinna, An antibacterial porous calcium phosphate bilayer functional coatings on titanium dental implants, *Ceram. Int.* 49 (2023) 2401–2409. <https://doi.org/10.1016/J.CERAMINT.2022.09.213>.
- [15] A.Y. Cai, Y.J. Zhu, C. Qi, Biodegradable Inorganic Nanostructured Biomaterials for Drug Delivery, *Adv. Mater. Interfaces* 7 (2020) 2000819. <https://doi.org/10.1002/ADMI.202000819>.
- [16] J. Jeong, J.H. Kim, J.H. Shim, N.S. Hwang, C.Y. Heo, Bioactive calcium phosphate materials and applications in bone regeneration, *Biomater. Res.* 23 (2019) 1–11. <https://doi.org/10.1186/S40824-018-0149-3>.
- [17] X. Wang, Y. Yu, L. Ji, Z. Geng, J. Wang, C. Liu, Calcium phosphate-based materials regulate osteoclast-mediated osseointegration, *Bioact. Mater.* 6 (2021) 4517–4530. <https://doi.org/10.1016/J.BIOACTMAT.2021.05.003>.
- [18] K. Ishikawa, Y. Miyamoto, A. Tsuchiya, K. Hayashi, K. Tsuru, G. Ohe, Physical and Histological Comparison of Hydroxyapatite, Carbonate Apatite, and  $\beta$ -Tricalcium Phosphate Bone Substitutes, *Mater.* 11 (2018) 1993. <https://doi.org/10.3390/MA11101993>.
- [19] S. V. Dorozhkin, Multiphasic calcium orthophosphate ( $\text{CaPO}_4$ ) bioceramics and their biomedical applications, *Ceram. Int.* 42 (2016) 6529–6554. <https://doi.org/10.1016/J.CERAMINT.2016.01.062>.
- [20] A. Najafinezhad, M. Abdellahi, S. Saber-Samandari, H. Ghayour, A. Khandan, Hydroxyapatite- M-type strontium hexaferrite: A new composite for hyperthermia applications, *J. Alloys Compd.* 734 (2018) 290–300. <https://doi.org/10.1016/J.JALLOCOM.2017.10.138>.
- [21] A. Talal, S.K. Hamid, M. Khan, A.S. Khan, Structure of biological

- apatite: bone and tooth, Handb. Ion. Substituted Hydroxyapatites (2020) 1–19. <https://doi.org/10.1016/B978-0-08-102834-6.00001-X>.
- [22] C. Wang, K.J. Jeong, H.J. Park, M. Lee, S.C. Ryu, D.Y. Hwang, K.H. Nam, I.H. Han, J. Lee, Synthesis and formation mechanism of bone mineral, whitlockite nanocrystals in tri-solvent system, *J. Colloid Interface Sci.* 569 (2020) 1–11.  
<https://doi.org/10.1016/J.JCIS.2020.02.072>.
- [23] F.A. Shah, Magnesium whitlockite – omnipresent in pathological mineralisation of soft tissues but not a significant inorganic constituent of bone, *Acta Biomater.* 125 (2021) 72–82.  
<https://doi.org/10.1016/J.ACTBIO.2021.02.021>.
- [24] H. Lin Jang, K. Jin, J. Lee, Y. Kim, S. Hoon Nahm, K. Sun Hong, K. Tae Nam, Revisiting Whitlockite, the Second Most Abundant Biomineral in Bone: Nanocrystal Synthesis in Physiologically Relevant Conditions and Biocompatibility Evaluation, *ACS Nano* 8 (2013) 634–641. <https://doi.org/10.1021/nn405246h>.
- [25] L. Wang, Y. Pang, Y. Tang, X. Wang, D. Zhang, X. Zhang, Y. Yu, X. Yang, Q. Cai, A biomimetic piezoelectric scaffold with sustained Mg<sup>2+</sup> release promotes neurogenic and angiogenic differentiation for enhanced bone regeneration, *Bioact. Mater.* 25 (2023) 399–414.  
<https://doi.org/10.1016/J.BIOACTMAT.2022.11.004>.
- [26] L. Bauer, M. Antunović, A. Rogina, M. Ivanković, H. Ivanković, Bone-mimetic porous hydroxyapatite/whitlockite scaffolds: preparation, characterization and interactions with human mesenchymal stem cells, *J. Mater. Sci.* 56 (2021) 3947–3969.  
<https://doi.org/10.1007/s10853-020-05489-3>.
- [27] Y. Yang, H. Wang, H. Yang, Y. Zhao, J. Guo, X. Yin, T. Ma, X. Liu, L. Li, Magnesium-Based Whitlockite Bone Mineral Promotes Neural and Osteogenic Activities, *ACS Biomater. Sci. & Eng.* 6 (2020) 5785–5796. <https://doi.org/10.1021/acsbiomaterials.0c00852>.
- [28] Y. Liu, H. Li, J. Xu, J. TerBush, W. Li, M. Setty, S. Guan, T.D. Nguyen, L. Qin, Y. Zheng, Biodegradable metal-derived magnesium and sodium enhances bone regeneration by angiogenesis aided osteogenesis and regulated biological apatite formation, *Chem. Eng. J.* 410 (2021) 127616. <https://doi.org/10.1016/J.CEJ.2020.127616>.
- [29] H.L. Jang, G. Bin Zheng, J. Park, H.D. Kim, H.R. Baek, H.K. Lee, K. Lee, H.N. Han, C.K. Lee, N.S. Hwang, J.H. Lee, K.T. Nam, In Vitro and In Vivo Evaluation of Whitlockite Biocompatibility: Comparative Study with Hydroxyapatite and β-Tricalcium Phosphate, *Adv. Healthc. Mater.* 5 (2016) 128–136. <https://doi.org/10.1002/ADHM.201400824>.

- [30] V.K. Kaliannagounder, N.P.M.J. Raj, A.R. Unnithan, J. Park, S.S. Park, S.J. Kim, C.H. Park, C.S. Kim, A.R.K. Sasikala, Remotely controlled self-powering electrical stimulators for osteogenic differentiation using bone inspired bioactive piezoelectric whitlockite nanoparticles, *Nano Energy* 85 (2021) 105901.  
<https://doi.org/10.1016/J.NANOEN.2021.105901>.
- [31] A.C. Tas, Preparation of porous apatite granules from calcium phosphate cement, *J. Mater. Sci. Mater. Med.* 19 (2008) 2231–2239.  
<https://doi.org/10.1007/s10856-007-3326-9>.
- [32] K. Akita, N. Fukuda, K. Kamada, K. Kudoh, N. Kurio, K. Tsuru, K. Ishikawa, Y. Miyamoto, Fabrication of porous carbonate apatite granules using microfiber and its histological evaluations in rabbit calvarial bone defects, *J. Biomed. Mater. Res. Part A* 108 (2020) 709–721. <https://doi.org/10.1002/JBM.A.36850>.
- [33] W.B. Lee, C. Wang, J.H. Lee, K.J. Jeong, Y.S. Jang, J.Y. Park, M.H. Ryu, U.K. Kim, J. Lee, D.S. Hwang, Whitlockite Granules on Bone Regeneration in Defect of Rat Calvaria, *ACS Appl. Bio Mater.* 3 (2020) 7762–7768. <https://doi.org/10.1021/acsabm.0c00960>.
- [34] H.L. Jang, H.K. Lee, K. Jin, H.Y. Ahn, H.E. Lee, K.T. Nam, Phase transformation from hydroxyapatite to the secondary bone mineral, whitlockite, *J. Mater. Chem. B* 3 (2015) 1342–1349.  
<https://doi.org/10.1039/C4TB01793E>.
- [35] A. Kizalaite, V. Klimavicius, V. Balevicius, G. Niaura, A.N. Salak, J.C. Yang, S.H. Cho, T. Goto, T. Sekino, A. Zarkov, Dissolution–precipitation synthesis and thermal stability of magnesium whitlockite, *CrystEngComm* 25 (2023) 4370–4379.  
<https://doi.org/10.1039/D3CE00602F>.
- [36] L. Sinusaite, A. Kareiva, A. Zarkov, Thermally Induced Crystallization and Phase Evolution of Amorphous Calcium Phosphate Substituted with Divalent Cations Having Different Sizes, *Cryst. Growth Des.* 21 (2021) 1242–1248.  
<https://doi.org/10.1021/acs.cgd.0c01534>.
- [37] K. Ishikawa, Bone Substitute Fabrication Based on Dissolution–Precipitation Reactions, *Mater.* 2010, 3 (2010) 1138–1155.  
<https://doi.org/10.3390/MA3021138>.
- [38] M.A. Jamilludin, K. Hayashi, Y. Yusuf, K. Ishikawa, Low-crystalline magnesium-doped carbonate apatite/β-tricalcium phosphate granules from sea urchin spine, *J. Am. Ceram. Soc.* 108 (2025) e20498.  
<https://doi.org/10.1111/jace.20498>.
- [39] M.P. Ginebra, M. Espanol, Y. Maazouz, V. Bergez, D. Pastorino,

- Bioceramics and bone healing, EFORT Open Rev. 3 (2018) 173–183.  
<https://doi.org/10.1302/2058-5241.3.170056>.
- [40] A. Fuchs, D. Kreczy, T. Brückner, U. Gbureck, P. Stahlhut, M. Bengel, A. Hoess, B. Nies, J. Bator, U. Klammert, C. Linz, A. Ewald, Bone regeneration capacity of newly developed spherical magnesium phosphate cement granules, Clin. Oral Investig. 26 (2022) 2619–2633.  
<https://doi.org/10.1007/s00784-021-04231-w>.
- [41] M. Sadat-Shojaei, M.T. Khorasani, E. Dinpanah-Khoshdargi, A. Jamshidi, Synthesis methods for nanosized hydroxyapatite with diverse structures, Acta Biomater. 9 (2013) 7591–7621.  
<https://doi.org/10.1016/J.ACTBIO.2013.04.012>.
- [42] C. Du, F.Z. Cui, W. Zhang, Q.L. Feng, X.D. Zhu, K. De Groot, Formation of calcium phosphate/collagen composites through mineralization of collagen matrix, J. Biomed. Mater. Res. 50 (2000) 518-527. [https://doi.org/10.1002/\(SICI\)1097-4636\(20000615\)50:4<518::AID-JBM7>3.0.CO;2-W](https://doi.org/10.1002/(SICI)1097-4636(20000615)50:4<518::AID-JBM7>3.0.CO;2-W).
- [43] V. Šromová, D. Sobola, P. Kaspar, A Brief Review of Bone Cell Function and Importance, Cells 12 (2023) 2576.  
<https://doi.org/10.3390/CELLS12212576>.
- [44] J. An, S. Leeuwenburgh, J. Wolke, J. Jansen, Mineralization processes in hard tissue: Bone, Biominer. Biomater. Fundam. Appl. (2016) 129–146. <https://doi.org/10.1016/B978-1-78242-338-6.00005-3>.
- [45] M.H. Hong, J.H. Lee, H.S. Jung, H. Shin, H. Shin, Biomaterialization of bone tissue: calcium phosphate-based inorganics in collagen fibrillar organic matrices, Biomater. Res. 26 (2022).  
<https://doi.org/10.1186/s40824-022-00288-0>.
- [46] S. Von Euw, Y. Wang, G. Laurent, C. Drouet, F. Babonneau, N. Nassif, T. Azaïs, Bone mineral: new insights into its chemical composition, Sci. Reports 9 (2019) 1–11.  
<https://doi.org/10.1038/s41598-019-44620-6>.
- [47] S. Wu, X. Liu, K.W.K. Yeung, C. Liu, X. Yang, Biomimetic porous scaffolds for bone tissue engineering, Mater. Sci. Eng. R Reports 80 (2014) 1–36. <https://doi.org/10.1016/J.MSER.2014.04.001>.
- [48] J. D. Currey, Bones— Structure and Mechanics, Google knygos, Princeton university press, 2002.  
[https://books.google.lt/books?hl=lt&lr=&id=2jYsJhxiiNWQC&oi=fnd&pg=PP15&dq=bone+structure&ots=1szkQx1GK4&sig=2eMt0WyLIQ\\_xP-I-bzKPnHOzAM&redir\\_esc=y#v=onepage&q=bone+structure&f=false](https://books.google.lt/books?hl=lt&lr=&id=2jYsJhxiiNWQC&oi=fnd&pg=PP15&dq=bone+structure&ots=1szkQx1GK4&sig=2eMt0WyLIQ_xP-I-bzKPnHOzAM&redir_esc=y#v=onepage&q=bone+structure&f=false).
- [49] Y.H. An, R.A. Draughn, Mechanical testing of bone and the bone-

- implant interface, *Mech. Test. Bone Bone-Implant Interface* (1999) 1–625. <https://doi.org/10.1201/9781420073560>.
- [50] S.R. Stock, The Mineral–Collagen Interface in Bone, *Calcif. Tissue Int.* 97 (2015) 262–280. <https://doi.org/10.1007/s00223-015-9984-6>.
- [51] D.G. Churchill, M. Dutour Sikirić, B. Colovic, H.F. Milhofer, Contemporary topics about phosphorus in biology and materials, BoD–Books on Demand, (2020).  
[https://books.google.com/books/about/Contemporary\\_Topics\\_about\\_Phosphorus\\_in.html?hl=lt&id=TJYtEAAAQBAJ](https://books.google.com/books/about/Contemporary_Topics_about_Phosphorus_in.html?hl=lt&id=TJYtEAAAQBAJ).
- [52] N. Reznikov, R. Shahar, S. Weiner, Three-dimensional structure of human lamellar bone: The presence of two different materials and new insights into the hierarchical organization, *Bone* 59 (2014) 93–104. <https://doi.org/10.1016/J.BONE.2013.10.023>.
- [53] J.D. Black, B.J. Tadros, Bone structure: from cortical to calcium, *Orthop. Trauma* 34 (2020) 113–119.  
<https://doi.org/10.1016/J.MPORTH.2020.03.002>.
- [54] C.J. Hernandez, R.J. Majeska, M.B. Schaffler, Osteocyte density in woven bone, *Bone* 35 (2004) 1095–1099.  
<https://doi.org/10.1016/J.BONE.2004.07.002>.
- [55] X. Su, K. Sun, F.Z. Cui, W.J. Landis, Organization of apatite crystals in human woven bone, *Bone* 32 (2003) 150–162.  
[https://doi.org/10.1016/S8756-3282\(02\)00945-6](https://doi.org/10.1016/S8756-3282(02)00945-6).
- [56] J. Mitchell, A.H. van Heteren, A literature review of the spatial organization of lamellar bone, *Comptes Rendus Palevol* 15 (2016) 23–31. <https://doi.org/10.1016/J.CRPV.2015.04.007>.
- [57] H. Razi, J. Predan, F.D. Fischer, O. Kolednik, P. Fratzl, Damage tolerance of lamellar bone, *Bone* 130 (2020) 115102.  
<https://doi.org/10.1016/J.BONE.2019.115102>.
- [58] S.H. Ralston, Bone structure and metabolism, *Medicine (Baltimore)* 45 (2017) 560–564. <https://doi.org/10.1016/J.MPMED.2017.06.008>.
- [59] A. Ibrahim, N. Magliulo, J. Groben, A. Padilla, F. Akbik, Z.A. Hamid, Hardness, an Important Indicator of Bone Quality, and the Role of Collagen in Bone Hardness, *J. Funct. Biomater.* 11 (2020) 85. <https://doi.org/10.3390/JFB11040085>.
- [60] G. Kline, D. Orton, H. Sadrzadeh, Bone metabolism, *Endocr. Biomarkers Clin. Clin. Chem. Partnersh.* (2017) 157–180. <https://doi.org/10.1016/B978-0-12-803412-5.00004-5>.
- [61] M. Racila, J.M. Crolet, Nano and Macro Structure of Cortical Bone: Numerical Investigations, *Mech. Adv. Mater. Struct.* 14 (2007) 655–663. <https://doi.org/10.1080/15376490701673193>.

- [62] S. Li, A. Abdel-Wahab, V. V. Silberschmidt, Analysis of fracture processes in cortical bone tissue, Eng. Fract. Mech. 110 (2013) 448–458. <https://doi.org/10.1016/J.ENGFRACTMECH.2012.11.020>.
- [63] B. Chang, X. Liu, Osteon: Structure, Turnover, and Regeneration, <Https://Home.Liebertpub.Com/Teb> 28 (2022) 261–278. <https://doi.org/10.1089/TEN.TEB.2020.0322>.
- [64] J.D. Currey, The structure and mechanics of bone, J. Mater. Sci. 47 (2012) 41–54. <https://doi.org/10.1007/s10853-011-5914-9>.
- [65] T.M. Keaveny, E.F. Morgan, G.L. Niebur, O.C. Yeh, Biomechanics of trabecular bone, Annu. Rev. Biomed. Eng. 3 (2001) 307–333. <https://doi.org/10.1146/ANNUREV.BIOENG.3.1.307/CITE/REFWORKS>.
- [66] F. Barrère, C. van Blitterswijk, K. de Groot, Bone regeneration: molecular and cellular interactions with calcium phosphate ceramics, Int. J. Nanomedicine 1 (2006) 317–332. <https://www.tandfonline.com/doi/abs/10.2147/DIJN.1.S627>.
- [67] R.Z. LeGeros, Calcium phosphate-based osteoinductive materials, Chem. Rev. 108 (2008) 4742–4753. <https://doi.org/10.1021/cr800427g>.
- [68] S.K. Sarkar, B.T. Lee, Hard tissue regeneration using bone substitutes: an update on innovations in materials, Korean J. Intern. Med. 30 (2015) 279. <https://doi.org/10.3904/KJIM.2015.30.3.279>.
- [69] C.F. Arias, M.A. Herrero, L.F. Echeverri, G.E. Oleaga, J.M. López, Bone remodeling: A tissue-level process emerging from cell-level molecular algorithms, PLoS One 13 (2018) e0204171. <https://doi.org/10.1371/JOURNAL.PONE.0204171>.
- [70] R. Florencio-Silva, G.R.D.S. Sasso, E. Sasso-Cerri, M.J. Simões, P.S. Cerri, Biology of Bone Tissue: Structure, Function, and Factors That Influence Bone Cells, Biomed Res. Int. 2015 (2015) 421746. <https://doi.org/10.1155/2015/421746>.
- [71] S.H. Ralston, Bone structure and metabolism, Medicine (Baltimore). 41 (2013) 581–585. <https://doi.org/10.1016/J.MPMED.2013.07.007>.
- [72] B. Clarke, Normal bone anatomy and physiology., Clin. J. Am. Soc. Nephrol. 3 (2008) 131-139. <https://doi.org/10.2215/CJN.04151206>.
- [73] E.F. Eriksen, Cellular mechanisms of bone remodeling, Rev. Endocr. Metab. Disord. 11 (2010) 219–227. <https://doi.org/10.1007/s11154-010-9153-1>.
- [74] H. Jodati, B. Yılmaz, Z. Evis, A review of bioceramic porous scaffolds for hard tissue applications: Effects of structural features, Ceram. Int. 46 (2020) 15725–15739. <https://doi.org/10.1016/J.CERAMINT.2020.03.192>.

- [75] P. Pivonka, J. Zimak, D.W. Smith, B.S. Gardiner, C.R. Dunstan, N.A. Sims, T.J. Martin, G.R. Mundy, Model structure and control of bone remodeling: A theoretical study, *Bone* 43 (2008) 249–263. <https://doi.org/10.1016/J.BONE.2008.03.025>.
- [76] P. Rowe, A. Koller, S. Sharma, Physiology, *Bone Remodeling*, StatPearls (2018). <http://europepmc.org/books/NBK499863>.
- [77] D.J. Hadjidakis, I.I. Androulakis, *Bone Remodeling*, *Ann. N. Y. Acad. Sci.* 1092 (2006) 385–396. <https://doi.org/10.1196/ANNALS.1365.035>.
- [78] X. Feng, J.M. McDonald, Disorders of bone remodeling, *Annu. Rev. Pathol. Mech. Dis.* 6 (2011) 121–145. <https://doi.org/10.1146/annurev-pathol-011110-130203>.
- [79] P. Kostenuik, On the evolution and contemporary roles of bone remodeling, *Marcus Feldman's Osteoporos.* 1 (2021) 727–772. <https://doi.org/10.1016/B978-0-12-813073-5.00031-9>.
- [80] J.S. Kenkre, J.H.D. Bassett, The bone remodelling cycle, *Ann. Clin. Biochem.* 55 (2018) 308–327. <https://doi.org/10.1177/0004563218759371>.
- [81] L.G. Raisz, Physiology and Pathophysiology of Bone Remodeling, *Clin. Chem.* 45 (1999) 1353–1358. <https://doi.org/10.1093/CLINCHEM/45.8.1353>.
- [82] G. Brunetti, A. Di Benedetto, G. Mori, Bone remodeling, Imaging Prosthet. Joints A Comb. Radiol. Clin. Perspect. (2014) 27–37. [https://link.springer.com/chapter/10.1007/978-88-470-5483-7\\_3](https://link.springer.com/chapter/10.1007/978-88-470-5483-7_3).
- [83] R. Mukherjee, C.-M. Chang, R.P. Pandey, R. Mukherjee, C.-M. Chang, R.P. Pandey, Immunology and Osteoporosis: A New Frontier in Treatment, *Osteoporos. - Pathophysiol. Diagnosis, Manag. Ther.* (2023). <https://doi.org/10.5772/intechopen.1002916>.
- [84] T.J. Blokhuis, M.F. Termaat, F.C. Boer, P. Patka, F.C. Bakker, H.J.Th. Haarmann, Properties of calcium phosphate ceramics in relation to their in vivo behavior, *J Trauma* 48 (2000) 179. [https://journals.lww.com/jtrauma/fulltext/2000/01000/properties\\_of\\_calcium\\_phosphate\\_ceramics\\_in.aspx](https://journals.lww.com/jtrauma/fulltext/2000/01000/properties_of_calcium_phosphate_ceramics_in.aspx).
- [85] J. Huang, Y. Ma, K. Pang, X. Ma, Z. Zheng, D. Xu, K. Xiong, B. Yu, L. Liao, Anisotropic Microspheres-Cryogel Composites Loaded with Magnesium l-Threonate Promote Osteogenesis, Angiogenesis, and Neurogenesis for Repairing Bone Defects, *Biomacromolecules* 24 (2023) 3171–3183. <https://doi.org/10.1021/ACS.BIOMAC.3C00243>.
- [86] H. Zhou, B. Liang, H. Jiang, Z. Deng, K. Yu, Magnesium-based biomaterials as emerging agents for bone repair and regeneration: from mechanism to application, *J. Magnes. Alloy.* 9 (2021) 779–804. <https://doi.org/10.1016/J.JMA.2021.03.004>.

- [87] X. Nie, X. Sun, C. Wang, J. Yang, Effect of magnesium ions/Type I collagen promote the biological behavior of osteoblasts and its mechanism, *Regen. Biomater.* 7 (2020) 53–61.  
<https://doi.org/10.1093/RB/RBZ033>.
- [88] F.D. Al-Shalawi, A.H. Mohamed Ariff, D.W. Jung, M.K.A. Mohd Ariffin, C.L. Seng Kim, D. Brabazon, M.O. Al-Osaimi, Biomaterials as Implants in the Orthopedic Field for Regenerative Medicine: Metal versus Synthetic Polymers, *Polym.* 15 (2023) 2601.  
<https://doi.org/10.3390/POLYM15122601>.
- [89] K. Zhang, S. Wang, C. Zhou, L. Cheng, X. Gao, X. Xie, J. Sun, H. Wang, M.D. Weir, M.A. Reynolds, N. Zhang, Y. Bai, H.H.K. Xu, Advanced smart biomaterials and constructs for hard tissue engineering and regeneration, *Bone Res.* 6 (2018) 1–15.  
<https://doi.org/10.1038/s41413-018-0032-9>.
- [90] J.W. Łuczak, M. Palusińska, D. Matak, D. Pietrzak, P. Nakielski, S. Lewicki, M. Grodzik, Ł. Szymański, The Future of Bone Repair: Emerging Technologies and Biomaterials in Bone Regeneration, *Int. J. Mol. Sci.* 25 (2024) 12766. <https://doi.org/10.3390/IJMS252312766>.
- [91] L. Kjalarsdóttir, A. Dýrfjörd, A. Dagbjartsson, E.H. Laxdal, G. Örlygsson, J. Gíslason, J.M. Einarsson, C.H. Ng, H. Jónsson, Bone remodeling effect of a chitosan and calcium phosphate-based composite, *Regen. Biomater.* 6 (2019) 241–247.  
<https://doi.org/10.1093/RB/RBZ009>.
- [92] Global Orthopedic Market Revenue to Exceed \$61 Billion in 2023, *ORTHOPAEDIC INDUSTRY ANNUAL REPORT®* (2023)  
<https://www.prnewswire.com/news-releases/global-orthopedic-market-revenue-to-exceed-61-billion-in-2023-300861796.html>.
- [93] D. Wahl, J.C.-E.C. Mater, Collagen-hydroxyapatite composites for hard tissue repair, *Eur Cell Mater* 11 (2006) 43-56.  
<https://core.ac.uk/download/pdf/25887855.pdf>
- [94] What is a biomaterial? — Center for Professional Personnel Development — Department of Agricultural Economics, Sociology, and Education.  
<https://aese.psu.edu/teachag/curriculum/modules/biomaterials/what-is-a-biomaterial>.
- [95] M. Chelu, A.M. Musuc, Advanced Biomedical Applications of Multifunctional Natural and Synthetic Biomaterials, *Process.* 11 (2023) 2696. <https://doi.org/10.3390/PR11092696>.
- [96] Biomaterials, NIBIB (2024). <https://www.nibib.nih.gov/science-education/science-topics/biomaterial-technologies>.

- [97] M.S. Birajdar, H. Joo, W.G. Koh, H. Park, Natural bio-based monomers for biomedical applications: a review, *Biomater. Res.* 25 (2021) 1–14. <https://doi.org/10.1186/S40824-021-00208-8>.
- [98] F.M. Klenke, K.A. Siebenrock, Osteology in Orthopedics – Bone Repair, Bone Grafts and Bone Graft Substitutes, *Ref. Modul. Biomed. Sci.* (2016). <https://doi.org/10.1016/B978-0-12-801238-3.99488-1>.
- [99] R. Drevet, J. Fauré, H. Benhayoune, Bioactive Calcium Phosphate Coatings for Bone Implant Applications: A Review, *Coatings* 13 (2023) 1091. <https://doi.org/10.3390/COATINGS13061091>.
- [100] W. Habraken, P. Habibovic, M. Epple, M. Bohner, Calcium phosphates in biomedical applications: materials for the future?, *Mater. Today* 19 (2016) 69–87.  
<https://doi.org/10.1016/J.MATTOD.2015.10.008>.
- [101] F.W. Bloemers, T.J. Blokhuis, P. Patka, F.C. Bakker, B.W. Wippermann, H.J.T.M. Haarman, Autologous bone versus calcium-phosphate ceramics in treatment of experimental bone defects, *J. Biomed. Mater. Res. Part B Appl. Biomater.* 66B (2003) 526–531. <https://doi.org/10.1002/JBM.B.10045>.
- [102] R. Schnettler, J.P. Stahl, V. Alt, T. Pavlidis, E. Dingeldein, S. Wenisch, Calcium phosphate-based bone substitutes, *Eur. J. Trauma* 30 (2004) 219–229. <https://doi.org/10.1007/s00068-004-1393-x>.
- [103] M. Canillas, P. Pena, A.H. De Aza, M.A. Rodríguez, Calcium phosphates for biomedical applications, *Boletín La Soc. Española Cerámica y Vidr.* 56 (2017) 91–112.  
<https://doi.org/10.1016/J.BSECV.2017.05.001>.
- [104] S. Chiba, T. Anada, K. Suzuki, K. Saito, Y. Shiwaku, N. Miyatake, K. Baba, H. Imaizumi, M. Hosaka, E. Itoi, O. Suzuki, Effect of resorption rate and osteoconductivity of biodegradable calcium phosphate materials on the acquisition of natural bone strength in the repaired bone, *J. Biomed. Mater. Res. Part A* 104 (2016) 2833–2842. <https://doi.org/10.1002/JBM.A.35828>.
- [105] Y. Zhang, T. Shu, S. Wang, Z. Liu, Y. Cheng, A. Li, D. Pei, The Osteoinductivity of Calcium Phosphate-Based Biomaterials: A Tight Interaction With Bone Healing, *Front. Bioeng. Biotechnol.* 10 (2022) 911180. <https://doi.org/10.3389/fbioe.2022.911180>.
- [106] Z. Sheikh, M.N. Abdallah, A.A. Hanafi, S. Misbahuddin, H. Rashid, M. Glogauer, Mechanisms of in Vivo Degradation and Resorption of Calcium Phosphate Based Biomaterials, *Materials (Basel)*. 8 (2015) 7913. <https://doi.org/10.3390/MA8115430>.
- [107] Z. Tang, Y. Tan, Y. Ni, J. Wang, X. Zhu, Y. Fan, X. Chen, X. Yang,

- X. Zhang, Comparison of ectopic bone formation process induced by four calcium phosphate ceramics in mice, *Mater. Sci. Eng. C* 70 (2017) 1000–1010. <https://doi.org/10.1016/J.MSEC.2016.06.097>.
- [108] L. Cheng, Y. Shi, F. Ye, H. Bu, Osteoinduction of calcium phosphate biomaterials in small animals, *Mater. Sci. Eng. C* 33 (2013) 1254–1260. <https://doi.org/10.1016/J.MSEC.2012.12.023>.
- [109] I. Lodoso-Torrecilla, J.J.J.P. van den Beucken, J.A. Jansen, Calcium phosphate cements: Optimization toward biodegradability, *Acta Biomater.* 119 (2021) 1–12.  
<https://doi.org/10.1016/J.ACTBIO.2020.10.013>.
- [110] J. Lu, M. Descamps, J. Dejou, G. Koubi, P. Hardouin, J. Lemaitre, J.P. Proust, The biodegradation mechanism of calcium phosphate biomaterials in bone, *J. Biomed. Mater. Res.* 63 (2002) 408–412. <https://doi.org/10.1002/JBM.10259>.
- [111] W. Cao, L.L. Hench, Bioactive materials, *Ceram. Int.* 22 (1996) 493–507. [https://doi.org/10.1016/0272-8842\(95\)00126-3](https://doi.org/10.1016/0272-8842(95)00126-3).
- [112] The Williams Dictionary of Biomaterials, Liverpool University Press, (1999)  
[https://books.google.lt/books?hl=lt&lr=&id=Hv45B7P5N3gC&oi=fnd&pg=PR5&dq=The+Williams+Dictionary+of+Biomaterials&ots=hQrUYjk6Zp&sig=cToPV6VflboBG2Y2UI0YUwNNLuE&redir\\_esc=y#v=onepage&q=The%20Williams%20Dictionary%20of%20Biomaterials&f=false](https://books.google.lt/books?hl=lt&lr=&id=Hv45B7P5N3gC&oi=fnd&pg=PR5&dq=The+Williams+Dictionary+of+Biomaterials&ots=hQrUYjk6Zp&sig=cToPV6VflboBG2Y2UI0YUwNNLuE&redir_esc=y#v=onepage&q=The%20Williams%20Dictionary%20of%20Biomaterials&f=false).
- [113] A. Das, S. Ghosh, T. Ringu, N. Pramanik, A Focus on Biomaterials Based on Calcium Phosphate Nanoparticles: an Indispensable Tool for Emerging Biomedical Applications, *BioNanoSci.* 13 (2023) 795–818. <https://doi.org/10.1007/s12668-023-01081-6>.
- [114] L.L. Hench, An Introduction To Bioceramics, An. World Scientific Publishing Company, (2013).  
[https://books.google.lt/books?hl=lt&lr=&id=mrzsCgAAQBAJ&oi=fnd&pg=PR7&ots=NyifLJKg5g&sig=RAhFtpGjpOyQ1pCYg9QsuvJ84Y&redir\\_esc=y#v=onepage&q&f=false](https://books.google.lt/books?hl=lt&lr=&id=mrzsCgAAQBAJ&oi=fnd&pg=PR7&ots=NyifLJKg5g&sig=RAhFtpGjpOyQ1pCYg9QsuvJ84Y&redir_esc=y#v=onepage&q&f=false).
- [115] Z. Tang, X. Li, Y. Tan, H. Fan, X. Zhang, The material and biological characteristics of osteoinductive calcium phosphate ceramics, *Regen. Biomater.* 5 (2018) 43–59. <https://doi.org/10.1093/RB/RBX024>.
- [116] H. Yuan, K. de Groot, Calcium Phosphate Biomaterials: An Overview, 171 (2004) 37–57. [https://doi.org/10.1007/1-4020-2648-X\\_3](https://doi.org/10.1007/1-4020-2648-X_3).
- [117] O. Chan, M.J. Coathup, A. Nesbitt, C.Y. Ho, K.A. Hing, T. Buckland, C. Campion, G.W. Blunn, The effects of microporosity on osteoinduction of calcium phosphate bone graft substitute

- biomaterials, *Acta Biomater.* 8 (2012) 2788–2794.  
<https://doi.org/10.1016/J.ACTBIO.2012.03.038>.
- [118] P. Jin, L. Liu, L. Cheng, X. Chen, S. Xi, T. Jiang, Calcium-to-phosphorus releasing ratio affects osteoinductivity and osteoconductivity of calcium phosphate bioceramics in bone tissue engineering, *Biomed. Eng. Online* 22 (2023) 1–16.  
<https://link.springer.com/article/10.1186/s12938-023-01067-1>.
- [119] S. Ali Akbari Ghavimi, B.N. Allen, J.L. Stromsdorfer, J.S. Kramer, X. Li, B.D. Ulery, Calcium and phosphate ions as simple signaling molecules with versatile osteoinductivity, *Biomed. Mater.* 13 (2018) 055005. <https://doi.org/10.1088/1748-605X/AAC7A5>.
- [120] T. Nakamura, M. Takemoto, Osteoconduction and its evaluation, *Bioceram. Their Clin. Appl.* (2008) 183–198.  
<https://doi.org/10.1533/9781845694227.1.183>.
- [121] S. Agrawal, R. Srivastava, Osteoinductive and osteoconductive biomaterials, *Racing Surf. Antimicrob. Interface Tissue Eng.* (2020) 355–395. [https://link.springer.com/chapter/10.1007/978-3-030-34471-9\\_15](https://link.springer.com/chapter/10.1007/978-3-030-34471-9_15).
- [122] P. Kazimierczak, A. Przekora, Osteoconductive and Osteoinductive Surface Modifications of Biomaterials for Bone Regeneration: A Concise Review, *Coatings* 2020, 10 (2020) 971.  
<https://doi.org/10.3390/COATINGS10100971>.
- [123] N. Eliaz, N. Metoki, Calcium Phosphate Bioceramics: A Review of Their History, Structure, Properties, Coating Technologies and Biomedical Applications, *Mater.* 10 (2017) 334.  
<https://doi.org/10.3390/MA10040334>.
- [124] L. Gineste, M. Gineste, X. Ranz, A. Ellefterion, A. Guilhem, N. Rouquet, P. Frayssinet, Degradation of hydroxylapatite, fluorapatite, and fluorhydroxyapatite coatings of dental implants in dogs, *J. Biomed. Mater. Res.* 48 (1999) 224–234.  
[https://doi.org/10.1002/\(SICI\)1097-4636\(1999\)48:3%3C224::AID-JBM5%3E3.0.CO;2-A](https://doi.org/10.1002/(SICI)1097-4636(1999)48:3%3C224::AID-JBM5%3E3.0.CO;2-A).
- [125] R.A. Surmenev, M.A. Surmeneva, A critical review of decades of research on calcium phosphate-based coatings: How far are we from their widespread clinical application?, *Curr. Opin. Biomed. Eng.* 10 (2019) 35–44. <https://doi.org/10.1016/J.COBME.2019.02.003>.
- [126] Y. Song, S. Zhang, J. Li, C. Zhao, X. Zhang, Electrodeposition of Ca-P coatings on biodegradable Mg alloy: In vitro biomineratization behavior, *Acta Biomater.* 6 (2010) 1736–1742.  
<https://doi.org/10.1016/J.ACTBIO.2009.12.020>.
- [127] M. Kasaeian-Naeini, M. Sedighi, R. Hashemi, Severe plastic

- deformation (SPD) of biodegradable magnesium alloys and composites: A review of developments and prospects, *J. Magnes. Alloy.* 10 (2022) 938–955.  
<https://doi.org/10.1016/J.JMA.2021.11.006>.
- [128] M.T. Islam, R.M. Felfel, E.A. Abou Neel, D.M. Grant, I. Ahmed, K.M.Z. Hossain, Bioactive calcium phosphate-based glasses and ceramics and their biomedical applications: A review, *J. Tissue Eng.* 8 (2017). <https://doi.org/10.1177/2041731417719170>.
- [129] Y. Su, I. Cockerill, Y. Zheng, L. Tang, Y.X. Qin, D. Zhu, Biofunctionalization of metallic implants by calcium phosphate coatings, *Bioact. Mater.* 4 (2019) 196–206.  
<https://doi.org/10.1016/J.BIOACTMAT.2019.05.001>.
- [130] B. Aksakal, M. Kom, H.B. Tosun, M. Demirel, Influence of micro- and nano-hydroxyapatite coatings on the osteointegration of metallic (Ti6Al4 V) and bioabsorbable interference screws: An in vivo study, *Eur. J. Orthop. Surg. Traumatol.* 24 (2014) 813–819.  
<https://doi.org/10.1007/s00590-013-1236-8>.
- [131] S. Bose, S. Tarafder, Calcium phosphate ceramic systems in growth factor and drug delivery for bone tissue engineering: A review, *Acta Biomater.* 8 (2012) 1401–1421.  
<https://doi.org/10.1016/J.ACTBIO.2011.11.017>.
- [132] M. Roy, A. Bandyopadhyay, S. Bose, In vitro antimicrobial and biological properties of laser assisted tricalcium phosphate coating on titanium for load bearing implant, *Mater. Sci. Eng. C* 29 (2009) 1965–1968. <https://doi.org/10.1016/J.MSEC.2009.03.009>.
- [133] M.P. Ginebra, C. Canal, M. Espanol, D. Pastorino, E.B. Montufar, Calcium phosphate cements as drug delivery materials, *Adv. Drug Deliv. Rev.* 64 (2012) 1090–1110.  
<https://doi.org/10.1016/J.ADDR.2012.01.008>.
- [134] L. Schröter, F. Kaiser, S. Stein, U. Gbureck, A. Ignatius, Biological and mechanical performance and degradation characteristics of calcium phosphate cements in large animals and humans, *Acta Biomater.* 117 (2020) 1–20.  
<https://doi.org/10.1016/J.ACTBIO.2020.09.031>.
- [135] A.M. Yousefi, A review of calcium phosphate cements and acrylic bone cements as injectable materials for bone repair and implant fixation, *J. Appl. Biomater. Funct. Mater.* 17 (2019).  
<https://doi.org/10.1177/2280800019872594>.
- [136] K. Ishikawa, Calcium Phosphate Cement, Springer Series in Biomaterials Science and Engineering 2 (2014) 199–227.

- [https://doi.org/10.1007/978-3-642-53980-0\\_7](https://doi.org/10.1007/978-3-642-53980-0_7).
- [137] J. Zhang, W. Liu, V. Schnitzler, F. Tancret, J.M. Bouler, Calcium phosphate cements for bone substitution: Chemistry, handling and mechanical properties, *Acta Biomater.* 10 (2014) 1035–1049. <https://doi.org/10.1016/J.ACTBIO.2013.11.001>.
- [138] I. Denry, L.T. Kuhn, Design and characterization of calcium phosphate ceramic scaffolds for bone tissue engineering, *Dent. Mater.* 32 (2016) 43–53. <https://doi.org/10.1016/J.DENTAL.2015.09.008>.
- [139] A. Bigi, E. Boanini, Functionalized biomimetic calcium phosphates for bone tissue repair, *J. Appl. Biomater. Funct. Mater.* 15 (2017) e313–e325. <https://doi.org/10.5301/jabfm.5000367>.
- [140] M. Touri, F. Moztarzadeh, N.A.A. Osman, M.M. Dehghan, M. Mozafari, 3D-printed biphasic calcium phosphate scaffolds coated with an oxygen generating system for enhancing engineered tissue survival, *Mater. Sci. Eng. C* 84 (2018) 236–242. <https://doi.org/10.1016/J.MSEC.2017.11.037>.
- [141] R. Detsch, S. Schaefer, U. Deisinger, G. Ziegler, H. Seitz, B. Leukers, In vitro -Osteoclastic Activity Studies on Surfaces of 3D Printed Calcium Phosphate Scaffolds, *J. Biomater. Appl.* 26 (2010) 359-380. <https://doi.org/10.1177/0885328210373285>.
- [142] V.S. Chaudhari, P. Kushram, S. Bose, Drug delivery strategies through 3D-printed calcium phosphate, *Trends Biotechnol.* 42 (2024) 1396–1409. [https://www.cell.com/trends/biotechnology/fulltext/S0167-7799\(24\)00145-8](https://www.cell.com/trends/biotechnology/fulltext/S0167-7799(24)00145-8).
- [143] K. Hayashi, T. Yanagisawa, M. Shimabukuro, R. Kishida, K. Ishikawa, Granular honeycomb scaffolds composed of carbonate apatite for simultaneous intra- and inter-granular osteogenesis and angiogenesis, *Mater. Today Bio* 14 (2022) 100247. <https://doi.org/10.1016/J.MTBIO.2022.100247>.
- [144] O.N. Musskaya, A.I. Kulak, V.K. Krut'ko, Y.A. Lesnikovich, V. V. Kazbanov, N.S. Zhirkova, Preparation of Bioactive Mesoporous Calcium Phosphate Granules, *Inorg. Mater.* 54 (2018) 117–124. <https://doi.org/10.1134/S0020168518020115>.
- [145] G.M.L. Dalmônico, P.F. Franczak, N. Levandowski, N.H.A. Camargo, A.L. Dallabrida, B.D. Da Costa, O.G. Gil, O. Cambra-Moo, M.A. Rodríguez, M. Canillas, An in vivo study on bone formation behavior of microporous granular calcium phosphate, *Biomater. Sci.* 5 (2017) 1315–1325. <https://doi.org/10.1039/C7BM00162B>.
- [146] S. Takeda, A. Tsuchiya, M. Moriyama, K. Ishikawa, Physical and histological comparison of three-dimensional interconnected porous

- carbonate apatite bone graft fabricated with cylindrical and spherical granules, *Ceram. Int.* 50 (2024) 53544–53551.  
<https://doi.org/10.1016/J.CERAMINT.2024.10.203>.
- [147] L. Schröter, F. Kaiser, O. Küppers, S. Stein, B. Krüger, P. Wohlfahrt, I. Geroneit, P. Stahlhut, U. Gbureck, A. Ignatius, Improving bone defect healing using magnesium phosphate granules with tailored degradation characteristics, *Dent. Mater.* 40 (2024) 508–519.  
<https://doi.org/10.1016/J.DENTAL.2023.12.019>.
- [148] S. Sakai, T. Anada, K. Tsuchiya, H. Yamazaki, H.C. Margolis, O. Suzuki, Comparative study on the resorbability and dissolution behavior of octacalcium phosphate,  $\beta$ -tricalcium phosphate, and hydroxyapatite under physiological conditions, *Dent. Mater. J.* 35 (2016) 216–224. <https://doi.org/10.4012/DMJ.2015-255>.
- [149] Z. Bal, T. Kaito, F. Korkusuz, H. Yoshikawa, Bone regeneration with hydroxyapatite-based biomaterials, *Emergent Mater.* 3 (2020) 521–544. <https://doi.org/10.1007/s42247-019-00063-3>.
- [150] S. Batool, U. Liaqat, B. Babar, Z. Hussain, Bone whitlockite: synthesis, applications, and future prospects, *J. Korean Ceram. Soc.* 2021 585 58 (2021) 530–547. <https://doi.org/10.1007/S43207-021-00120-W>.
- [151] D.B. Bhuiyan, J.C. Middleton, R. Tannenbaum, T.M. Wick, Mechanical properties and osteogenic potential of hydroxyapatite-PLGA-collagen biomaterial for bone regeneration, *J. Biomater. Sci. Polym. Ed.* 27 (2016) 1139–1154.  
<https://doi.org/10.1080/09205063.2016.1184121>.
- [152] R.O. Kareem, N. Bulut, O. Kaygili, Hydroxyapatite Biomaterials: A Comprehensive Review of their Properties, Structures, Medical Applications, and Fabrication Methods, *J. Chem. Rev.* 6 (2024) 1–26. <https://doi.org/10.48309/JCR.2024.415051.1253>.
- [153] V.S. Kattimani, S. Kondaka, K.P. Lingamaneni, Hydroxyapatite—Past, Present, and Future in Bone Regeneration, *Bone and Tissue Regeneration Insights* 7 (2016). <https://doi.org/10.4137/BTRI.S36138>.
- [154] D.V. Abere, S.A. Ojo, G.M. Oyatogun, M.B. Paredes-Epinosa, M.C.D. Niluxsshun, A. Hakami, Mechanical and morphological characterization of nano-hydroxyapatite (nHA) for bone regeneration: A mini review, *Biomed. Eng. Adv.* 4 (2022) 100056.  
<https://doi.org/10.1016/J.BEA.2022.100056>.
- [155] N. Ramesh, S.C. Moratti, G.J. Dias, Hydroxyapatite–polymer biocomposites for bone regeneration: A review of current trends, *J. Biomed. Mater. Res. Part B Appl. Biomater.* 106 (2018) 2046–2057.

- <https://doi.org/10.1002/JBM.B.33950>.
- [156] A. Szczęś, L. Hołysz, E. Chibowski, Synthesis of hydroxyapatite for biomedical applications, *Adv. Colloid Interface Sci.* 249 (2017) 321–330. <https://doi.org/10.1016/J.CIS.2017.04.007>.
  - [157] D.G. Filip, V.A. Surdu, A.V. Paduraru, E. Andronescu, Current Development in Biomaterials—Hydroxyapatite and Bioglass for Applications in Biomedical Field: A Review, *J. Funct. Biomater.* 213 (2022) 248. <https://doi.org/10.3390/JFB13040248>.
  - [158] S. Mondal, S. Park, J. Choi, T.T.H. Vu, V.H.M. Doan, T.T. Vo, B. Lee, J. Oh, Hydroxyapatite: A journey from biomaterials to advanced functional materials, *Adv. Colloid Interface Sci.* 321 (2023) 103013. <https://doi.org/10.1016/J.CIS.2023.103013>.
  - [159] M. Saleem, S. Rasheed, C. Yougen, Silk fibroin/hydroxyapatite scaffold: a highly compatible material for bone regeneration, *Sci. Technol. Adv. Mater.* 21 (2020) 242–266.  
<https://doi.org/10.1080/14686996.2020.1748520>.
  - [160] Z. Zhong, X. Wu, Y. Wang, M. Li, Y. Li, X.L. Liu, X. Zhang, Z. Lan, J. Wang, Y. Du, S. Zhang, Zn/Sr dual ions-collagen co-assembly hydroxyapatite enhances bone regeneration through procedural osteoimmunomodulation and osteogenesis, *Bioact. Mater.* 10 (2022) 195–206. <https://doi.org/10.1016/J.BIOACTMAT.2021.09.013>.
  - [161] A.S.M. Zaffarin, S.F. Ng, M.H. Ng, H. Hassan, E. Alias, Nano-Hydroxyapatite as a Delivery System for Promoting Bone Regeneration In Vivo: A Systematic Review, *Nanomater.* 11 (2021) 2569. <https://doi.org/10.3390/NANO11102569>.
  - [162] S. Mondal, B. Mondal, A. Dey, S.S. Mukhopadhyay, Studies on Processing and Characterization of Hydroxyapatite Biomaterials from Different Bio Wastes, *J. Miner. Mater. Charact. Eng.* 11 (2012) 55-67. [https://file.scirp.org/pdf/JMMCE20120100005\\_62409258.pdf](https://file.scirp.org/pdf/JMMCE20120100005_62409258.pdf).
  - [163] C.C. Liu, A. Solderer, C. Heumann, T. Attin, P.R. Schmidlin, Tricalcium phosphate (-containing) biomaterials in the treatment of periodontal infra-bony defects: A systematic review and meta-analysis, *J. Dent.* 114 (2021) 103812.  
<https://doi.org/10.1016/J.JDENT.2021.103812>.
  - [164] L. Xie, Y. Yang, Z. Fu, Y. Li, J. Shi, D. Ma, S. Liu, D. Luo, Fe/Zn-modified tricalcium phosphate (TCP) biomaterials: preparation and biological properties, *RSC Adv.* 9 (2019) 781–789.  
<https://doi.org/10.1039/C8RA08453J>.
  - [165] M.C. Tronco, J.B. Cassel, L.A. dos Santos,  $\alpha$ -TCP-based calcium phosphate cements: A critical review, *Acta Biomater.* 151 (2022) 70–

87. <https://doi.org/10.1016/J.ACTBIO.2022.08.040>.
- [166] K. Szurkowska, Ł. Szeleszczuk, J. Kolmas, Effects of Synthesis Conditions on the Formation of Si-Substituted Alpha Tricalcium Phosphates, *Int. J. Mol. Sci.* 21 (2020) 9164.  
<https://doi.org/10.3390/IJMS21239164>.
- [167] I.O. Oladele, S.A. Adekola, N.I. Agbeboh, B.A. Isola-Makinde, B.O. Adewuyi, Synthesis and Application of Sustainable Tricalcium Phosphate Based Biomaterials From Agro-Based Materials: A Review, *Biomed. eng. comput. biol.* 15 (2024).  
<https://doi.org/10.1177/11795972241293525>.
- [168] G. Cicek, E.A. Aksoy, C. Durucan, N. Hasirci, Alpha-tricalcium phosphate ( $\alpha$ -TCP): Solid state synthesis from different calcium precursors and the hydraulic reactivity, *J. Mater. Sci. Mater. Med.* 22 (2011) 809–817. <https://doi.org/10.1007/s10856-011-4283-x>.
- [169] H. Chaair, H. Labjar, O. Britel, Synthesis of  $\beta$ -tricalcium phosphate, *Morphologie* 101 (2017) 120–124.  
<https://doi.org/10.1016/J.MORPHO.2017.06.002>.
- [170] J. Kolmas, A. Kaflak, A. Zima, A. Tólsarczyk, Alpha-tricalcium phosphate synthesized by two different routes: Structural and spectroscopic characterization, *Ceram. Int.* 41 (2015) 5727–5733.  
<https://doi.org/10.1016/J.CERAMINT.2014.12.159>.
- [171] S. Gallinetti, C. Canal, M.P. Ginebra, Development and Characterization of Biphasic Hydroxyapatite/ $\beta$ -TCP Cements, *J. Am. Ceram. Soc.* 97 (2014) 1065–1073.  
<https://doi.org/10.1111/JACE.12861>.
- [172] M. Ebrahimi, M.G. Botelho, S. V. Dorozhkin, Biphasic calcium phosphates bioceramics (HA/TCP): Concept, physicochemical properties and the impact of standardization of study protocols in biomaterials research, *Mater. Sci. Eng. C* 71 (2017) 1293–1312.  
<https://doi.org/10.1016/J.MSEC.2016.11.039>.
- [173] S. Sureshbabu, M. Komath, H.K. Varma, In Situ Formation of Hydroxyapatite – Alpha Tricalcium Phosphate Biphasic Ceramics with Higher Strength and Bioactivity, *J. Am. Ceram. Soc.* 95 (2012) 915–924. <https://doi.org/10.1111/J.1551-2916.2011.04987.X>.
- [174] R.Z. Legeros, S. Lin, R. Rohanizadeh, D. Mijares, J.P. Legeros, Biphasic calcium phosphate bioceramics: Preparation, properties and applications, *J. Mater. Sci. Mater. Med.* 14 (2003) 201–209.  
<https://doi.org/10.1023/A:1022872421333>.
- [175] D. Guo, K. Xu, Y. Han, The in situ synthesis of biphasic calcium phosphate scaffolds with controllable compositions, structures, and

- adjustable properties, *J. Biomed. Mater. Res. Part A* 88A (2009) 43–52. <https://doi.org/10.1002/JBM.A.31844>.
- [176] S.E. Lobo, R. Glickman, W.N. da Silva, T.L. Arinze, I. Kerkis, Response of stem cells from different origins to biphasic calcium phosphate bioceramics, *Cell Tissue Res.* 361 (2015) 477–495. <https://doi.org/10.1007/s00441-015-2116-9>.
- [177] E.U. Lee, D.J. Kim, H.C. Lim, J.S. Lee, U.W. Jung, S.H. Choi, Comparative evaluation of biphasic calcium phosphate and biphasic calcium phosphate collagen composite on osteoconductive potency in rabbit calvarial defect, *Biomater. Res.* 19 (2015). <https://spj.science.org/doi/full/10.1186/s40824-014-0026-7>.
- [178] A. Afonina, A. Dubauskas, V. Klimavicius, A. Zarkov, A. Kareiva, I. Grigoraviciute, Phase transformations during the dissolution-precipitation synthesis of magnesium whitlockite nanopowders from gypsum, *Ceram. Int.* 49 (2023) 38157–38164. <https://doi.org/10.1016/J.CERAMINT.2023.09.146>.
- [179] S. Batool, Z. Hussain, U. Liaqat, M. Sohail, Solid-state synthesis and process optimization of bone whitlockite, *Ceram. Int.* 48 (2022) 13850–13854. <https://doi.org/10.1016/J.CERAMINT.2022.01.267>.
- [180] M. Nabiyouni, Y. Ren, S.B. Bhaduri, Magnesium substitution in the structure of orthopedic nanoparticles: A comparison between amorphous magnesium phosphates, calcium magnesium phosphates, and hydroxyapatites, *Mater. Sci. Eng. C* 52 (2015) 11–17. <https://doi.org/10.1016/J.MSEC.2015.03.032>.
- [181] J. Kolmas, P. Romaniuk, D. Predoi, A. Drobniwska, K. Burdan, B. Kołodziejska, Magnesium ion substitution in various calcium phosphates: A way towards bone regeneration, *Ceram. Int.* 51 (2025) 1153–1160. <https://doi.org/10.1016/J.CERAMINT.2024.11.096>.
- [182] G. Kazakova, T. Safranova, D. Golubchikov, O. Shevtsova, J. V. Rau, Resorbable Mg<sup>2+</sup>-Containing Phosphates for Bone Tissue Repair, *Mater.* 14 (2021) 4857. <https://doi.org/10.3390/MA14174857>.
- [183] A.A. Awan, U. Liaqat, Z. Hussain, W. Miran, Whitlockite-A study on the effect of reaction parameters on morphology in one-solvent system, *Mater. Chem. Phys.* 314 (2024) 128932. <https://doi.org/10.1016/j.matchemphys.2024.128932>.
- [184] Y. Pang, D. Li, J. Zhou, X. Liu, M. Li, Y. Zhang, D. Zhang, X. Zhang, Q. Cai, In vitro and in vivo evaluation of biomimetic hydroxyapatite/whitlockite inorganic scaffolds for bone tissue regeneration, *Biomed. Mater.* 17 (2022) 065020.

- <https://doi.org/10.1088/1748-605X/AC95E9>.
- [185] Y.Z. Jin, G. Bin Zheng, H.L. Jang, K.M. Lee, J.H. Lee, Whitlockite Promotes Bone Healing in Rabbit Ilium Defect Model, *J. Med. Biol. Eng.* 39 (2019) 944–951. <https://doi.org/10.1007/S40846-019-00471-0/TABLES/2>.
- [186] J.-T. Lee, S. Kim, Comparison of the biocompatibility and osteogenesis potential of whitlockite and an activin A/BMP2 chimera using a rat calvarial defect model: a pilot study, *J. Periodontal Implant Sci.* 54 (2023) 432–443. <https://doi.org/10.5051/JPIS.2304280214>.
- [187] J. Li, K. Li, Y. Ding, S. Zhang, T. Hu, S. Wang, X. Zheng, Hydroxyapatite-whitlockite composite coating as a biomimetic material for bone integration, *Surf. Coatings Technol.* 487 (2024) 131019. <https://doi.org/10.1016/J.SURFCOAT.2024.131019>.
- [188] D. Zhou, C. Qi, Y.X. Chen, Y.J. Zhu, T.W. Sun, F. Chen, C.Q. Zhang, Comparative study of porous hydroxyapatite/chitosan and whitlockite/chitosan scaffolds for bone regeneration in calvarial defects, *Int. J. Nanomedicine* 12 (2017) 2673–2687.  
<https://doi.org/10.2147/IJN.S131251>.
- [189] H.D. Kim, H.L. Jang, H.Y. Ahn, H.K. Lee, J. Park, E. seo Lee, E.A. Lee, Y.H. Jeong, D.G. Kim, K.T. Nam, N.S. Hwang, Biomimetic whitlockite inorganic nanoparticles-mediated in situ remodeling and rapid bone regeneration, *Biomaterials* 112 (2017) 31–43.  
<https://doi.org/10.1016/J.BIOMATERIALS.2016.10.009>.
- [190] F. Xiao, J. Shi, X. Zhang, M. Hu, K. Chen, C. Shen, X. Chen, Y. Guo, Y. Li, Gadolinium-doped whitlockite/chitosan composite scaffolds with osteogenic activity for bone defect treatment: In vitro and in vivo evaluations, *Front. Bioeng. Biotechnol.* 11 (2023) 1071692.  
<https://doi.org/10.3389/fbioe.2023.1071692>.
- [191] L.V. Maximiano, L.B. Correa, N.C. Gomes-da-Silva, L.S. da Costa, M.G.P. Da Silva, A.V. Chaves, M.L. Franco, P.B.A. Fechine, A.S. de Menezes, R. Santos-Oliveira, D.M. Andrade Neto, Magnesium whitlockite nanoparticles: Hydrothermal synthesis, anti-inflammatory and anti-cancer potential, *Colloids Surfaces B Biointerfaces* 239 (2024) 113931. <https://doi.org/10.1016/J.COLSURFB.2024.113931>.
- [192] F. Nigar, A.L. Johnston, J. Smith, W. Oakley, M.T. Islam, R. Felfel, D. Grant, E. Lester, I. Ahmed, Production of Nano Hydroxyapatite and Mg-Whitlockite from Biowaste-Derived products via Continuous Flow Hydrothermal Synthesis: A Step towards Circular Economy, *Materials (Basel)*. 16 (2023) 2138. <https://doi.org/10.3390/MA16062138/S1>.
- [193] A. Kizalaite, V. Klimavicius, J. Versockiene, E. Lastauskiene, T.

- Murauskas, R. Skaudzius, T. Yokoi, M. Kawashita, T. Goto, T. Sekino, A. Zarkov, Peculiarities of the formation, structural and morphological properties of zinc whitlockite ( $\text{Ca}_{18}\text{Zn}_2(\text{HPO}_4)_2(\text{PO}_4)_{12}$ ) synthesized via a phase transformation process under hydrothermal conditions, *CrystEngComm* 24 (2022) 5068–5079.  
<https://doi.org/10.1039/D2CE00497F>.
- [194] I. Grigoraviciute-Puroniene, Y. Tanaka, V. Vegelyte, Y. Nishimoto, K. Ishikawa, A. Kareiva, A novel synthetic approach to low-crystallinity calcium deficient hydroxyapatite, *Ceram. Int.* 45 (2019) 15620–15623. <https://doi.org/10.1016/J.CERAMINT.2019.05.072>.
- [195] J. Vecstaudza, M. Gasik, J. Locs, Amorphous calcium phosphate materials: Formation, structure and thermal behaviour, *J. Eur. Ceram. Soc.* 39 (2019) 1642–1649.  
<https://doi.org/10.1016/J.JEURCERAMSOC.2018.11.003>.
- [196] H. Nagai, M. Kobayashi-Fujioka, K. Fujisawa, G. Ohe, N. Takamaru, K. Hara, D. Uchida, T. Tamatani, K. Ishikawa, Y. Miyamoto, Effects of low crystalline carbonate apatite on proliferation and osteoblastic differentiation of human bone marrow cells, *J. Mater. Sci. Mater. Med.* 26 (2015) 1–8. <https://doi.org/10.1007/s10856-015-5431-5>.
- [197] V. Dhand, K.Y. Rhee, S.J. Park, The facile and low temperature synthesis of nanophase hydroxyapatite crystals using wet chemistry, *Mater. Sci. Eng. C* 36 (2014) 152–159.  
<https://doi.org/10.1016/J.MSEC.2013.11.049>.
- [198] Y. Sugiura, M.L. Munar, K. Ishikawa, Fabrication of octacalcium phosphate block through a dissolution-precipitation reaction using a calcium sulphate hemihydrate block as a precursor, *J. Mater. Sci. Mater. Med.* 29 (2018) 1–8. <https://doi.org/10.1007/s10856-018-6162-1>.
- [199] G. Tripathi, Y. Sugiura, A. Kareiva, E. Garskaite, K. Tsuru, K. Ishikawa, Feasibility evaluation of low-crystallinity  $\beta$ -tricalcium phosphate blocks as a bone substitute fabricated by a dissolution-precipitation reaction from  $\alpha$ -tricalcium phosphate blocks, *J. Biomater. Appl.* 33 (2018) 259–270.  
<https://doi.org/10.1177/0885328218788255>.
- [200] K. Tsuru, A. Yoshimoto, M. Kanazawa, Y. Sugiura, Y. Nakashima, K. Ishikawa, Fabrication of Carbonate Apatite Block through a Dissolution–Precipitation Reaction Using Calcium Hydrogen Phosphate Dihydrate Block as a Precursor, *Mater.* 10 (2017) 374. <https://doi.org/10.3390/MA10040374>.
- [201] R. Raiseliene, G. Linkaitė, A. Zarkov, A. Kareiva, I. Grigoraviciute, Large-Scale Green Synthesis of Magnesium Whitlockite from

- Environmentally Benign Precursor, Mater. 2024, 17 (2024) 788.  
<https://doi.org/10.3390/MA17040788>.
- [202] Y. Sugiura, M.L. Munar, K. Ishikawa, Fabrication of octacalcium phosphate foam through phase conversion and its histological evaluation, Mater. Lett. 212 (2018) 28–31.  
<https://doi.org/10.1016/J.MATLET.2017.10.051>.
- [203] Y. Sugiura, K. Ishikawa, Effect of Calcium and Phosphate on Compositional Conversion from Dicalcium Hydrogen Phosphate Dihydrate Blocks to Octacalcium Phosphate Blocks, Cryst. 8 (2018) 222. <https://doi.org/10.3390/CRYST8050222>.
- [204] K. Benataya, M. Lakrat, L.L. Elansari, E. Mejdoubi, Synthesis of B-type carbonated hydroxyapatite by a new dissolution-precipitation method, Mater. Today Proc. 31 (2020) S83–S88.  
<https://doi.org/10.1016/J.MATPR.2020.06.100>.
- [205] M. Shimabukuro, K. Hayashi, R. Kishida, A. Tsuchiya, K. Ishikawa, Effects of carbonate ions in phosphate solution on the fabrication of carbonate apatite through a dissolution–precipitation reaction, Ceram. Int. 48 (2022) 1032–1037.  
<https://doi.org/10.1016/J.CERAMINT.2021.09.188>.
- [206] A. Afonina, A. Kizalaite, A. Zarkov, A. Drabavicius, T. Goto, T. Sekino, A. Kareiva, I. Grigoraviciute-Puroniene, Synthesis of whitlockite nanopowders with different magnesium content, Ceram. Int. 48 (2022) 32125–32130.  
<https://doi.org/10.1016/J.CERAMINT.2022.07.152>.
- [207] D. Alves Cardoso, J.A. Jansen, S.C. Leeuwenburgh, Synthesis and application of nanostructured calcium phosphate ceramics for bone regeneration, J. Biomed. Mater. Res. Part B Appl. Biomater. 100B (2012) 2316–2326. <https://doi.org/10.1002/JBM.B.32794>.
- [208] N.S. Muthiah Pillai, K. Eswar, S. Amirthalingam, U. Mony, P. Kerala Varma, R. Jayakumar, Injectable Nano Whitlockite Incorporated Chitosan Hydrogel for Effective Hemostasis, ACS Appl. Bio Mater. 2 (2019) 865–873. <https://doi.org/10.1021/acsabm.8b00710>.
- [209] M. Wang, J. Yao, S. Shen, C. Heng, Y. Zhang, T. Yang, X. Zheng, A scaffold with zinc-whitlockite nanoparticles accelerates bone reconstruction by promoting bone differentiation and angiogenesis, Nano Res. 16 (2023) 757–770. <https://doi.org/10.1007/s12274-022-4644-4>.
- [210] D. Griesiute, A. Kizalaite, A. Dubnika, V. Klimavicius, V. Kalendra, V. Tyrpekl, S.H. Cho, T. Goto, T. Sekino, A. Zarkov, Cite this: Dalton Trans, 53 (2024) 1722. <https://doi.org/10.1039/d3dt03756h>.

- [211] A. V. Teterskii, S.Y. Stefanovich, B.I. Lazoryak, D.A. Rusakov, Whitlockite solid solutions  $\text{Ca}_{9-x}\text{M}_x\text{R}(\text{PO}_4)_7$  ( $x = 1, 1.5$ ; M = Mg, Zn, Cd; R = Ln, Y) with antiferroelectric properties, Russ. J. Inorg. Chem. 52 (2007) 308–314. <https://doi.org/10.1134/S0036023607030023>.
- [212] S. Amirthalingam, S.S. Lee, M. Pandian, J. Ramu, S. Iyer, N.S. Hwang, R. Jayakumar, Combinatorial effect of nano whitlockite/nano bioglass with FGF-18 in an injectable hydrogel for craniofacial bone regeneration, Biomater. Sci. 9 (2021) 2439–2453. <https://doi.org/10.1039/D0BM01496F>.
- [213] J. Du, Y. Zhang, J. Wang, M. Xu, M. Qin, X. Zhang, D. Huang, Highly resilient porous polyurethane composite scaffolds filled with whitlockite for bone tissue engineering, J. Biomater. Sci. Polym. Ed. 34 (2023) 845–859. <https://doi.org/10.1080/09205063.2022.2145871>.
- [214] N. Rochdi, brahim Majidi, N. Habti, Y. Naimi, A new percentage of biphasic calcium phosphate (BCP) of nanoparticles synthesized directly by hydrothermal process, Mediterr. J. Chem. 10 (2020) 355–362. <https://doi.org/10.13171/mjc10402004221251nr>.
- [215] A.C. Tas, Transformation of Brushite ( $\text{CaHPO}_4 \cdot 2\text{H}_2\text{O}$ ) to Whitlockite ( $\text{Ca}_9\text{Mg}(\text{HPO}_4)(\text{PO}_4)_6$ ) or Other CaPs in Physiologically Relevant Solutions, J. Am. Ceram. Soc. 99 (2016) 1200–1206. <https://doi.org/10.1111/JACE.14069>.
- [216] S.Y. Stefanovich, B.I. Lazoryak, A.M. Antipin, A.S. Volkov, A.I. Evdokimov, O.A. Gurbanova, O. V. Dimitrova, D. V. Deyneko, Crystal structures of biocompatible Mg-, Zn-, and Co-whitlockites synthesized via one-step hydrothermal reaction, Zeitschrift Fur Krist. - Cryst. Mater. 238 (2023) 301–309. <https://doi.org/10.1515/zkri-2023-0016>
- [217] M.N. Hassan, M.M. Mahmoud, A.A. El-Fattah, S. Kandil, Microwave-assisted preparation of Nano-hydroxyapatite for bone substitutes, Ceram. Int. 42 (2016) 3725–3744. <https://doi.org/10.1016/J.CERAMINT.2015.11.044>.
- [218] C. Qi, Y.J. Zhu, X.Y. Zhao, B.Q. Lu, Q.L. Tang, J. Zhao, F. Chen, Highly Stable Amorphous Calcium Phosphate Porous Nanospheres: Microwave-Assisted Rapid Synthesis Using ATP as Phosphorus Source and Stabilizer, and Their Application in Anticancer Drug Delivery, Chem. – A Eur. J. 19 (2013) 981–987. <https://doi.org/10.1002/CHEM.201202829>.
- [219] C. Qi, Y.-J. Zhu, F. Chen, J. Wu, Porous microspheres of magnesium whitlockite and amorphous calcium magnesium phosphate: microwave-assisted rapid synthesis using creatine phosphate, and

- application in drug delivery †, *J. Mater. Chem. B* 3 (2015) 7775. <https://doi.org/10.1039/c5tb01106j>.
- [220] Z.Y. Cai, F. Peng, Y.P. Zi, F. Chen, Q.R. Qian, Microwave-Assisted Hydrothermal Rapid Synthesis of Calcium Phosphates: Structural Control and Application in Protein Adsorption, *Nanomater.* 5 (2015) 1284–1296. <https://doi.org/10.3390/NANO5031284>.
- [221] C. Qi, F. Chen, J. Wu, Y.J. Zhu, C.N. Hao, J.L. Duan, Magnesium whitlockite hollow microspheres: a comparison of microwave-hydrothermal and conventional hydrothermal syntheses using fructose 1,6-bisphosphate, and application in protein adsorption, *RSC Adv.* 6 (2016) 33393–33402. <https://doi.org/10.1039/C6RA00775A>.
- [222] C. Lin, Y. Wang, Y. Zhou, Y. Zeng, C.C. Lin, A rapid way to synthesize magnesium whitlockite microspheres for high efficiency removing heavy metals, *Desalination and water treatment* 162 (2019) 220-227. <https://doi.org/10.5004/dwt.2019.24290>.
- [223] M. Lakrat, H. Jodati, E.M. Mejdoubi, Z. Evis, Synthesis and characterization of pure and Mg, Cu, Ag, and Sr doped calcium-deficient hydroxyapatite from brushite as precursor using the dissolution-precipitation method, *Powder Technol.* 413 (2023) 118026. <https://doi.org/10.1016/J.POWTEC.2022.118026>.
- [224] J. Rodríguez-Carvajal, T. Roisnel, Line Broadening Analysis Using FullProf\*: Determination of Microstructural Properties, *Mater. Sci. Forum* 443–444 (2004) 123–126. <https://doi.org/10.4028/WWW.SCIENTIFIC.NET/MSF.443-444.123>.
- [225] S. Brunauer, P.H. Emmett, E. Teller, Adsorption of Gases in Multimolecular Layers, *J. Am. Chem. Soc.* 60 (1938) 309–319. <https://doi.org/10.1021/ja01269a023>.
- [226] E.P. Barrett, L.G. Joyner, P.P. Halenda, The Determination of Pore Volume and Area Distributions in Porous Substances. I. Computations from Nitrogen Isotherms, *J. Am. Chem. Soc.* 73 (1951) 373–380. <https://doi.org/10.1021/ja01145a126>.
- [227] U. Kuila, M. Prasad, Specific surface area and pore-size distribution in clays and shales, *Geophys. Prospect.* 61 (2013) 341–362. <https://doi.org/10.1111/1365-2478.12028>.
- [228] S. Suppi, K. Kasemets, A. Ivask, K. Künnis-Beres, M. Sihtmäe, I. Kurvet, V. Aruoja, A. Kahru, A novel method for comparison of biocidal properties of nanomaterials to bacteria, yeasts and algae, *J. Hazard. Mater.* 286 (2015) 75–84. <https://doi.org/10.1016/J.JHAZMAT.2014.12.027>.
- [229] H.C. Hsu, W.H. Tuan, H.Y. Lee, In-situ observation on the

- transformation of calcium phosphate cement into hydroxyapatite, *Mater. Sci. Eng. C* 29 (2009) 950–954.  
<https://doi.org/10.1016/J.MSEC.2008.08.014>.
- [230] M. El Hazzat, A. El Hamidi, M. Halim, S. Arsalane, Complex evolution of phase during the thermal investigation of Brushite-type calcium phosphate  $\text{CaHPO}_4 \cdot 2\text{H}_2\text{O}$ , *Materialia* 16 (2021) 101055.  
<https://doi.org/10.1016/J.MTLA.2021.101055>.
- [231] E. Mhla, P.G. Koutsoukos, Heterogeneous crystallization of calcium hydrogen phosphate anhydrous (monetite), *Colloids Surfaces A Physicochem. Eng. Asp.* 513 (2017) 125–135.  
<https://doi.org/10.1016/J.COLSURFA.2016.11.041>.
- [232] F. Capitelli, F. Bosi, S.C. Capelli, F. Radica, G. Della Ventura, Neutron and XRD Single-Crystal Diffraction Study and Vibrational Properties of Whitlockite, the Natural Counterpart of Synthetic Tricalcium Phosphate, *Cryst.* 11 (2021) 225.  
<https://doi.org/10.3390/CRYST11030225>.
- [233] F. Baino, S. Caddeo, C. Vitale-Brovarone, Sintering effects of bioactive glass incorporation in tricalcium phosphate scaffolds, *Mater. Lett.* 274 (2020) 128010. <https://doi.org/10.1016/J.MATLET.2020.128010>.
- [234] M.T. Fulmer, I.C. Ison, C.R. Hankermayer, B.R. Constantz, J. Ross, Measurements of the solubilities and dissolution rates of several hydroxyapatites, *Biomaterials* 23 (2002) 751–755.  
[https://doi.org/10.1016/S0142-9612\(01\)00180-6](https://doi.org/10.1016/S0142-9612(01)00180-6).
- [235] C. Stähli, J. Thüring, L. Galea, S. Ne Tadier, M. Bohner, N. Döbelin, Hydrogen-substituted b-tricalcium phosphate synthesized in organic media, *Res. Pap. Acta Cryst* 72 (2016) 875–884.  
<https://doi.org/10.1107/S2052520616015675>.
- [236] R.G. Carrodeguas, S. De Aza,  $\alpha$ -Tricalcium phosphate: Synthesis, properties and biomedical applications, *Acta Biomater.* 7 (2011) 3536–3546. <https://doi.org/10.1016/J.ACTBIO.2011.06.019>.
- [237] B. Myszka, M. Schüßler, K. Hurle, B. Demmert, R. Detsch, A.R. Boccaccini, S.E. Wolf, Phase-specific bioactivity and altered Ostwald ripening pathways of calcium carbonate polymorphs in simulated body fluid, *RSC Adv.* 9 (2019) 18232–18244.  
<https://doi.org/10.1039/C9RA01473J>.
- [238] K. Ishikawa, E. Garskaite, A. Kareiva, Sol–gel synthesis of calcium phosphate-based biomaterials—A review of environmentally benign, simple, and effective synthesis routes, *J. Sol-Gel Sci. Technol.* 2020 943 94 (2020) 551–572. <https://doi.org/10.1007/S10971-020-05245-8>.
- [239] M. Thommes, K. Kaneko, A. V. Neimark, J.P. Olivier, F. Rodriguez-

- Reinoso, J. Rouquerol, K.S.W. Sing, Physisorption of gases, with special reference to the evaluation of surface area and pore size distribution (IUPAC Technical Report), *Pure Appl. Chem.* 87 (2015) 1051–1069. <https://doi.org/10.1515/pac-2014-1117>.
- [240] M. Retajczyk, A. Wróblewska, A. Szymańska, B. Michalkiewicz, Isomerization of limonene over natural zeolite-clinoptilolite, *Clay Miner.* 54 (2019) 121–129. <https://doi.org/10.1180/CLM.2019.18>.
- [241] D. Lee, P.N. Kumta, Chemical synthesis and stabilization of magnesium substituted brushite, *Mater. Sci. Eng. C* 30 (2010) 934–943. <https://doi.org/10.1016/J.MSEC.2010.04.007>.
- [242] T. Konishi, S. Watanabe, Hydrothermal transformation of calcium hydrogen phosphate dihydrate into magnesium whitlockite, 37 (2021) 21–025. <https://doi.org/10.3363/prb.37.21>.
- [243] L. Obadia, T. Rouillon, B. Bujoli, G. Daculsi, J.M. Bouler, Calcium-deficient apatite synthesized by ammonia hydrolysis of dicalcium phosphate dihydrate: Influence of temperature, time, and pressure, *J. Biomed. Mater. Res. Part B Appl. Biomater.* 80B (2007) 32–42. <https://doi.org/10.1002/JBM.B.30565>.
- [244] C. Stähli, J. Thüring, L. Galea, S. Tadier, M. Bohner, N. Döbelin, Hydrogen-substituted  $\beta$ -tricalcium phosphate synthesized in organic media, *Acta Crystallogr. Sect. B Struct. Sci. Cryst. Eng. Mater.* 72 (2016) 875–884. <https://doi.org/10.1107/S2052520616015675>.
- [245] J. Xu, I.S. Butler, D.F.R. Gilson, FT-Raman and high-pressure infrared spectroscopic studies of dicalcium phosphate dihydrate ( $\text{CaHPO}_4 \cdot 2\text{H}_2\text{O}$ ) and anhydrous dicalcium phosphate ( $\text{CaHPO}_4$ ), *Spectrochim. Acta Part A Mol. Biomol. Spectrosc.* 55 (1999) 2801–2809. [https://doi.org/10.1016/S1386-1425\(99\)00090-6](https://doi.org/10.1016/S1386-1425(99)00090-6).
- [246] A. Tsuchiya, M. Sato, I. Takahashi, K. Ishikawa, Fabrication of apatite-coated gypsum granules and histological evaluation using rabbits, *Ceram. Int.* 44 (2018) 20330–20336. <https://doi.org/10.1016/J.CERAMINT.2018.08.021>.
- [247] T. Sugimoto, Preparation of monodispersed colloidal particles, *Adv. Colloid Interface Sci.* 28 (1987) 65–108. [https://doi.org/10.1016/0001-8686\(87\)80009-X](https://doi.org/10.1016/0001-8686(87)80009-X).
- [248] V.G. Baldovino-Medrano, V. Niño-Celis, R. Isaacs Giraldo, Systematic Analysis of the Nitrogen Adsorption-Desorption Isotherms Recorded for a Series of Materials Based on Microporous-Mesoporous Amorphous Aluminosilicates Using Classical Methods, *J. Chem. Eng. Data* 68 (2023) 2512–2528. <https://doi.org/10.1021/acs.jced.3c00257>.
- [249] G. Tozzi, A. De Mori, A. Oliveira, M. Roldo, Composite Hydrogels

- for Bone Regeneration, Mater. 9 (2016) 267.  
<https://doi.org/10.3390/MA9040267>.
- [250] S. Nomura, K. Tsuru, S. Matsuya, I. Takahashi, K. Ishikawa, Fabrication of Spherical Carbonate Apatite Using Calcium Sulfate as a Precursor by W/O Emulsion Method, Key Eng. Mater. 529–530 (2013) 78–81.  
<https://doi.org/10.4028/www.scientific.net/KEM.529-530.78>.
- [251] N. Angelova, S. Koleva, M. Kostadinov, G. Yordanov, Preparation, characterization and protein adsorption properties of nanostructured magnesium whitlockite, J. Mater. Sci. 57 (2022) 21571–21582.  
<https://doi.org/10.1007/s10853-022-08011-z>.
- [252] C.F. Holder, R.E. Schaak, Tutorial on Powder X-ray Diffraction for Characterizing Nanoscale Materials, ACS Nano 13 (2019) 7359–7365.  
<https://doi.org/10.1021/acsnano.9b05157>.
- [253] W. Xiang-qin, S. Fei, Y. Wei, C. Lei, W. Shu-mei, Fingerprinting of Mineral Medicine Natrii Sulfas by Fourier Transform Infrared Spectroscopy, 36 (2021) 38–43.  
<https://www.spectroscopyonline.com/view/fingerprinting-of-mineral-medicine-natrii-sulfas-by-fourier-transform-infrared-spectroscopy>.
- [254] R. Karalkeviciene, E. Raudonyte-Svirbutaviciene, A. Zarkov, J.C. Yang, A.I. Popov, A. Kareiva, Solvothermal Synthesis of Calcium Hydroxyapatite via Hydrolysis of Alpha-Tricalcium Phosphate in the Presence of Different Organic Additives, Crystals 13 (2023) 265.  
<https://doi.org/10.3390/CRYST13020265/S1>.
- [255] M.S. Djošić, V.B. Mišković-Stanković, Z.M. Kačarević-Popović, B.M. Jokić, N. Bibić, M. Mitić, S.K. Milonjić, R. Jančić-Heinemann, J. Stojanović, Electrochemical synthesis of nanosized monetite powder and its electrophoretic deposition on titanium, Colloids Surfaces A Physicochem. Eng. Asp. 341 (2009) 110–117.  
<https://doi.org/10.1016/J.COLSURFA.2009.03.046>.

## ACKNOWLEDGMENTS

I want to express my sincere gratitude to all those who supported and guided me throughout this endeavor. I am deeply thankful to Prof. Habil. Dr. A. Kareiva for welcoming me into the Department of Inorganic Chemistry and offering me the chance to pursue my studies. I am especially grateful to my supervisor, Assoc. Prof. dr. Inga Grigoravičiūtė, for her exceptional guidance, encouragement, and support. She provided strength, reassurance, and friendship whenever I needed it most. It is because of her steadfast help that I was able to complete this work successfully. I also sincerely thank Assoc. Prof. Dr. Justina Gaidukevič, Dr. Andrius Pakalniškis, and Prof. Dr. Ramūnas Skaudžius for their significant assistance and training in performing specific measurements. I am also grateful to Dr. Monika Mortimer for antibacterial studies.

I am profoundly grateful to my husband, Audrius, for his patience, faith, encouragement, and care for our children when I needed support the most. I also extend my heartfelt appreciation to both my parents and my husband's parents for their generous willingness to take care of our children, allowing me the time to focus on this work.

## LIST OF PUBLICATIONS AND ATTENDING CONFERENCES

### Publications in Journal

1. **R. Raiseliene**, G. Linkaite, A. Zarkov, A. Kareiva, I. Grigoraviciute. *Large-Scale Green Synthesis of Magnesium Whitlockite from Environmentally Benign Precursor*. Materials, 17(4) (2024) 788. <https://doi.org/10.3390/ma17040788>.
2. **R. Raiseliene**, G. Linkaite, A. Zarkov, M. Mortimer, A. Kareiva, I. Grigoraviciute. *Synthesis of Magnesium Whitlockite Granules via a Dissolution-Precipitation Reaction*. Ceramics International, available online 26 April 2025. <https://doi.org/10.1016/j.ceramint.2025.04.373>.
3. **R. Raiseliene**, G. Linkaite, A. Ezerskyte, I. Grigoraviciute. *Tailored Morphology and Phase Evolution of Magnesium Whitlockite Granules via a Dissolution–Precipitation Approach*. Applied Sciences, 15(13) (2025) 7221. <https://doi.org/10.3390/app15137221>.

### Attended Conferences

1. **R. Raiseliene**, G. Linkaite, I. Grigoraviciute, A. Kareiva. *Synthesis and Investigation of Magnesium Whitlockite Granules*. Functional Inorganic Materials (FIM 2022), Vilnius, Lithuania, 6-8 October 2022.
2. **R. Raiseliene**, G. Linkaite, I. Grigoraviciute-Puroniene, A. Kareiva. *Phase transformations in the synthesis of magnesium whitlockite granules*. Ignacy Domeyko and the intellectual environment of Vilnius at the beginning of the 19th century, Vilnius, Lithuania, 20 October 2022.
3. **R. Raiseliene**, G. Linkaite, I. Grigoraviciute-Puroniene, A. Kareiva. *Synthesis of magnesium whitlockite granules*. Chemistry and Chemical Technology 2022 (CCT2022), Kaunas, Lithuania, 14 October 2022.
4. **R. Raiseliene**, G. Linkaite, A. Kareiva, I. Grigoraviciute. *Synthesis and Investigation of Biphasic Calcium Phosphate Granules*. Chemistry and Chemical Technology 2023 (CCT-2023), Vilnius, Lithuania, 10 March 2023.
5. G. Linkaitė, S. Bendžiūtė, **R. Raišelienė**, A. Kareiva, I. Grigoravičiūtė. *Synthesis of biphasic magnesium whitlockite and carbonated hydroxyapatite granules*. Chemija ir cheminė technologija 2023: studentų mokslinės konferencijos pranešimų medžiaga, Klaipėda, Lietuva, 2023 m. gegužės 12 d.

6. **R. Raišlienė**, G. Linkaitė, A. Žarkov, M. Mortimer, A. Kareiva, I. Grigoravičiūtė. *Synthesis of magnesium whitlockite granules via a continuous dissolution-precipitation reaction*. The 2<sup>nd</sup> Central and Eastern European Conference on Physical Chemistry & Materials Science (CEEC-PCMS2), Kaunas, Lithuania, 16-19 September 2024.
7. **R. Raišlienė**, G. Linkaitė, A. Žarkov, A. Kareiva, I. Grigoravičiūtė. *Aplinkai draugiška didelio kieko magnio vitlokito miltelių sintezė*. Chemija ir geomokslai 2024, Vilnius, Lietuva, 2024 m. kovo 22 d.
8. G. E. Budžytė, **R. Raišlienė**, I. Grigoravičiūtė, A. Kareiva, A. Žarkov. *Magnio vitlokito sintezės iš amorfino kalcio fosfato parametru optimizavimas*. Chemija ir geomokslai 2024, Vilnius, Lietuva, 2024 m. kovo 22 d.
9. **R. Raišlienė**, G. Linkaitė, A. Žarkov, A. Kareiva, M. Skruodienė, I. Grigoravičiūtė. *Large amount synthesis of magnesium whitlockite nanopowders from an environmentally friendly initial reactant*. Open readings 2024, Vilnius, Lithuania, 23-26 April 2024.
10. G. Linkaitė, **R. Raišlienė**, A. Kareiva, M. Skruodienė, I. Grigoravičiūtė. *Synthesis of biphasic calcium phosphate granules under static and rotating conditions from environmentally benign precursor – gypsum*. Open readings 2024, Vilnius, Lithuania, 23-26 April 2024.
11. G. E. Budžytė, **R. Raišlienė**, I. Grigoravičiūtė, A. Kareiva, A. Žarkov. *Dissolution-precipitation synthesis of magnesium whitlockite from amorphous calcium phosphate*. Open readings 2024, Vilnius, Lithuania, 23-26 April 2024.
12. G. Linkaitė, **R. Raišlienė**, A. Kareiva, I. Grigoravičiūtė. *Synthesis of biphasic calcium phosphate granules from gypsum under static and rotating conditions*. 6th international conference: Rare earth materials: advances in synthesis, studies and applications, Vilnius, Lithuania, 20–23 October 2024.
13. **R. Raišlienė**, G. Linkaitė, S. Astramskas, A. Kareiva, I. Grigoravičiūtė. *Skirtingos morfologinės sudėties magnio vitlokito granulių sintezė, ištyrimas bei tarpinių fazinių identifikavimas*. Chemija ir geomokslai 2025, Vilnius, Lietuva, 2025 kovo 14 d.
14. G. Linkaitė, **R. Raišlienė**, I. Grigoravičiūtė, A. Kareiva. *Environmentally friendly synthesis of biphasic calcium phosphates: transformation of gypsum under different synthesis profiles*. Chemija ir geomokslai 2025, Vilnius, Lietuva, 2025 kovo 14 d.

## CURRICULUM VITAE

<b>Vardas Pavardė</b>	Rūta Raišelienė
<b>Darbo patirtis</b>	
Laikotarpis	Nuo 2013 m. 06 mén. iki 2022 m. 10 mén.
Pareigos	Vyresnioji inžinierė
Pagrindinės veiklos ir atsakomybės	Cheminės kontrolės duomenų analizė bei ataskaitų ruošimas, legioneliozės prevencija, naftos produktų chromatografinė analizė, chemiškai valyto vandens ruošimo instrukcijų rengimas, peržiūra, pavaldaus personalo darbo kontrolė, mokymas, jų darbo laiko apskaitos žiniaraščio tvarkymas.
Darbovietės pavadinimas ir adresas	AB Vilniaus šilumos tinklai (buvusi UAB “Vilniaus energija”), Spaudos g. 6-1, Vilnius
Laikotarpis	Nuo 2011 m. 12 mén. iki 2013 m. 06 mén.
Pareigos	Inžinierė
Pagrindinės veiklos ir atsakomybės	Atsakinga už laboratorijoje atliekamų cheminių analizių vidinę kontrolę, aplinkos monitoringo bei technologinių vandenų kontrolę, vandeninių tirpalų jonų chromatografijos analizę.
Darbovietės pavadinimas ir adresas	UAB “Vilniaus energija”, Jočionių g. 13 , Vilnius
Laikotarpis	Nuo 2008 m. 06 mén. iki 2011 m. 12 mén.
Pareigos	Laborantė
Pagrindinės veiklos ir atsakomybės	Termofikacinio, technologinio vandens cheminė analizė, rezultatų įvertinimas bei sisteminimas.
Darbovietės pavadinimas ir adresas	UAB “Vilniaus energija”, Jočionių g.13 , Vilnius
Darbovietės veiklos sritis arba ūkio šaka	Bendrovė centralizuotai aprūpina šiluma daugiau nei 195 tūkstančius butų Vilniaus mieste, taip pat Grigiškėse, Salininkuose ir Trakų Vokėje.
Laikotarpis	Nuo 2007 m. 08 mén. iki 2007 m. 10 mén.

	Statusas	Praktikantė
Pagrindinės veiklos ir atsakomybės		Augalinių eterinių aliejų cheminė analizė. Dirbau su dujų chromatografu, spec. distiliavimo įranga.
Darbovietaės pavadinimas ir adresas		Chemijos Institutas, A. Goštauto g. 9, Vilnius
Darbovietaės veiklos sritis arba ūkio šaka		Chemijos mokslo ir technologijų plėtra, siekiant padidinti chemijos bei jai gimininguų sričių žinių fondą ir taikyti jį visuomenės gyvenimo kokybei gerinti.
<b>Išsilavinimas</b>		
Laikotarpis		Nuo 2019 m. iki dabar
Kvalifikacija		Chemijos doktorantė
Įstaigos, kurioje įgytas išsilavinimas, pavadinimas		Vilniaus universitetas, Chemijos ir geomokslų fakultetas, Naugarduko g. 24, LT – 03225, Vilnius
Laikotarpis		2007 – 2009 m.
Kvalifikacija		Chemijos magistro laipsnis
Įstaigos, kurioje įgytas išsilavinimas, pavadinimas		Vilniaus universitetas, Chemijos fakultetas, Naugarduko g. 24, LT – 03225, Vilnius
Laikotarpis		2003 – 2007 m.
Kvalifikacija		Chemijos bakalauro laipsnis
Įstaigos, kurioje įgytas šsilavinimas, pavadinimas		Vilniaus universitetas, Chemijos fakultetas, Naugarduko g. 24, LT – 03225, Vilnius
<b>Kalbiniai įgūdžiai</b>		
Gimtoji kalba		Lietuvių
Kitos kalbos		Anglų: B1 lygis Rusų: A2 lygis

Vilniaus universiteto leidykla  
Saulėtekio al. 9, III rūmai, LT-10222 Vilnius  
El. p. [info@leidykla.vu.lt](mailto:info@leidykla.vu.lt), [www.leidykla.vu.lt](http://www.leidykla.vu.lt)  
[bookshop.vu.lt](http://bookshop.vu.lt), [journals.vu.lt](http://journals.vu.lt)  
Tiražas 20 egz.